Nouvelles technologies de réception cohérente pour la mesure et le contrôle des paramètres physiques de transmission sur fibres optiques

Alix May

To cite this version:

Alix May. Nouvelles technologies de réception cohérente pour la mesure et le contrôle des paramètres physiques de transmission sur fibres optiques. Optique / photonique. Institut Polytechnique de Paris, 2023. Français. NNT : 2023IPPAT013 . tel-04188312

HAL Id: tel-04188312
https://theses.hal.science/tel-04188312v1

INSTITUT
POLYTECHNIQUE
DE PARIS

NNT : 2023IPPAT013

Thèse de doctorat

TELECOM
Paris

IP PARIS

Novel receiver-based techniques for the monitoring of physical parameters in optical fiber networks

Thèse de doctorat de l'Institut Polytechnique de Paris
préparée à Télécom Paris

École doctorale n° 626 - Ecole Doctorale de l'Institut Polytechnique de Paris (ED IP Paris)
Spécialité de doctorat : Réseaux, informations et communications

Thèse présentée et soutenue à Palaiseau, le 7 Avril 2023, par

ALIX MAY

Composition du Jury :

Christophe Peucheret Professeur, ENSSAT Lannion	Président/Examinateur
Christelle Aupetit-Berthelemot Professeure, Université de Limoges	Rapportrice
Gabriella Bosco Professeure, Politecnico di Torino	Rapportrice
Chigo Okonkwo Professeur associé, Eindhoven University of Technology	Examinateur
Nicolas Dubreuil Professeur, Institut d'Optique Graduate School	Examinateur
Philippe Ciblat Professeur, Télécom Paris	Directeur de thèse
Elie Awwad Maitre de conférences, Télécom Paris	Co-directeur de thèse
Fabien Boitier Ingénieur de recherche, Nokia Networks France	Invité

Acknowledgements

I would like to express my deepest gratitude to all of the people who have supported me during this exciting and challenging process. Having carried out my PhD in collaboration between Nokia Bell Labs and Télécom Paris, I had the wonderful opportunity to interact and work with a wide variety of people and characters from whom I learned a lot.

First of all, I would like to thank Nicolas Dubreuil and Philippe Jennevé who introduced me to the telecom world through the Supoptique team project “PIMS”. I particularly appreciated Nicolas’ ongoing and contagious enthusiasm and Philippe’s kindness and pedagogy. My willingness to pursue a PhD degree at Nokia was all the more confirmed after a 3-month internship with Philippe as my supervisor.

Then, I want to thank Philippe Ciblat and Elie Awwad from Télécom Paris who agreed to be my PhD supervisors. I appreciated that Philippe was coming from another field from optics and was able to bring his outside view on my work. I also appreciated his availability and careness as well as our interesting discussions and debates about work or life. Regarding Elie, I greatly appreciated his impressive pedagogic skills and his optimism which makes learning and going forward easy. Also, his unparalleled kindness makes it very agreeable to work and to interact with him.

I now want to thank the people which supervised me at Nokia. A big warm thank you to Fabien who introduced me to this wonderful topic, who followed me and worked with me during these 3 years with a lot of dedication, pedagogy, patience and a bit of humour. A thank you to Petros for fruitful conversations about research where he always shows his famous touch of madness. Thanks to him, I am also a happy client of Quitoque which provides me food every once in a while. I want to thank also Matteo for his infectious passion for research and his help during my learning of Optilux. Matteo, who has been also a dear friend to me for a very long time now. Finally, I would like to thank Patricia Layec for giving me the opportunity to pursue a PhD in her team and more recently to join her team as a permanent

researcher.

Thanks to Nokia, I was able to meet a great deal of interesting and wonderful people, with whom I shared many great moments, whether it be in the “Columbus” at Nozay, in the lab for coffee time, in “Le Bureau” at Courtaboeuf and more recently at Massy. We managed to keep a team spirit despite a few disturbances along the way, the covid, the air conditioning issues and the move to Massy. To name a few, Mijail, Nihel, Arnaud, Emmanuel, Rajiv, Eric, Haïk, Sébastien, Joana, Samar, Sterenn, Xiaoyan, Isaia or my neighbour Jelena.

A special thank you to Guillaume and Aymeric for being there with me daily during and after office hours. Thank you for the nice, funny (Aymeric!) and interesting conversations as well as our many sport sessions: aqua cycling, squash, hiking and of course climbing. We have - almost...- tried them all! Guillaume, thank you for the talks, the Chaï Latte, origami roses, and the games (wordle, worldle, quordle and many more).

I would like to thank my old(er) friends for their support, kindness and patience: Alice, Faustine, Elise, Jeremie, Laurie, Fanny, Flora, Manon. A special thanks to my dearest Axelle, for your kindness, presence and insatiable thirst for knowledge, in every domains.

My penultimate thanks go to my family, my parents and my dear brother who always supported me and challenged me with their questions about my work. My last thanks go to my dear Sylvain whom I was lucky to meet at the beginning of this Bell Labs adventure and who supported me the whole time.

Résumé en français

Les systèmes de transmission par fibre optique transportent plus de 99 % du trafic des données dans le monde. Ce succès presque inégalé est lié premièrement aux propriétés physique de la silice. L'atténuation du champ électromagnétique qui se propage dans une fibre optique est relativement faible, de l'ordre de 2 dB/km, particulièrement dans la région infrarouge (1.5 μm-1.6 μm). Cela correspond à une division par 2 de la puissance du power chaque 15 kilomètre. Par comparison, pour les cables de cuivre, à une fréquence de 60 MHz, l'atténuation est de 18 dB/km (G-623, ITU-T). Deuxièmement, l'amplification large bande, sur des dizaines de nanomètres dans la région infrarouge, a permis à ces liens optiques de transmettre des données sur des distances transocéaniques en concaténant des tronçons de fibre et des amplificateurs optiques. Enfin, l'avènement de la technologie cohérente, le développement de techniques puissantes de traitement du signal ainsi que le développement d'algorithmes de correction d'erreur directe (FEC) ont permis de s'approcher très proche de la capacité permise par la capacité limite de Shannon.

Ces 30 dernières années, le développement des systèmes de transmission par fibre optique a permis de répondre aux besoins croissants en utilisation d'Internet, qui ne devraient pas diminuer de si tôt. Tandis que le pourcentage d'utilisateurs mondiaux d'Internet était de 50 % en 2018, on s'attendait à ce qu'il monte à 66 % de la population mondiale d'ici 2023, ce qui correspondrait à 5.3 milliards d'utilisateurs au total. Notons qu'en 2022, le nombre d'utilisateurs mondiaux d'Internet a atteint 5.03 milliard, ce qui confirme la tendance attendue. Tandis que de plus en plus de personnes utilisent Internet, chaque utilisateur a besoin d'un nombre grandissant d'appareils, surtout des appareils de type Internet des Objects (IOT). Tandis que le nombre d'utilisateurs d'Internet devrait passer de 4.7 en 2020 à 5.5 milliards en 2025, le nombre d'objets connectés ou d'objects IOT devrait passer de 20 en 2020 à 48 milliards en 2025.

Pour répondre à la croissance du trafic tout en réduisant le coût par bit transmis, l'optimisation des réseaux optiques est nécessaire. A cette fin, une première solution est de permettre la flexibility et la dynamicité de ces derniers. C'est ce qui est permis par les réseaux élastiques, où les grilles de fréquence deviennent flexibles et les débits sont variés pour s'adapter aux besoins du réseau.

Pour permettre une plus grande optimisation, l'opérateur a besoin d'une connaissance du réseau de manière constante. Par exemple, si les opérateurs connaissent avec plus de précision l'état des paramètres de leur système, ils peuvent ajouter ou retirer des liaisons optiques avec des marges précises, dépanner, effectuer de la maintenance proactive de composants défectueux and enfin aussi adapter les paramètres de transmission aussi rapidement que possible.

Les premières techniques de monitoring (ou surveillance en français) ont été developpées avant les réseaux élastiques et dynamiques. Cependant, ces techniques requièrent généralement l'utilisation de composants externes ou de canaux dédiés. Pour une optimisation totale, utiliser des émetteurs-récepteurs déjà déployés pour du monitoring est particulièrement souhaitable pour baisser les coûts. Dans ce contexte, l'avènement de la technologie cohérente a offert nombreuses opportunités pour le monitoring. En effet, les récepteurs cohérents effectuent de l'estimation aveugle ou assistée par des données ainsi que de la compensation de plusieurs effets physiques. Le monitoring de paramètres aggregés comme la dispersion chromatique résiduelle accumulée, la dispersion modale de polarisation (PMD) accumulée ou la perte dépendante de la polarisation (PDL) accumulée sont proposés, par exemple les travaux de Hauske en 2009.

Comme l'évolution de la puissance longitudinale le long de la fibre a un impact significatif sur la performance totale, il est important de la mesurer. Le reflectomètre optique (en anglais OTDR for optical time-domain reflectometer) est un appareil qui permet la caractérisation des pertes de propagation le long de la fibre en analysant la lumière retro-réfléchie. Bien qu'étant plutôt précis and pertinent pour la caractérisation des anomalies de puissance, il y a plusieurs limitations à son utilisation pour un monitoring massif. Son prix est susceptible de limiter l'ampleur de son implémentation dans un réseau ainsi que la nécessité d'utiliser des signaux hors bande. Estimer la puissance longitudinale en utilisant des données de télémétrie déjà disponibles au niveau du récepteur serait d'autant plus pertinent pour un monitoring à bas coût et efficace.

Dans ce contexte, deux techniques pionnières ont été proposées pour estimer le profil longitudinal de puissance, c'est-à-dire la puissance en chacun des points de la ligne, seulement en effectuant un traitement du signal particulier sur les données récupérées au récepteur cohérent. Les deux travaux exploitent l'apparition d'effets non-linéaires distribués pendant la propogation de la lumière afin de mesurer le profil longitudinal de puissance. La mesure se base soit sur une opération de corrélation entre deux signaux pour la première technique soit sur une optimisation. Depuis 2021, plusieurs travaux ont été publiés que ce soient des améliorations de ces deux techniques, des nouvelles techniques ou des applications de ces technique, ce qui confirme leur pertinence et leur portée.

Dans leur travail initiral, Tanimura et al. et Sasai et al. ont proposé une détection d'anomalie qui utilise le profil de puissance et ont montré la détection d'anomalies dans des liens avec plusieurs tronçons de fibre, ce qui est très encourageant. Tanimura et al. a notamment étudié numériquement la localisation d'anomalies. Ces travaux n'ont pas proposé d'estimer la valeur des anomalies ou pertes de puissance, ce qui constitue pourtant une information importante pour la prise de décision.

Aperçu du manuscrit et contributions

Dans ce contexte, ce manuscrit étudie la méthode d'estimation de profil de puissance basée sur une corrélation et la possibilité de l'utiliser pour charactériser entièrement, localiser et estimer, des pertes de puissances avec une précision adaptée. Les autres objectifs sont l'étude de la charactérisation des pertes de puissances sur deux topologies particulières, un réseau meshé et un lien très longue distance, ainsi que la charactérisation de nouvelles anomalies comme celles dépendantes de la polarisation.

J'ai effectué mon doctorat entre Nokia Bell Labs (Nozay, France) et le *Laboratoire Traitement et Communication de l'Information (LTCI)* de Télécom Paris (Palaiseau, France) dans le cadre d'une convention *CIFRE (Convention industrielle de formation par la recherche)*. Ce manuscrit est organisé en 4 chapitres dans lesquels je présente le travail accompli pendant ces 3 années de recherche.

Dans le premier chapitre, nous présentons les bases des réseaux optiques, ainsi que des notions fondamentales des systèmes de communications optiques cohérentes. Ensuite, nous nous concentrons sur les défis du monitoring. Premièrement, nous présentons les raisons d'un besoin d'acquérir de larges quantités de données pour optimiser les réseaux optiques du futur. Puis, nous montrons quels types de monitoring est déjà intégrés dans les réseaux optiques modernes et quelles techniques sont développées dans la recherche grâce à l'avènement de la technologie cohérente. Enfin, nous examinons différentes techniques d'estimation de profil de puissance basées sur l'analyse du signal reçu par le récepteur cohérent, incluant les méthodes pionnière. L'étude de ces méthodes sera notre axe prioritaire tout au long du manuscrit.

Dans le deuxième chapitre, nous présentons une méthode pour estimer et localiser les pertes de puissances dans un réseau optique. Cette méthode est basée sur une calibration et l'utilisation d'une techique d'estimation du profil longitudinal de puissance qui utilise un calcul de corrélation. Nous proposons tout d'abord un modèle pour décrire l'évolution du profil de puissance estimé et pour permettre l'estimation de pertes de puissance. Ensuite, nous présentons la méthode proposée qui se base sur une calibration. Enfin, nous effectuons une démonstration expérimentale sur un lien de 300 km and nous étudions la précision de l'estimation de la valeur et de la position des pertes.

Le troisième chapitre se concentre sur l'estimation du profil longitudinal de puissance et sur la détection d'anomalies dans deux cas d'étude: un réseau meshé et un lien très longue distance. Dans le cas d'un réseau meshé, nous évaluons expérimentalement l'amélioration de la précision de charactérisation (à la fois la position et la valeur) des pertes de puissance qu'on obtient en utilisant plusieurs chemins optiques pour le monitoring. Dans le cas du lien très longue distance, nous effectuons l'estimation de profils de puissance sur un lien de plus de 10000 km and nous étudions la détection de plusieurs pertes de puissance.

Enfin, dans le chapitre 4, nous étudions la possibilité de détecter d'autres types d'anomalie avec l'outil d'estimation de profil de puissance. Pour cela, nous proposons une méthode pour estimer et localiser des variations de pertes dépendantes de la polarisation (PDL en anglais) dans un lien optique avec une simple adaptation de l'algorithme et de la méthode proposée dans le chapitre 1. Nous étudions à l'aide de simulations numériques les performances du nouvel outil de monitoring de PDL.

Contents

List of acronyms

AI anomaly indicator.

ASE amplified spontaneous emission.

BER bit error rate.

CD chromatic dispersion.

CFE carrier frequency estimation.

CMA constant modulus algorithm.

CPE carrier phase estimation.

CUT channel under test.

DBP digital back propagation.

DCF dispersion compensating fibers.

DGD dispersion group delay.

DSP digital signal processing.

EDFA erbium-doped fiber amplifier.

FEC forward error correction.

FWM four-wave mixing.

GVD group velocity dispersion.

MIMO multiple-input multiple-output.

MMSE minimum mean square error.

NLSE non-linear Schrödinger equation.

OADM optical add-drop multiplexer.

OCM optical channel monitors.

OOK on-off keying.

OSNR optical signal-to-noise ratio.

OTDR optical time-domain reflectometer.

PDL polarization-dependent loss.

PDM polarization-division multiplexing.

PMD polarization mode dispersion.

QAM quadrature and phase modulation.

QoT quality of transmission.

QPSK quadrature phase shift keying.

ROADM reconfigurable optical add-drop multiplexers.

RP regular perturbation.

SDM spatial division multiplexing.

SMF single mode fiber.

SNR signal-to-noise ratio.

SOP state of polarization.

SPM self-phase modulation.

sps samples per symbol.

SSFM split-step Fourier method.

SSMF standard single mode fiber.

VOA variable optical attenuator.

WDM wavelength division multiplexing.

WSS wavelength selective switch.

XPM cross-phase modulation.

Introduction

Optical fiber transmission systems carry more than 99 % of data traffic around the world [1]. This unchallenged success stems from, first, the physical properties of silica. The attenuation of the propagating electromagnetic field in the fiber is relatively low, of the order of 0.2 dB/km [2], particularly in the infrared region (1.5 μm-1.6 μm). This corresponds to a division by 2 of the signal power every 15 kilometers. In comparison, for copper cables, at a frequency of 60 MHz the attenuation value is of 18 dB/km (G-623, ITU-T). Second, wideband optical amplifications covering tens of nanometers in the infrared region allow these fiber links to transmit data over transocenanic distances by regularly concatenating fiber sections and optical amplifiers. Finally, the advent of coherent technology, the development of powerful digital signal processing (DSP) techniques [3] as well as the development of forward error correction (FEC) algorithms allowed us to approach even further the capacity allowed by Shannon capacity limit.

In the last 30 years, the development of optical fiber transmission systems has made it possible to meet the growing needs for internet usage, which are not expected to slow down. While the percentage of internet users among the global population was of 50 % in 2018, it was expected to go up to 66 % of the population by 2023 [4], which corresponds to 5.3 billion users in total. We note that in 2022 we have reached 5.03 billion internet users worldwide, confirming the tendency [5]. While more and more people use the internet, each user needs a growing numer of devices, specially Internet of Things devices (IoT). While the number of users is expected to go from 4.7 in 2020 to 5.5 billion in 2025, the number of IoT or connected devices is expected to go from 20 in 2020 to 48 billion in 2025 [6]. Apart from the well-established sources of capacity increase, new “mega-applications” are expected to enter the game soon. Such an example is the distributed telescope project Square Kilometer Array (SKA) which is expected to generate huge data streams at different locations on earth (possibly several times beyond the current total internet traffic), with the challenge being to transport, recombine and process those streams in real time.

To respond to the traffic growth while reducing the cost per transmitted bit, optimization of optical networks is necessary. To this end, a first solution is to allow flexibility and dynamicity. With elastic networks [7], grids become flexible and symbol rates can be varied to adapt to the network needs.

For further optimization, the operator needs to know continously the state of the network [8]. For instance, if operators know their current system parameters better, they can add, upgrade or downgrade lightpaths (accommodate new demands) with the absolutely necessary margins [9–11], troubleshoot, run proactive maintenance of faulty components [12] and finally also adapt transmission parameters as fast as possible [13].

Monitoring techniques have been developed before elastic and dynamic networks [14]. However, those techniques usually require external devices or a dedicated channel. For a full optimization, using already deployed transceivers for monitoring is highly desirable to save on costs. In this context, the advent of the coherent technology has given many opportunities for monitoring. Indeed, coherent receivers perform blind or data-aided estimation and compensation of various physical effects [3]. The monitoring of aggregate parameters such as the residual accumulated chromatic dispersion (CD), the accumulated polarization mode dispersion (PMD) or the accumulated PDL was proposed e.g., in the work of [15]. Another straight-forward measurement at coherent receivers is the pre-FEC BER performed by counting the errors on parity bits and without any a priori knowledge of the transmitted sequence which is useful for fault-management applications [16].

As the evolution of the distance-wise power along the link has a significant impact on the overall performance [11], it is an important parameter to monitor. The optical time-domain reflectometer (OTDR) is a device which allows the characterization of the propagation loss along the fiber by analyzing the light which is reflected back in the fiber. Though quite accurate and relevant for the characterization of power anomalies, there are some limitations to its use for a massive monitoring. Its price is likely to limit the scale of its implementation as well as the need for out-of-band signals. Being able to monitor the longitudinal power with telemetry data already available at the receiver side would be all the more relevant for a low-cost and efficient monitoring.

In this context, two pioneer techniques were proposed to estimate the longitudinal power profile, *i.e.,* the power at each point in the link, only by performing a specific DSP on the data from the coherent receiver ([17], 2019) and ([18], 2020). Both works exploit the occurence of distributed non-linear effects during propagation to measure the longitudinal power by proposing either a correlation-based technique [17] or an adaptive digital back propagation (DBP) technique [18]. After 2021, several works have been published consisting in either an improvement of these techniques [19], novel techniques [20] or applications of these techniques [21] confirming the relevance of such topics.

In their initial work, Tanimura et al. [17, 22] and Sasai et al. [18] proposed an anomaly detection scheme using the power profile and showed the detection of anomalies in multi-span links, which is quite promising. In [22], Tanimura et al. investigate numerically the location of anomalies. Those works did not propose to estimate the values of power anomalies, which is an important piece of information for the process of decision making.

Outline and contributions

In this context, this manuscript investigates the correlation-based power profile estimation technique and the possibility to use it to fully characterize, locate and estimate, power losses with an adequate accuracy. Other goals include the investigation of the characterization on two specific link topologies, meshed network and long-haul link, as well as the characterization of new anomalies such as polarization-dependent losses.

I carried out my PhD under an industrial grant within Nokia Bell Labs (Nozay, France) and the *Information Processing and Communications Laboratory (LTCI)* of Telecom Paris (Palaiseau, France). This manuscript is organized in four chapters in which I present the work accomplished during these 3 years of research.

In the first chapter, we review the basics of optical networks as well as the fundamental notions of coherent optical communications systems. Then we focus on the challenge of monitoring. First, we review the reasons behind the need of large amounts of data acquisition to optimize future optical networks. Then, we review what type of monitoring is already integrated in modern optical networks and what techniques are developed in the research world thanks to the advent of coherent technology. Finally, we review and discuss several receiver-based techniques, among them the pioneer ones, to estimate the longitudinal power profile in the link which will be our focus throughout the manuscript.

In the second chapter, we introduce a method to estimate and locate power losses in an optical link. This method is based on a calibration and the use of a longitudinal power profile computed using a correlation-based technique [17, 22]. We first propose a model to describe the evolution of the power profile and to allow for the estimation of power losses. Then, we present the proposed calibration-based method. Finally, we perform an experimental demonstration on a 300-km link and we study the accuracy of the estimation of the value and position of the losses.

The third chapter focuses on the longitudinal power profile monitoring and anomaly detection scheme in two use cases: a meshed network and a long-haul optical link. For the meshed-network case, we experimentally assess the gains in loss characterization (both position and value) accuracy that stems from using multiple lightpaths for monitoring. For long-haul submarine links, we perform the estimation of a power profile over a $>$ 10000-km link and we study the detection of multiple power anomalies.

Finally, in the fourth chapter, we investigate the possibility of detecting other types of anomalies with the power profile estimation tool. To this end, we propose a method to estimate and locate PDL variations in an optical link by a simple adaptation of the algorithm and proposed method in Chapter 1. We investigate through numerical simulations the performance of the new PDL estimator.

Publications list

Journal paper

[J1] **A. May**, F. Boitier, E. Awwad, P. Ramantanis, M. Lonardi and P. Ciblat, "Receiver-Based Experimental Estimation of Power Losses in Optical Networks" in *IEEE Photonics Technology Letters*, vol. 33, no. 22, pp. 1238–1241, November 2021.

International conference papers

[IC1] **A. May**, F. Boitier, A. Courilleau, B. Al Ayoubi, and P. Layec, "Demonstration of enhanced power losses characterization in optical networks" in *Optical Fiber Communications Conference (OFC)*, San Diego, USA, 2022, paper Th1C.6. Presented orally.

[IC2] **A. May**, E. Awwad, P. Ramantanis, and P. Ciblat, "Receiver-based localization and estimation of polarization dependent loss" in *OptoElectronics and Communications Conference (OECC)*, Toyama, Japan, 2022. Presented orally.

[IC3] **A. May**, F. Boitier, A. Meseguer, J. Esparza, P. Plantady, A. Calsat and P. Layec, "Longitudinal Power Monitoring over a deployed 10,000-km Link for Submarine System" in *Optical Fiber Communications Conference (OFC)*, San Diego, USA, 2023, paper Tu2G.3.

[IC4] P. Serena, C. Lasagni, A. Bononi, F. Boitier, **A. May**, P. Ramantanis and M. Lonardi, "Locating Fiber Loss Anomalies with a Receiver-side Monitoring Algorithm exploiting Cross-Phase Modulation" in *Optical Fiber Communications Conference (OFC)*, San Diego, USA, 2023, paper W1H.3.

National conference paper

[FC1] **A. May**, F. Boitier, E. Awwad, P. Ramantanis, M. Lonardi, and P. Ciblat, "Estimation de pertes de puissance pour les réseaux optiques" in *Optique Dijon, Journées nationales de l'optique guidée (JNOG)*, 2021. Presented orally.

Patent

[P1] **A. May**, F. Boitier, E. Awwad, P. Ramantanis and M. Lonardi, "Coherent Receiver Based Localization And Quantization Of Power-related Anomalies In Optical Transport Networks". European application filed in October 2020.

Chapter 1

Monitoring in elastic optical networks

1.1 Introduction

Optical transmissions systems are deployed across the world to allow for an almost instantaneous exchange of data. To optimize optical networks, the observation or monitoring of the state of the links is desirable. Therefore, several research works focused on developing monitoring techniques both low cost and accurate. The advent of the coherent receiver a decade ago brought a lot of opportunities for monitoring through digital signal processing algorithms.

This chapter is organized as follows. We first present the basics of optical communication systems in Section 1.2. We describe a typical optical fiber link composed of fiber spans and several opto-electronic components in which multiple physical effects impact the propagation of light. We also describe the different types of networks in terms of topology or reach. In Section 1.3, we highlight how the need for network optimization motivated a massive monitoring. We then briefly review the existing monitoring in modern optical networks. We also present several digital signal processing (DSP)-based monitoring techniques. In Section 1.4, we present different techniques to estimate the longitudinal power profile of an optical link based on a DSP at the coherent receiver side, which is the core subject of this manuscript.

1.2 Basics on optical communication systems

1.2.1 General design of an optical link

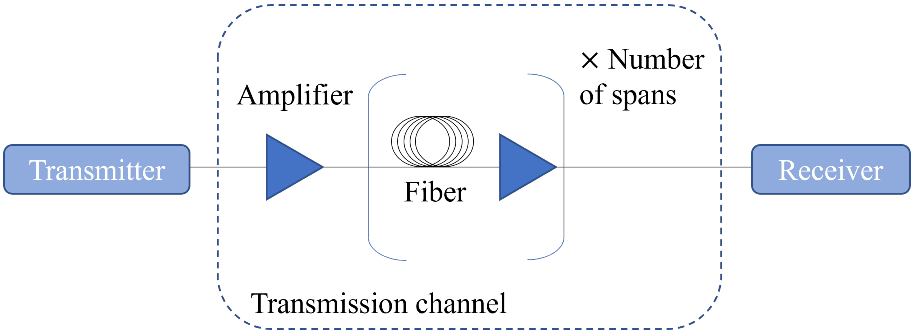

Figure 1.1: Schematic of the general design of an multi-span optical telecom link.

All optical links are composed of three fundamental elements: the **transmitter**, the **transmission channel** and the **receiver**, represented in Fig 1.1. The **transmitter** encodes the information - binary sequence of 0s and 1s - on a signal that can be transmitted into the transmission channel. The **receiver** transforms the optical signal into an electric signal. The **transmission channel** is composed of optical fibers, and all other elements in which light travels such as amplifiers, couplers, filters, etc. The optical fiber is a flexible, transparent fiber made by drawing glass (silica) to a diameter slightly thicker than that of a human hair. Its attenuation is of the order of 0.2 dB/km, which means that after 15 km of propagation, the power of the light is divided by two. Though quite low, amplifiers are required to compensate for the induced total loss to transmit information over hundreds or thousands of kilometers. Every chunk of fiber between two amplifiers is referred to as “span”, cf Fig. 1.1.

Optical amplifiers were introduced to replace electrical regeneration and are massively used both in submarine and in terrestrial long-haul transmissions. Proposed in the late 1980s, rare-earth doped fiber amplifiers and specifically the erbium-doped fiber amplifiers, are the most commonly used in optical fiber communications. Their operation is based on the principle of stimulated emission. The gain medium is a silica fiber doped with erbium ions. The laser pump copropagates with the signal to be amplified in the doped fiber. Erbium ions are excited by the laser pump to high energy levels and can transition back to the ground state thanks to two phenomena: i) stimulated emission of photons of the same wavelength as the one of the incoming signal photon, allowing for the amplification of the signal and ii) spontaneous emission, generating noise, which is known as amplified spontaneous emission (ASE). An erbium-doped fiber amplifier (EDFA) typically provide gains of 20 dB or more, which allows for the compensation of a propagation loss over 100 kilometers of optical fibers with a 0.2 dB/km attenuation. Other optical amplifiers include distributed Raman amplifiers and semiconductor amplifiers.

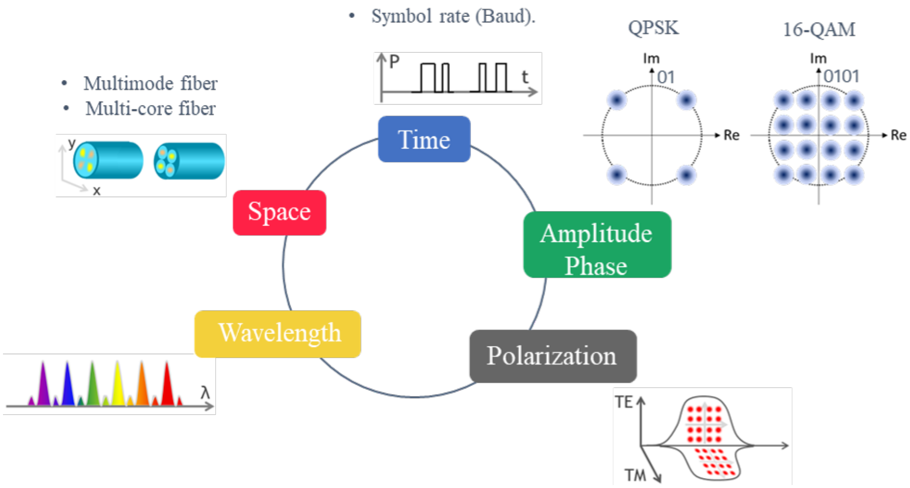

Figure 1.2: Different dimensions over which the light is modulated.

To transmit more information per unit of time, the five dimensions of light are being used: time, wavelength, quadrature (amplitude and phase), polarization and space, as shown in Fig 1.2. **Time** (or equivalently frequency) is the first dimension over which the light was modulated. The symbol rate R_s is simply given by the modulation rate of the light intensity. A symbol corresponds to the state of the optical waveform and can represent or convey one or several bits of data. On-off keying (OOK) is an example of this type of modulation where only two amplitudes of light are used to represent the two binary numbers 0 and 1. In this case, the bit rate R_b is equal to the symbol rate R_s.

Coherent receivers, which are receivers sensitive to both the phase and the amplitude of an optical field, reemerged as a key tool to achieve higher bit rates, empowered by the innovations in high-speed electronic devices and digital signal processing. Information could then be encoded not only on the intensity of the field but also on its phase : **quadrature** modulation. With this type of modulation, the bit rate is $R_b = \log_2(M) \cdot R_s$, where M is the number of discrete symbols in the complex plane. The value of $\log_2(M)$ corresponds to the number of bits which can be represented by a symbol. In Fig 1.2, we represented quadrature phase shift keying (QPSK) modulation format where the information is coded onto four phase states, the amplitude E being constant. Each symbol k is of the form $E \cdot \exp(i(k\pi/2+\pi/4))$ with $k = \{0, 1, 2, 3\}$. To increase further the bit rate, quadrature and phase modulation (QAM) formats consider symbols for which both the phase and the amplitude are varied. For example, 16-QAM modulation format considers 16 symbols where each symbol carries 4 bits. Hence, for a fixed symbol rate, the bit rate of QPSK (respectively 16-QAM) is doubled (resp. multiplied by four) compared to the bit rate of OOK.

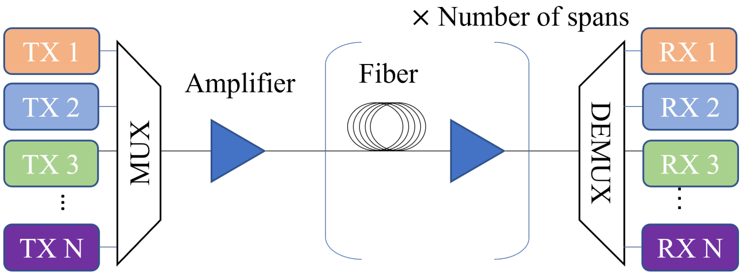

Figure 1.3: Schematic of a general wavelength division multiplexing (WDM) link.

WDM technology consists in combining N channels operating at distinct **wavelengths** in the same optical fiber, as shown in Fig 1.3. Despite the high density of channels, the weak linear cross talk between channels at low power limits the degradation of the quality of signal during its propagation. The different wavelengths are combined together with the use of a multiplexer at the input of the fiber and then separated before the receiver with a demultiplexer. The total data rate is equal to the single channel rate multiplied by the number of channels. In products nowadays, WDM technology covers the whole C+L-band corresponding to 1528.77 to 1610.06 nm. What has helped making this technique a standard one is, among others, the possibility of using a single EDFA to amplify the whole C-band. According to the International telecommunications union (ITU) standard, for the C-band, the number of channels is 50 with a 100 GHz-grid, from 1528.77 to 1567.95 nm. In recent years, researchers are looking into extending the bandwidth of transmission links by exploring amplification techniques for the S-band and beyond [23].

Coherent detection, when implemented in a polarization-diversity configuration, gives access to the state of **polarization** of the incoming light. This feature unlocks a new multiplexing opportunity: polarization-division multiplexing (PDM). PDM consists in sending two different sequences of symbols on two orthogonal polarization states of the electric field. For a given symbol rate, it multiplies the inital bit rate by a factor two. Therefore, for a PDM quadrature modulation, the bit rate per WDM channel is $R_\text{b} = 2 \cdot \log_2(M) \cdot R_\text{s}$.

In more recent years, **space**, the remaining degree of freedom, is studied to increase further the total rate of a fibre link. spatial division multiplexing (SDM) techniques include: adding more single mode fiber (SMF) bundles in a cable, using multi-mode fibers, or using multi-core fibers, or even any combination of both multi-mode and multi-core [24]. Apart from adding more fibre bundles, the other SDM techniques are not yet implemented in today's transmission systems.

1.2.2 Physical effets during light propagation

When light propagates inside an optical fiber, due to the interactions with materials, several effects will alter the performance of the transmission. When an incoming electromagnetic wave with a complex amplitude $\boldsymbol{E}(z,t)$ propagates into a medium, an electric dipole moment can be acquired by the medium, which is a distortion of the distribution of charges. The total polarization $\boldsymbol{P}$ induced by electric dipoles satisfies the general relation ([2], Section 1.3):

$$\boldsymbol{P} = \epsilon_0(\chi^{(1)} \cdot \boldsymbol{E} + \chi^{(2)}\boldsymbol{E}\boldsymbol{E} + \chi^{(3)}\boldsymbol{E}\boldsymbol{E}\boldsymbol{E} + ...), \tag{1.1}$$

where ϵ_0 is the vacuum permittivity and $\chi^{(l)}(l = 1, 2, ...)$ is the l^{th} order susceptibility. The first term is the dominant contribution term to $\boldsymbol{P}$. The linear susceptibility $\chi^{(1)}$ is related to the absorption coefficient and the dispersion (refractive index) of the material. Effects on the propagation of light are **attenuation** and **chromatic dispersion**. The second-order susceptibility $\chi^{(2)}$ is responsible for non-linear effects as second-harmonic generation and sum-frequency generation. However, materials like optical fibers made of silica do not support any even order optical non-linearities. Therefore, the lowest **non-linear effects** in optical fibers are those originating from the third-order susceptibility $\chi^{(3)}$. We now present succinctly those effects.

Linear propagation effects

i) Power attenuation In an optical fiber, with $E(z,t)$ the amplitude of the scalar optical field, the power $P(z) = \langle\, |E(z,t)|^2 \,\rangle$ decreases exponentially with the distance z during the propagation: $P(z) = P_0 \cdot \exp(-\alpha z)$, where P_0 is the power in Watt at the beginning of the transmission, z the distance in [km], and α the attenuation coefficient [km^{-1}]. We denote the frequently used attenuation coefficient expressed in dB by α_{dB}. The evolution of the amplitude of the optical field is described by the equation:

$$\frac{\partial E(z,t)}{\partial z} = -\frac{\alpha}{2}E(z,t). \tag{1.2}$$

In optical fibers, the attenuation coefficient depends on the wavelength of the signal. The main sources for attenuation are Rayleigh scattering and absorption of the material. Standard single mode fiber (SSMF) are the most commonly used for telecommunications since they have a low loss coefficient $\alpha_{\text{dB}} = 0.2$ dB/km at 1550 nm ([2], 1.2.2).

ii) Chromatic dispersion (CD) CD is a linear effect resulting from the wavelength dependence of the refractive index $n(\omega)$ where ω is the angular frequency of the optical field. To describe this dependence, we can approximate the propagation constant $\beta(\omega)$ using a Taylor expansion around the angular frequency ω_0:

$$\beta(\omega) = \frac{n(\omega)\omega}{c} = \beta_0 + \beta_1(\omega - \omega_0) + \frac{\beta_2}{2}(\omega - \omega_0)^2 + \frac{\beta_3}{6}(\omega - \omega_0)^3 ... \tag{1.3}$$

where c is the velocity of light, β_i is the i-th derivate of $\beta(\omega)$ with respect to ω at the point $\omega = \omega_0$.

β_0 [km^{-1}] and β_1 [ps/km] which is the group velocity are not responsible for any signal distortion. However, the group velocity dispersion (GVD) β_2 [ps^2/km] is the acceleration of the spectral components and is responsible for the pulse broadening in the time domain and interference between symbols. β_3 [ps^3/km] is the GVD slope or the variation of GVD as a function of the wavelength.

The dispersion coefficient $D(\lambda)$, dependent on the wavelength λ of the optical field and expressed in [ps/nm/km], is linked to the GVD β_2 through

$$D(\lambda) = -\frac{2\pi c}{\lambda^2}\beta_2. \tag{1.4}$$

For a SSMF, the usual dispersion coefficient $D_0 = D(\lambda_0)$ is around 17 ps/nm/km for $\lambda_0 = 1550$ nm. D_0 can be quite different for other types of fibers. For example, for LEAF fibers, D_0 is between 4.5 and 6 ps/nm/km, for $\lambda_0 = 1565$ nm [25]. The evolution of the optical field only in presence of chromatic dispersion is governed by the equation:

$$\frac{\partial E(t,z)}{\partial z} + i\frac{\beta_2}{2}\frac{\partial^2 E(t,z)}{\partial t^2} - \frac{i\beta_3}{6}\frac{\partial^3 E(t,z)}{\partial t^3} = 0 \tag{1.5}$$

Solving Eq. (1.5) allows us to write the impulse response of chromatic dispersion $d_{sz}(t)$ from coordinate s to z with $s < z$:

$$d_{sz}(t) = \mathcal{F}^{-1}\{\exp(-i\frac{\beta_2}{2}(z-s)\omega^2 - i\frac{\beta_3}{6}(z-s)\omega^3)\}(t), \tag{1.6}$$

where $\mathcal{F}$ is the operator of the Fourier transform. We note that this filter corresponds to the application of CD for a distance $z-s$. The filter compensating for the same amount of CD is denoted by $d_{zs}(t)$.

Before the deployment of coherent detection, the CD was compensated using dispersion compensating fibers (DCF) to ensure the recovering of data. DCF have a dispersion coefficient D whose value is large and negative. In dispersion managed (DM) systems, units of DCF are placed between positive dispersion fiber spans, generally in optical fiber inter-stage, and an accumulated CD close to 0 ps/km/nm can be achieved. In modern coherent systems, the accumulated CD can be compensated with digital filters at the receiver, as presented in Section 1.2.3.

Non-linear effects

For intense electromagnetic fields, non-linear effects inside optical fibers are no longer negligible. Those effects can be encompassed under the notion of four-wave mixing (FWM) since they all involve the interactions between four waves at $\omega_1, \omega_2, \omega_3$ and ω_4. In telecom fibers, FWM interactions include mainly scattering effects such as Raman and Brillouin, and phase modulation effects (also called Kerr effects) such as self-phase modulation (SPM) and cross-phase modulation (XPM). In practice, SPM corresponds to the interaction of one channel with itself and XPM corresponds to the interaction of one channel with another.

The non-linear Schrödinger equation describes the evolution of an optical field of amplitude $E(z,t)$. We write it first in the case of a scalar optical field in presence of three effects: attenuation, chromatic dispersion and third-order non-linear phase modulation effects as:

$$\frac{\partial E(z,t)}{\partial z} + \frac{\alpha}{2}E(z,t) + i\frac{\beta_2}{2}\frac{\partial^2 E(z,t)}{\partial t^2} - i\frac{\beta_3}{6}\frac{\partial^3 E(z,t)}{\partial t^3} - i\gamma|E(z,t)|^2 E(z,t) = 0 \quad (1.7)$$

where γ is the non-linear coefficient introduced as:

$$\gamma = \frac{2\pi}{\lambda}\frac{n_2}{A_{\text{eff}}}, \quad (1.8)$$

where n_2 is the non-linear index and A_{eff} the effective mode area of the fiber.

To study the impact of the Kerr effect on WDM transmissions, the Gaussian noise model was derived [26] followed by the enhanced Gaussian noise model [27]. Other research works include those regarding the compensation of non-linear effects. One popular technique for the compensation of physical effects is the digital back propagation (DBP) [28]. The idea is to solve the inverse of the non-linear Schrödinger equation (NLSE) and to numerically apply it to the received signal. Since DBP techniques might be quite complex to implement (for instance DBP dealing with inter-channel effects), some works propose to consider a perturbation analysis to construct the non-linearity compensating algorithm [29].

Polarization effects

Because of asymmetries in the fiber stress and geometry arising from the fabrication process and deployment conditions, polarization effects, linear and non-linear, will alter the propagation of the optical field. The polarization state of an optical field can be described through the Jones formalism as a linear combination of two linearly polarized fields $(1,0)^T$ and $(0,1)^T$. In this basis, the amplitude of the optical field is described by the following vector: $\boldsymbol{E}(z,t) = (E_x(z,t), E_y(z,t))^T$.

i) Polarization cross talk and Polarization mode dispersion (PMD) Because of the birefringence of the fiber, polarizations travel at difference group velocities. Since thermal and mechanical stresses vary over time and along the fiber, the accumulated dispersion group delay (DGD), which is the delay between the fastest and slowest polarization state, is not constant. This phenomenon is known as the PMD. To assess the strength of this phenomenon, we rely on the PMD coefficient D_{PMD} measured in ps/$\sqrt{\text{km}}$. From this coefficient, we can estimate the mean accumulated DGD $\overline{\Delta\tau}$ through $\overline{\Delta\tau} = D_{\text{PMD}} \cdot \sqrt{L}$ ([2], Section 1.2.4) with L being the propagation distance in kilometers.

A fiber span can be modeled as the concatenation of independent randomly oriented birefringent sections. To describe this, we introduce the transfer function $\boldsymbol{H}_{\text{fiber}}$ that consists in a product of N_{b} independent unitary Jones matrices:

$$\boldsymbol{H}_{\text{fiber}} = \prod_{i=1}^{N_{\text{b}}} \boldsymbol{R_i} \cdot \begin{pmatrix} \exp(-i(\omega\tau_i/2 + \phi_i/2)) & 0 \\ 0 & \exp(+i(\omega\tau_i/2 + \phi_i/2)) \end{pmatrix} \cdot \boldsymbol{R_i}^{-1}, \quad (1.9)$$

where ϕ_i and τ_i are respectively the phase shift and the DGD of the i^{th} segment. The rotation matrix $\boldsymbol{R_i}$ describes the random mismatch between the incident polarization states of the signal and the principal polarization states of the birefringent element i. This equation encapsulates both the cross talk, *i.e.,* random coupling between polarization states and the PMD.

ii) Polarization-dependent loss (PDL) PDL refers to the polarization dependence of the insertion loss of an optical element. It can be induced by EDFAs, wavelength selective switch (WSS), etc [30]. This effect will be described in details and studied in the Chapter 4.

iii) Vector form of the NLSE The NLSE written in Eq. (1.7) can be written in a vector form to take into account polarization effects. The Manakov equation is commonly used to describe the evolution of the optical field $\boldsymbol{E}(t,z)$ in the case of a random birefringence ([31], Sections 6.6.2-6.6.3):

$$\begin{aligned}\frac{\partial E_j(z,t)}{\partial z} + \frac{\alpha}{2}E_j(z,t) + \beta_{1,j}\frac{\partial E_j(z,t)}{\partial t} + i\frac{\beta_2}{2}\frac{\partial^2 E_j(z,t)}{\partial t^2} - i\frac{\beta_3}{6}\frac{\partial^3 E_j(z,t)}{\partial t^3}\\ - i\frac{8}{9}\gamma(|E_x(z,t)|^2 + |E_y(z,t)|^2)E_j(z,t) = 0 \quad (1.10)\end{aligned}$$

with $j = \{x, y\}$. Note that the 8/9 coefficient weighing the Kerr effect contribution results from the averaging of PMD due to random birefringence. Also, this equation does not explicitely show the linear polarization crosstalk that we presented earlier.

1.2.3 Digital signal processing

Thanks to the advent of the coherent technology, several DSP techniques have been developped to mitigate the presented physical parameters as well as impairments at the transmitter and receiver side. In Fig. 1.4, we show a figure drawn in [3] describing the different subsystems in a digital coherent receiver including DSP operations. We present here the main operations of the DSP chain commonly used [3, 32] in commercial transceivers.

i) Clock recovery After analog-to-digital conversion of the output of the photodiodes, the signal is sampled at f_s/R_s samples per symbol (sps) with f_s the sampling rate of the analog-to-digital converters and R_s the symbol rate of the transmitted signal. The signal is resampled at 2 sps, minimum value to satisfy the Shannon-Nyquist theorem. Since the transmitter and the receiver do not share a common reference clock, thus they have a slightly different frequency. As a consequence, the symbol rate seen by the receiver R_s' is different from R_s. The purpose of the clock

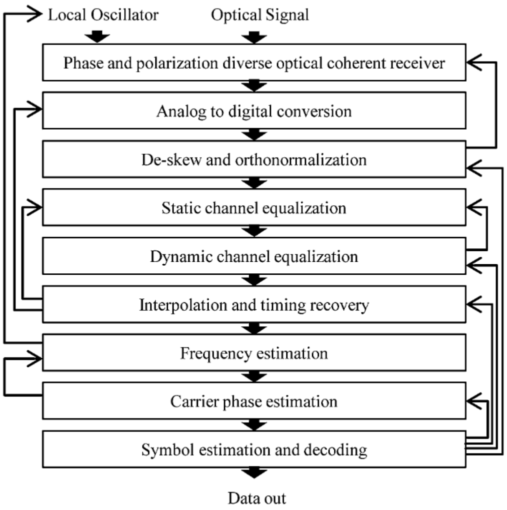

Figure 1.4: Subsystems in a digital coherent receiver including DSP operations. Source: [3].

recovery is to track this difference and compensate it. In laboratory experiments, since the waveforms are generally short (few milliseconds), clock tracking is not necessarly required as the timing mismatch can be corrected by a linear compression (or dilatation) of the time axis of the receiver.

ii) CD compensation The accumulated CD can be digitally compensated by a filter. This compensation is usually performed in the frequency-domain [33]. Therefore, for a propagation over L [km] the filter to be applied is the inverse of the Fourier transform of $d_{0,L}(t)$ defined in Eq. (1.6).

iii) Adaptive equalization and polarization demultiplexing Because of time-varying polarizations effects, an adaptive filter is needed to recover the transmitted polarizations. This is performed by an adaptive multiple-input multiple-output (MIMO) that separates the polarization tributaries of the signal, compensates PMD and residual CD [15] and applies the matched filter. One time-domain equalizer commonly used for PDM-QPSK modulated signals is the constant modulus algorithm (CMA). The CMA is a blind gradient-descent algorithm whose goal is to minimize the squared error between the modulus of the outputs symbols and a target constant modulus. Other data-aided MIMO equalizers can be also used found in literature such as frequency-domain equalizers in [34].

iv) Frequency and phase estimation Coherent detection is a homodyne detection with two different lasers, a local oscillator laser at the receiver side with an angular frequency ω_{LO} and the laser the generated the signal at the transmitted side with an angular frequency ω_s close to ω_{LO}. The goal of the carrier frequency estimation (CFE) is to estimate and compensate for the frequency detuning $\omega_{LO} - \omega_s$ [35]. Then, the carrier phase estimation (CPE) allows the compensation of the phase variations due to the non-zero spectral width of the lasers. There exists several algorithms to perform this operation such as the blind search algorithm [36] or, in the case of QPSK, the Viterbi-Viterbi algorithm [37]. The latter consists in computing the 4^{th} power of the received field to remove the signal modulation, estimating the phase noise and finally compensating it.

1.2.4 Networks architecture

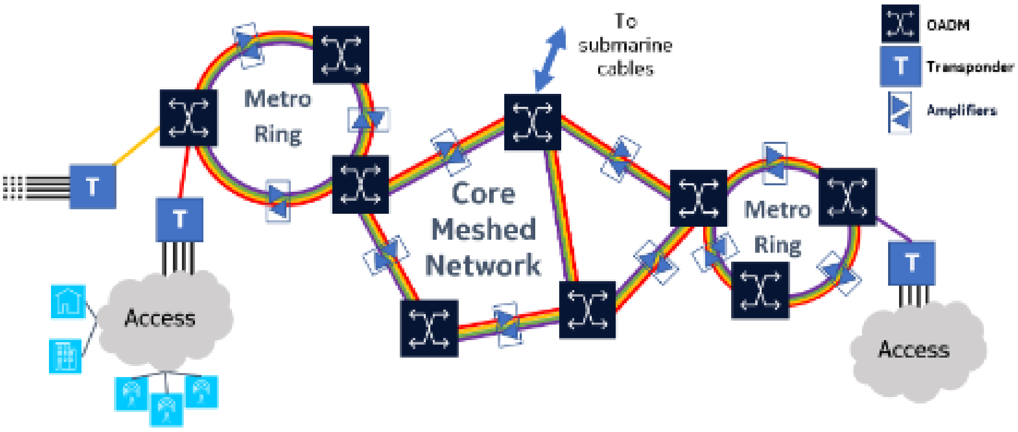

Figure 1.5: Representation of different network topologies. Source: [38].

Thanks to the advent of high-bandwidth electronics, high-performance DSP techniques and small-footprint optical and opto-electronic devices, high speed optical communications have taken such a predominance in todays communications that it is estimated that more than 4 billion kilometers of optical fibers have been deployed around the Earth. Optical networks are organized in rings or meshes and are classified by their applications and the length of their links. In Fig. 1.5, we show a schematic representation of these networks.

The access network is the one which is closer to the end-user. It provides subscribers with connectivity to their immediate service provider, which can be wireless mobile network base stations, enterprises or residential endpoints. The concerned optical links are under 100 km and do not have in-line amplifiers. The metropolitan

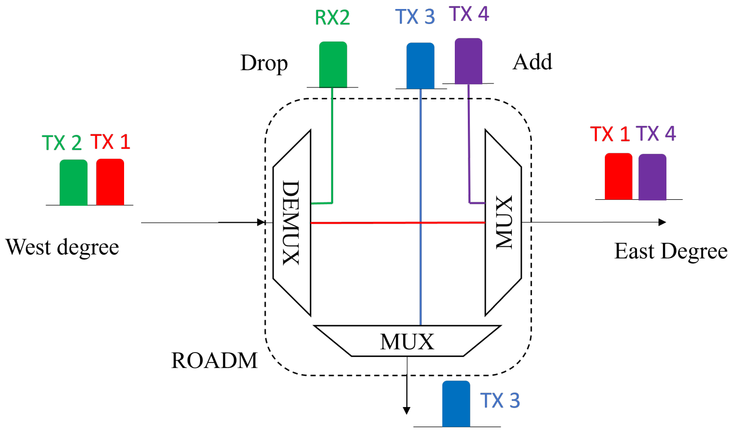

Figure 1.6: Schematic diagram of an optical add-drop multiplexer (OADM).

and the core networks have similar applications, they both interconnect networks. However, metropolitan links usually refer to optical links with propagation distances of the order of several hundreds of kilometers while the core - which can also be referred to as backbone network - can connect different countries and continents through submarine links which can be of thousands of kilometers long.

The transmission of data from one network to another is performed with the use of coherent WDM technology, that we presented in Section 1.2.1. Optical channels are extracted at nodes thanks to OADMs to be transported to its destination. The OADM is the main component of optical nodes and the one which allows WDM technology to be most interesting. At each OADM, WDM channels can be added and dropped, which allows each of the channels to follow its own path. In Fig 1.6, we show coarsely how an OADM operates. We have two channels TX 1 (transmitter) and TX 2 coming towards the OADM. RX (receiver) 2 is dropped while TX 1 continues its propagation into another fiber after being multiplexed with the added signal TX 4. TX 3 is added also in this OADM but goes into another direction. Because of the dynamisation of networks, reconfigurable optical add-drop multiplexers (ROADM) were developed to allow for the possibility to reconfigure the lightpaths to react to possible events.

Now that we have presented the basics of optical communication systems, we will focus on the expected evolution of monitoring to optimize future optical networks.

1.3 Towards massive monitoring

The goal of monitoring is to provide data to optimize the use of a system [8]. In the case of optical networks, monitoring is a part of the optimization loop in Fig.

1.7. Monitoring information about the state of the network is collected. Analyses are performed and depending on their outputs, specific configuration changes are applied to the network.

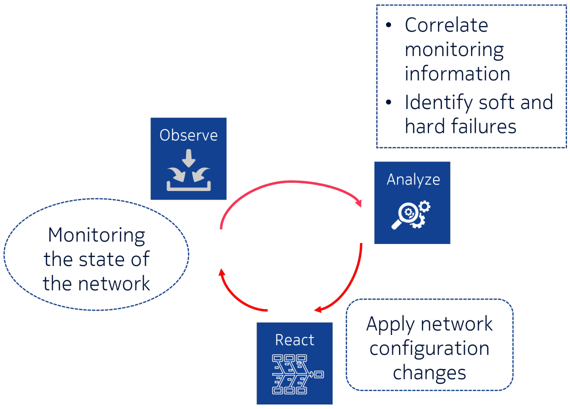

Figure 1.7: Network optimizing loop.

1.3.1 Monitoring for the optimization of future optical networks

Future optical networks increasingly require getting accurate data for a full optimization, whether it be at the design stage or during operation.

"Design" margins account for the intrinsic inaccuracy of performance prediction tools and for the limited knowledge of the network, including but not limited to physical parameters or performance of optical components, at the design stage [10]. To reduce them, one way is to reduce the uncertainties on the input parameters of those prediction tools. For example, using machine learning, in [39], Seve et al. managed to reduce uncertainties on power levels and noise figures of amplifiers. This increased the accuracy of the signal-to-noise ratio (SNR) estimation, leading to a reduction of the quality of transmission (QoT) prediction error from 1.8 to 0.1 dB. In [11], a study is proposed on the link between the uncertainties of physical parameters and the overall performance uncertainty. Ramantanis et al. show how valuable it is to monitor physical parameters such as the non-linear parameter γ and the fiber attenuation α, instead of only monitoring parameters describing the overall performance such as the SNR. They discuss the impact of each parameter (including but not limited to the noise figure of amplifiers, the fiber attenuation, the span length or the power per channel) uncertainty on the performance uncertainty, providing guidelines on which is most important to monitor. Ramantanis et al.

found that the fiber attenuation was the parameter whose uncertainty had the most impact on the performance uncertainty and was therefore the most important to monitor.

To fully optimize optical networks, a continuous observation throughout operation is necessary to close the control loop drawn in Fig. 1.7. Because of the dynamicity of elastic optical networks [7], a continuous monitoring is required to ensure an uninterrupted optimization. For example, in [40], optical performance monitoring such as optical signal-to-noise ratio (OSNR) or power is demonstrated during channel add/drop scenarios at the millisecond scale. In low margins network, anomaly detection techniques are necessary to ensure reliability. The goal is to get as much information as possible about the anomaly whether it be its type, its location or its amplitude. To automate network, accurate monitoring is required to make the most adapted decisions. Decisions may include repairment, rerouting [41] or a transmission parameters adjustment using for example "hitless" reconfigurations [13]. A "hitless" reconfiguration is a reconfiguration without any service interruption, which for example could mean the requirement of a minimum bit error rate (BER) at all times.

Finally, optimization cannot be complete with expensive techniques. Therefore, a continuous, accurate and low cost monitoring is required for optical networks to be low margin, hitless and automated.

1.3.2 Monitoring in modern optical networks

The need for monitoring in optical networks has been defined in early 2000s and updated since them [42] with a review of the several parameters to be monitored and the activities that monitoring helps to perform. The latter includes configuration management such as channel activation, addition of new channels, fault management to detect and isolate faults and degradation management to detect degradations before a fault occurs.

Many of the reviewed parameters are monitored in modern optical networks at different scales which are shown in Fig. 1.8 to multiply sources of information.

For example, in commercial ROADM degree cards, the power per channel, the wavelength and the OSNR can be monitored by an optical channel monitors (OCM). At the receiver side, the pre-forward error correction (FEC) BER is recovered by counting the errors on parity bits. The input power and output powers of amplifiers and transceivers are also monitored.

More recently, because of the high increase in compacity of components, com-

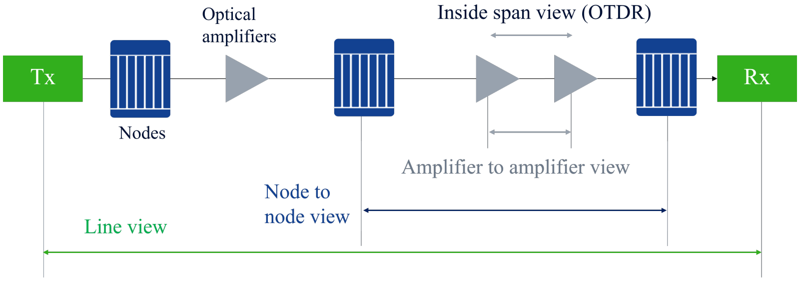

Figure 1.8: Monitoring at different scales.

plex optical devices become pluggable and can be placed at key locations in the network. To monitor the fiber span state, pluggable optical time-domain reflectometer (OTDR) modules are commercialized. By analyzing the light which is reflected back in the fiber, the OTDR allows for the characterization of the propagation loss along the fiber. An important downside is its price, which limits the scale of its implementation.

1.3.3 Towards receiver-based monitoring

Several works in early 2000s proposed monitoring techniques. In [14], the authors present existing monitoring techniques of multiple parameters including the OSNR, the CD, the PMD or the BER. Though a few techniques are available for each parameter, they are very specific to each parameter. Plus, some of them even require the modification of the transmitter or addionnal costly devices. All of that increases significantly the monitoring cost if all parameters are monitored.

The advent of the coherent technology has given many opportunities to cut the monitoring cost. Indeed, coherent receivers perform blind or data-aided estimation and compensation of various physical effects. One can take advantage of these estimated parameters for monitoring purposes, therefore saving cost.

For instance, the authors in [15] propose to use the computed coefficients from the adaptive equalizer to estimate the residual accumulated CD, the accumulated PMD or the accumulated PDL. This technique allows the enhancement of the knowledge on the network which can be useful for reducing margins or for creating digital twins, a tool for optimization.

Monitoring of physical parameters can also allow for the proactive detection of anomalies. For example, in [12], Boitier et al. analyze state of polarization (SOP) variations from coefficients of the filter obtained by the CMA and through machine learning, they are able to recognize fiber breaks before they occur.

More recently, one powerful DSP-based technique was proposed to estimate the longitudinal power of an optical link, *i.e.,* the channel power at each point along the optical path. Other DSP-based power profile estimation techniques were proposed, based *a priori* on SPM effects, and they all act as anomaly detection tools. Another technique based on XPM effects is proposed to detect and locate anomalies [43].

In this manuscript, we are going to focus on power profile estimation techniques and we are going to present them in details in the following section.

1.4 Power profile estimation techniques

Since the first power profile estimation technique proposed in [17] and developped in [22] by Tanimura et al., other techniques were proposed. The different power profile estimation algorithms exploit non-linear effects occuring during the propagation of a signal along an optical link. In this section, we thus present the split-step Fourier method (SSFM), which is a numerical method to solve the NLSE. We also present a perturbative way to model non-linear effects, which is the regular perturbation (RP) method. Secondly, we lay out the two pioneer power profile estimation techniques by Tanimura et al. [17] and by Sasai et al. [18] which were proposed in 2019 and 2020 respectively, thus at the beginning of my PhD. Thirdly, we describe several additional power profile estimation techniques which are either improvements of the pioneer ones or novel ones. Finally, we collect some applications of these techniques reported in the recent literature.

1.4.1 Modeling of non-linear effects: SSFM or RP and eRP methods

We have seen that the NLSE describes the propagation of an optical field in an optical fiber, encapsulating various physical effects including non-linear effects. Since the NLSE does not yield analytical solutions, numerical methods are required to compute their approximate solutions.

SSFM

The SSFM [31] is a direct numerical solution of the NLSE and is the most popular and commonly used one. We present here the principle of the SSFM. We look back at the NLSE written in Chapter 1 in Eq. (1.7) in the scalar case:

$$\frac{\partial E(z,t)}{\partial z}+\frac{\alpha}{2}E(z,t)+i\frac{\beta_2}{2}\frac{\partial^2 E(z,t)}{\partial t^2}-i\frac{\beta_3}{6}\frac{\partial^3 E(z,t)}{\partial t^3}-i\gamma|E(z,t)|^2E(z,t)=0. \quad (1.11)$$

The main idea of the SSFM is to split the equation into two terms, linear and non-linear to allow for the numerical resolution of the equation:

$$\frac{\partial E(t,z)}{\partial z}+\hat{L}E(t,z)+\hat{N}E(t,z)=0 \quad (1.12)$$

Where $\hat{L}$ is the differential linear operator accounting for the attenuation and the dispersion and $\hat{N}$ is the non-linear operator accounting for the non-linear effects. The key assumption to the SSFM is that these two types of effects can be considered independent if applied in a small section dz of fiber. Therefore, to solve this complex equation, the SSFM consist in propagating in the optical fiber by short-distance segments dz of fiber, and applying consecutively the linear effects and the non-linear effects N times, $N = L/dz$ being the number of segments and L the length of the fiber. The SSFM is relatively fast because it takes advantage of the fast Fourier transform to apply the CD, an all-pass filter, in the frequency domain. In practice, the segment dz is non-uniform. For example, dz can be varied as a function of the power in the link to optimize the computational time. Polarization effects can be modeled in the linear step of the SSFM using Jones matrices.

Though the SSFM provides a numerical solution of the NLSE, it does not provide any analytical solutions. A closed-form approximation of the received field is desirable for computing efficiency, as well as for understanding physical effects to provide relevant compensation, equalization or monitoring techniques. Therefore, much research has been dedicated to the search of approximate analytical solutions of the NLSE. This includes, among others, linearization techniques [44–46], the use of Volterra series [47, 48] and the RP method [49, 50].

RP method

The RP method was initially proposed in [49]. This iterative and perturbative method provides a closed-form approximation of the received field. To present the general idea of the method, we use some of the derivations written in [50]. A summary diagram is shown in Fig. 1.9, where the SSFM is compared to the first-order of the RP, called RP1. We see that, in the case of SSFM, the electric field $E(t, L)$ after a distance L is computed by applying successively N blocks "$\mathcal{L}$" implementing linear effects and N blocks "$\mathcal{N}_s$" implementing Kerr effects, as explained before. The non-linear block $\mathcal{N}_s$ accounts for all-order non-linearities: $\mathcal{N}_s(U) = U \cdot \exp(-i\gamma|U|^2 L_{\text{eff}} \cdot dz)$, where L_{eff} if the fiber effective length.

In the case of the RP1, the electric field $\tilde{E}(\omega, L)$ at an angular frequency ω after a distance L can be written as $\tilde{E}(L, \omega) \simeq \tilde{E}_0(L, \omega) + \gamma \tilde{E}_1(L, \omega)$. $\tilde{E}_0(L, \omega)$ is the unperturbed solution of the NLSE, only affected by linear effects. $\tilde{E}_1(L, \omega)$ accounts for the first-order perturbation of the Kerr effect. It can be written as [49]:

$$E_1(L, t) = -i \int_0^L \gamma(z) h_{zL}(t) \otimes \mathcal{N}_0(h_{0z}(t) \otimes E_0(0, t))\, dz \tag{1.13}$$

where $\otimes$ corresponds to the convolution product and $h_{sz}(t)$ is the linear impulse response from coordinate s to z:

$$h_{sz}(t) = \mathcal{F}^{-1}\{\sqrt{\mathcal{G}(z, s)} \cdot \exp(-i\frac{\mathcal{C}(z, s)}{2}\omega^2 - i\frac{\mathcal{C}_s(z, s)}{6}\omega^3)\}, \tag{1.14}$$

where $\mathcal{G}(z, s)$, $\mathcal{C}(z, s)$, $\mathcal{C}_s(z, s)$ are the cumulated gain, dispersion and dispersion slope, respectively, between coordinate s and z, respectively

$$\mathcal{G}(z, s) = \exp(\int_s^z (-\alpha(x) + \sum_k \log(\mathcal{G}_k)\delta(x - z_k))\, dx)$$

$$\mathcal{C}(z, s) = \int_s^z \beta_2(x)\, dx$$

$$\mathcal{C}_s(z, s) = \int_s^z \beta_3(x)\, dx.$$

$\mathcal{G}_k$ is the gain of the amplifier located at coordinate z_k. $\delta(x)$ is Dirac's delta function, $\alpha(x)$, $\beta_2(x)$ and $\beta_3(x)$ are the fiber attenuation, dispersion and third-order dispersion at coordinate x, respectively. We note that this formalism which includes amplifiers and the variation of physical parameters along z allows the application of the method to various forms of optical links. Finally, $\mathcal{N}_0$ is the non-linear parameter of the RP method defined as:

$$\mathcal{N}_0(U) = |U|^2 U. \tag{1.15}$$

In [49], an enhanced RP method is proposed, the eRP, with an updated non-linear parameter $\mathcal{N}_{\text{P}}$ which replaces $\mathcal{N}_0$ in Eq. (1.13):

$$\mathcal{N}_{\mathrm{P}}(U) = (|U|^2 - 2\mathcal{P}(z))U, \tag{1.16}$$

where $\mathcal{P}(z) = P \cdot \mathcal{G}(0,z)$ with P the power at $z = 0$. In Fig. 1.9.b , an algorithm computing Eq. (1.13) is shown, assuming a uniform discretization grid Δz for the integral in z. $E_1(L,t)$ is the sum of several lines where each line is the concatenation of one non-linear block $\mathcal{N}$ and linear $\mathcal{L}$ blocks. The non-linear block implements $-i\gamma\mathcal{N}_{\mathrm{P}}(\mathcal{U})\Delta z$ whereas the linear block implements $h_{sz}(t)$ with $z = s + \Delta z$.

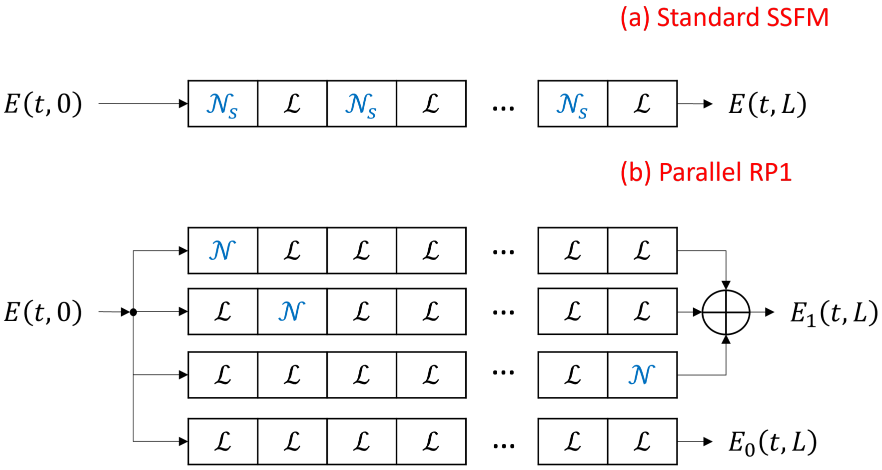

Figure 1.9: Schematic diagram of the SSFM and RP algorithms, inspired from [50].

We see that each line can be computed independently from the others, which can save some computation time if a parallel simulation architecture is available.

To conclude, we have presented two ways to model nonlinear effects, the SSFM and the RP1 method. The SSFM is a direct numerical resolution of the NLSE while the RP method provides an analytical solution at first-order. The latter allows an easier apprehension of physical effects useful for designing compensation or smart monitoring techniques.

1.4.2 Pioneer power profile estimation techniques

We now present the two pioneer power profile estimation techniques. First, we show their longitudinal power profile. Then, we present both power profile estimation algorithms. Finally, we present the anomaly detection scheme that they propose and discuss on the opportunites that it offers to monitoring.

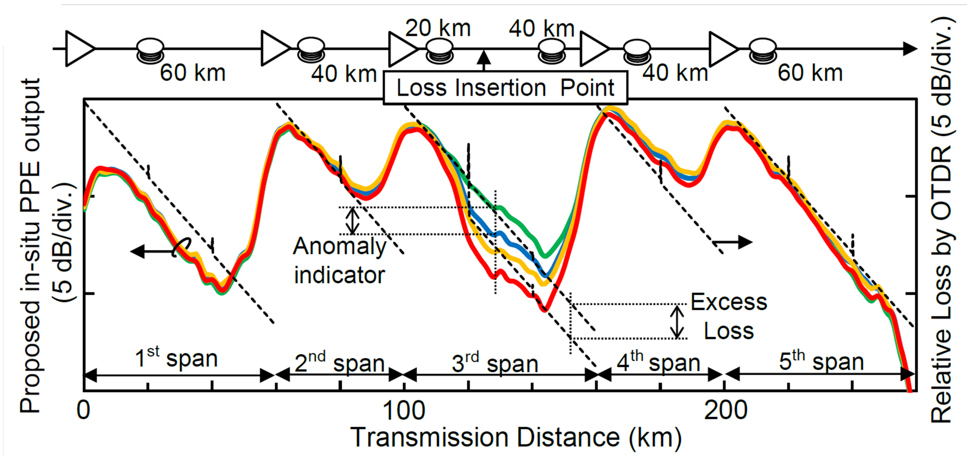

Figure 1.10: Estimated power profiles over a 260-km link from [17]. Each power profile has a different power loss inserted at 120 km.

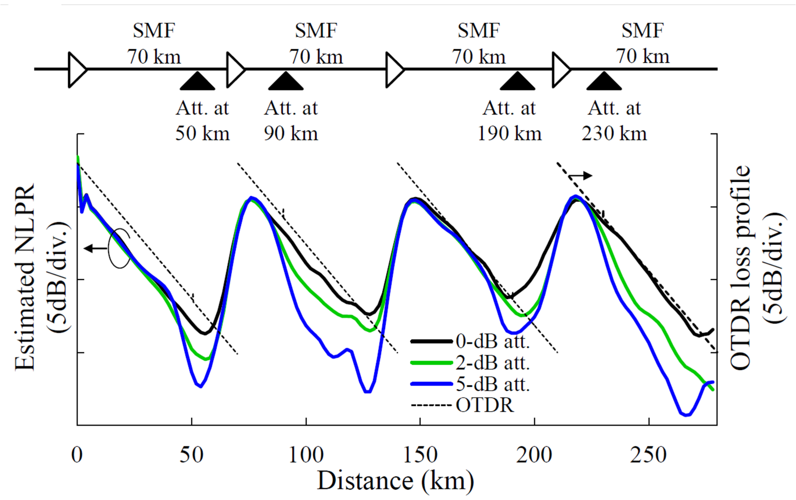

Figure 1.11: Estimated power profiles over a 280-km link from [18]. Each power profile has different power losses inserted at multiple points.

Longitudinal power profiles

A few months apart, Tanimura et. al [17] and Sasai et. al [18] proposed experimental demonstrations of longitudinal power profile estimations by using specific DSP on the received signal. In Fig. 1.10 the estimated power profiles over a 260-km optical link obtained by Tanimura et al. in [17] is shown. The OTDR profile showing the evolution of the optical power in the link is shown to compare it with estimated power profiles. We see that the curves follow the variations of the optical power in the link. The value obtained decreases during the propagation inside a span and increases around the position of the amplifiers. However, we see that the variations are much smoother than expected, specially around amplifiers. We also note that the scale is in dB/div, not in Watt or in dBm.

In Fig. 1.11, the estimated power profiles over a 280-km optical link obtained by Sasai et al. in [18] is shown. We see that the obtained power profiles are quite similar to the previous ones.

Power profile estimation algorithms

We now present the two algorithms proposed to estimate power profiles.

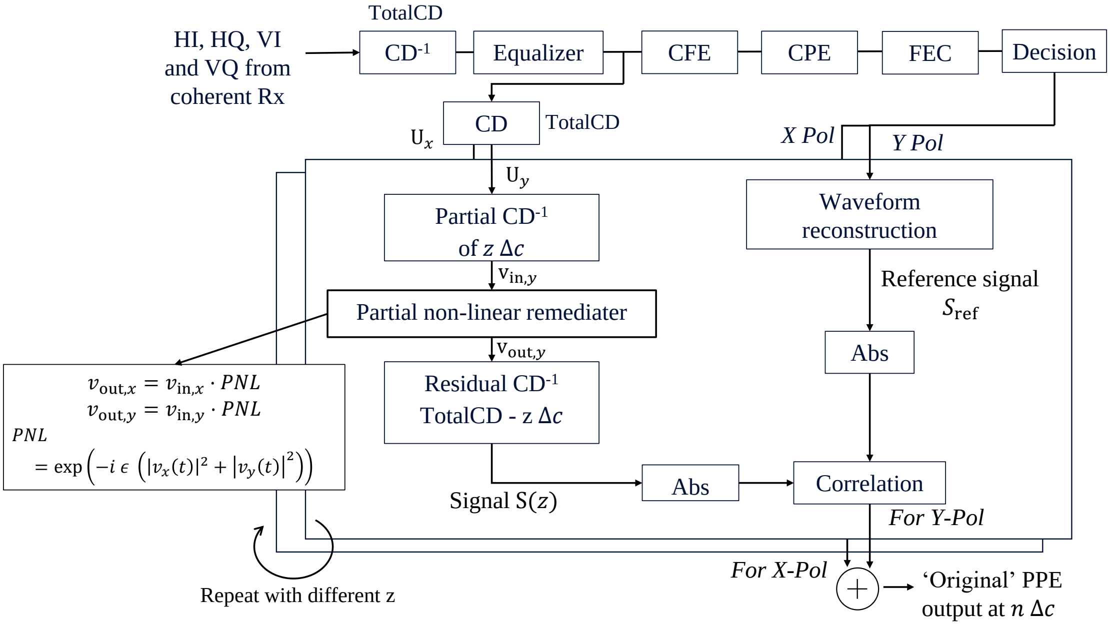

Figure 1.12: "Original correlation-based" technique. Power profile estimation algorithm first proposed in [17]. Schematic is drawn from [22].

We draw in Fig. 1.12 a schematic diagram of the algorithm proposed in [17] for the estimation of power profiles. This estimation is based on the correlation between two signals, which we denote $S(z)$ and S_{ref}. $S(z)$ is the signal which holds information about the non-linear effects at point z and S_{ref} is the reference signal. The power profile is built by varying the position z from 0 to the total length of the fiber L in the profile. Let us see how each of those signals is built. To obtain S_{ref}, the usual DSP - CD compensation, equalization and polarization demultiplexing, CFE, CPE - is performed on the four real output signals of the coherent receiver (usually denoted as HI and HQ for H or "x" polarization and VI and VQ for V or "y" polarization). Then, a FEC algorithm could be used or hard decision [22] can be performed. Finally, S_{ref} is obtained by reconstructing the transmitted waveform from the decoded bits. When the SNR is high enough, this signal is the signal which was sent into the fiber.

Both polarizations of $S(z)$, $S_x(z)$ and $S_y(z)$ are obtained in several steps. The compensation of the total CD is first performed on the signals from the coherent receiver. Equalization and demultiplexing of the polarizations are performed. Then, the total CD is applied to the signal. The obtained signal is denoted by $U_j(t)$, with $j = \{x, y\}$ corresponding to the polarization. Then, three operations are performed on $U_j(t)$, for each z. First, the CD corresponding to a distance $L-z$ is compensated, L being the length of the total transmission. This corresponds to convolve $U_j(t)$ with the impulse response $d_{L,z}$ defined in Eq. (1.6):

$$\begin{cases} v_{\mathrm{in},x}(z,t) = d_{L,z} \otimes U_x(t) \\ v_{\mathrm{in},y}(z,t) = d_{L,z} \otimes U_y(t). \end{cases} \tag{1.17}$$

Secondly, a phase rotation of ϵ times the total power is performed to partially compensate for SPM effects and we obtain $v_{\mathrm{out},j}(z,t)$:

$$\begin{cases} v_{\mathrm{out},x}(z,t) = v_{\mathrm{in},x}(z,t) \cdot \exp(-i\epsilon(|v_{\mathrm{in},x}(z,t)|^2 + |v_{\mathrm{in},y}(z,t)|^2)) \\ v_{\mathrm{out},y}(z,t) = v_{\mathrm{in},y}(z,t) \cdot \exp(-i\epsilon(|v_{\mathrm{in},x}(z,t)|^2 + |v_{\mathrm{in},y}(z,t)|^2)), \end{cases} \tag{1.18}$$

where ϵ is set to 0.01. Thirdly, the CD corresponding to the remaining distance z is compensated and we obtain $S_x(z,t)$ and $S_y(z,t)$:

$$\begin{cases} S_x(z,t) = d_{z,0} \otimes v_{\mathrm{out},x}(z,t) \\ S_y(z,t) = d_{z,0} \otimes v_{\mathrm{out},y}(z,t). \end{cases} \tag{1.19}$$

Finally, the power profile, which we denote by R, is obtained by performing the correlation between the absolute values of $S(z)$ and S_{ref} for each value of z:

$$R(z) = \mathrm{corr}(|S_x(z,t)|, |S_{x,\mathrm{ref}}(t)|) + \mathrm{corr}(|S_y(z,t)|, |S_{y,\mathrm{ref}}(t)|). \tag{1.20}$$

No detail is given about the type of correlation which is performed. We observe that each $R(z)$ can be computed independently for each z. z are discrete values and are chosen by the user depending on the zone they want to monitor or on the spatial granularity. The spatial granularity $\Delta z = L/N$ depends on the number of points N of the profile.

In the following, we will refer to this technique as the “original correlation-based” technique.

We show in Fig. 1.13 a schematic diagram of the algorithm drawn by Sasai et al. in [18] for the estimation of power profiles. The algorithm follows an approach similar to DBP techniques, but with several iterations of the DBP to learn compensating coefficients as done in a neural network.

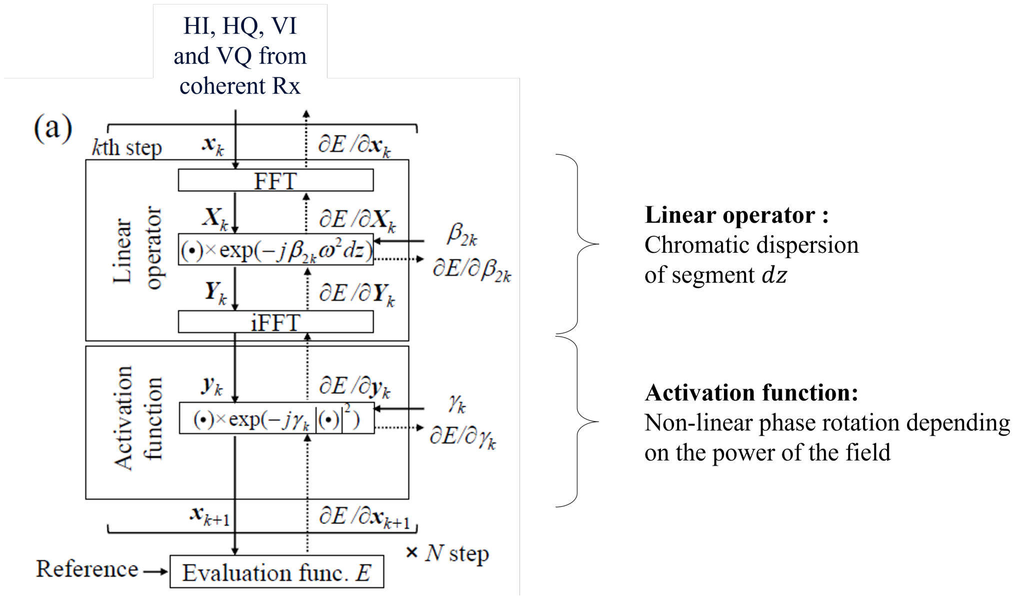

Figure 1.13: "Adaptive DBP" technique. Power profile estimation algorithm proposed by Sasai. Schematic (left side) is taken from in [18].

The received signals from the coherent receiver are first propagated through standard DBP. The non-linear coefficients γ_k with $k = 1, 2, ...N$ are set to arbitrary initial values. k indicates the index of the SSFM segment. The dispersion coefficients $\beta_{2,k}$ are set to averaged values of estimated dispersion coefficient (total dispersion divided by the total number of steps N). A mean squares error is calculated for the evaluation function using the back-propagated signal and the reference signal. The reference signal is obtained similarly to what was proposed in the correlation based-method explained earlier. Gradient descent method is then used to update coefficients γ_k and $\beta_{2,k}$. After several iterations, the coefficients are optimized and the vector containing all γ_k corresponds to the estimated power profile. Sasai et al. also refer to this estimated profile as "NLPR" for "non-linear phase rotation" as it corresponds to the required phase rotation at each distance to equalize the signal and target the minimal error with respect to the transmitted signal. The authors claim that they are estimating the true power in the link, providing that the non-linear coefficient γ is known.

In the following, we will refer to this technique as the "adaptive DBP" technique.

To conclude, we presented the first two algorithms proposed to estimate power profiles in [17, 22] and in [18]. In the first one, we see similarities between the RP method and the proposed algorithm as the three operations performed for each z

correspond to one branch of the RP method, with 2 linear operations and 1 non-linear phase rotation applied at a point z. The second algorithm is based on the SSFM since for each iteration of the gradient descent method, N linear operators and N non-linear operators are applied to the received signal corresponding to the CD and SPM.

Anomaly detection schemes

Finally, we present the anomaly detection scheme that they propose using the longitudinal power profiles. This scheme is first proposed by the authors of [17, 22]. The same scheme is used by the authors in [18] with the adaptive DBP power profile estimation technique. We plot in Fig. 1.14 a schematic diagram of the proposed anomaly detection scheme. When the power profile is computed, we switch between two modes. During the “normal state” mode, the power profile is stored in a memory and corresponds to the reference power profile. During the “monitoring” mode, the **anomaly indicator** is computed as the difference between the reference power profile and the monitoring power profile.

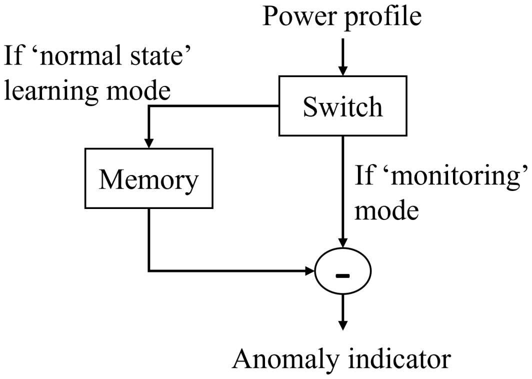

Figure 1.14: Schematic diagram of proposed anomaly detection scheme common to [17, 22] and [18].

In Fig. 1.15a, we plot the anomaly indicators obtained in [17] with the correlation-based power profile estimation technique. In Fig. 1.15b, we plot the anomaly indicators obtained in [18] with the adaptive DBP power profile estimation technique. Both figures show anomaly indicators in presence of power losses of different values. In both figures, we see peaks located around the positions of inserted losses confirming the mismatch between the reference and the monitoring state in terms of powers and validating the use of power profile estimation techniques for anomaly detection.

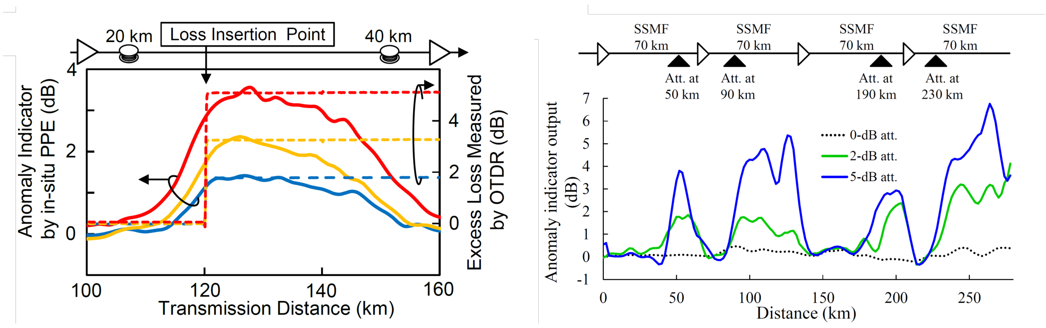

(a) Anomaly indicators in presence of 3 inserted power losses at 120 km. Experimental results from [17].

(b) Anomaly indicators in presence of 2 and 5-dB power losses inserted at 20, 90, 190 and 230 km. Experimental results from [18].

Figure 1.15: Anomaly indicators in presence of multiple power losses.

Regarding the full characterization - position and value - of power losses, in Fig. 1.15a, we see that when the loss value is increased, the peak amplitudes increases. However, the two presented scales are different and no indications on how to retrieve the value of the power loss from the peak is given. In Fig. 1.15b, we also observe that when the loss value is increased from 2 to 5 dB, the amplitude of the peaks increase. Compared to the Fig. 1.15a, a single dB-scale is proposed. For the loss inserted at 50 km, we obtain roughly 1.8 dB and 4 dB, which is satisfactory. However, for other losses, the measurement seems more difficult to perform. The peaks are either too large, or not of the right amplitude. Finally, in the follow-up article [22] of the authors in [17], they propose to use the derivative of the anomaly indicator to locate power losses and investigate through simulations the accuracy of the estimation. In Fig. 1.16, we plot the derivative of the anomaly indicator in presence of 3 power losses of different values at 120 km, obtained experimentally. We observe that the peak in the derivative curve is located around the position of the loss, a few kilometers away, as said in [22]. They also investigate numerically the location accuracy and were able to locate an anomaly 500 meters aways from its real location, by decreasing the spatial granularity Δz and increasing the baud rate. We note that in this follow-up article, all anomaly indicators are plotted using arbitrary units for the y-axis, which indicates no claim and no methodology on the possibility to estimate power loss values from anomaly indicators.

1.4.3 Power profile estimation techniques

Following these first proposed techniques, several works focused on improving them and others proposed new techniques. We gather in Table .1.1 the relevant works

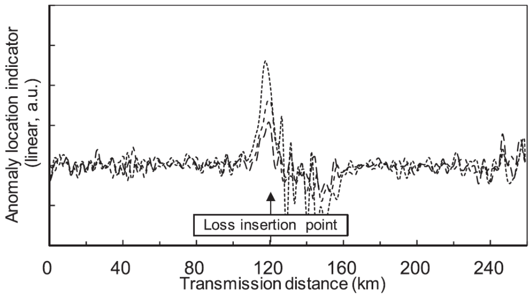

Figure 1.16: Derivative of the anomaly indicator in presence of 3 power losses of different values at 120 km. Experimental results from [22].

with the corresponding used technique.

Techniques (year of first proposition)	References
Original correlation-based (2019)	[17, 21, 22, 51–54]
Adaptive DBP (2020)	[18, 19, 55, 56]
Volterra (2021)	[20]
Forward correlation-based (2022)	[57]
Linear least squares (2022)	[58]
Comparative work on correlation-based technique and minimum mean square error (MMSE) (2022)	[59]

Table 1.1: Summary of power profile estimation techniques from 2019 to 2023. In "References" are cited works which propose the technique and those who use it.

In [20], the authors propose the use of an algorithm based on a Volterra nonlinear equalizer. Through simulations, a power profile - shown in relative dB scale - is estimated. The variations are quite sharp and follow those of the real power. This can be explained by the use of a high baud rate - 130 Gbaud -, which, as highlighted in [22], increases the spatial resolution. They also use their technique for anomaly detection and estimation of power losses.

In [19], the authors propose an improvement of their "adaptive DBP" technique and show experimentally a power profile estimation on a 2000-km link using a circulative loop. They propose to optimize the step of the DBP by varying it according to the power at each point. This optimization reminds us of the varying step size which is usully performed in SSFM.

In [57], the authors propose an adaptation of the "original correlation-based" technique to experimentally locate multi-path interference. The correlation is performed between the received signal and one branch of the RP method which is applied to the reference signal. Equations of the adapted algorithm will be derived at the end of this section and this technique will be refered to as the "forward correlation-based" technique.

In [58], the authors of [18] propose a linear least-squares method to estimate power profiles. The goal is to minimize the difference between the received signal and an emulated received signal. This emulation is done by using the RP1 method. Through numerical simulations, this method offers an excellent agreement between the estimated power profile and the theoretical power.

Finally, a theoretical work is proposed in [59] by Sasai et al. to compare correlation-based - "original" and "forward" - and minimum mean square error (MMSE) techniques. By MMSE techniques they refer to the "adaptive DBP" with the gradient optimization of the SSFM and its equivalent linear least squares [58]. They explain the reasons behind the deteriorated spatial resolution of the correlation-based techniques. In particular, they show that these techniques filter high frequencies of the power profile resulting in a smoothened estimate of it.

We now describe the adaptation of the "original correlation-based" techique proposed in [57] and formalized in [59]. We draw in Fig. 1.17 a schematic diagram of the algorithm. Notations from Fig. 1.12 were kept to ease the comparison between both correlation techniques. Two differences exist between the "original correlation-based" and the new correlation-based algorithms. The main difference between both techniques is that, in the latter case a branch of the RP method is applied to the reference signal whereas in Fig. 1.12, for the "original correlation-based" technique, inverse operations of the branch are applied to the received signal. Therefore, this adaptation of the "original correlation-based" techique is referred to as "forward correlation-based".

The correlation is performed between a reference signal denoted by $S'_{\mathrm{ref}}(z,t)$ and the signal $U(t)$. The signal $U(t)$ is similar to the one in Fig. 1.12 except that the CFE and the CPE are applied. This operation needs to be performed since the correlation will be done between the signals and not the absolute values of them, which is the second difference with respect to the "original correlation-based" technique. $S'_{\mathrm{ref}}(z,t)$ is obtained by applying three operations on $S_{\mathrm{ref}}(t)$. First, the CD corresponding to a distance z is applied. This corresponds to convolve $S_j(t)$ where $j = x, y$ with the impulse response $d_{0,z}$ defined in Eq. (1.6):

$$\begin{cases} s_{\mathrm{in},x}(z,t) = d_{0,z} \otimes S_{x,\mathrm{ref}}(t) \\ s_{\mathrm{in},y}(z,t) = d_{0,z} \otimes S_{y,\mathrm{ref}}(t). \end{cases} \tag{1.21}$$

Secondly, a phase rotation of ϵ times the total power is performed to partially emulate SPM effects and we obtain $s_{\mathrm{out},j}(z,t)$:

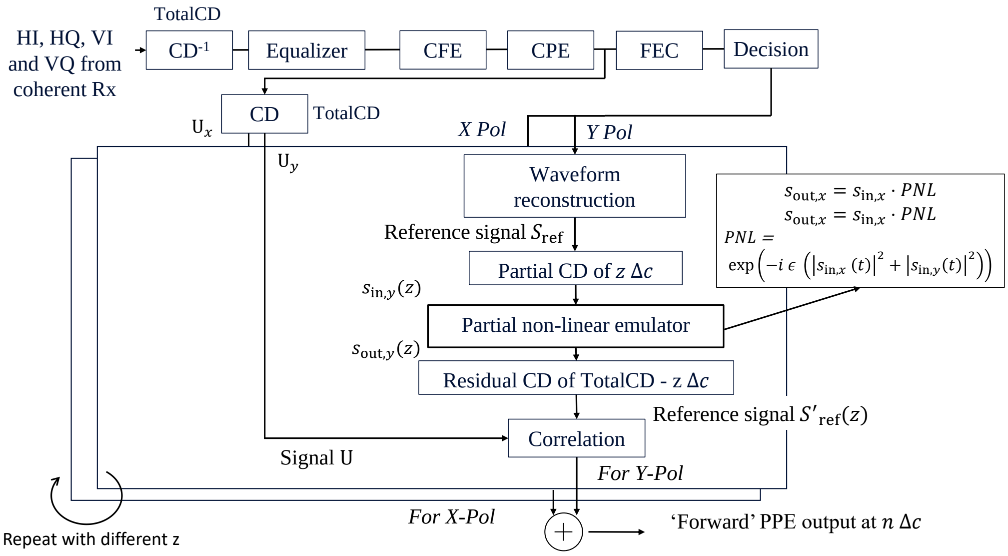

Figure 1.17: "Forward correlation-based" technique. Power profile estimation algorithm. Schematic inspired by technique proposed by Hahn et al. in [57] and formalized by Sasai et al. in [59].

$$\begin{cases} s_{\text{out},x}(z,t) = s_{\text{in},x}(z,t) \cdot \exp(-i\epsilon(|s_{\text{in},x}(z,t)|^2 + |s_{\text{in},y}(z,t)|^2)) \\ s_{\text{out},y}(z,t) = s_{\text{in},y}(z,t) \cdot \exp(-i\epsilon(|s_{\text{in},x}(z,t)|^2 + |s_{\text{in},y}(z,t)|^2)). \end{cases} \tag{1.22}$$

ϵ is set to 0.01. Thirdly, the CD corresponding to the remaining distance $L - z$ is applied and we obtain $S'_{x,\text{ref}}(z,t)$ and $S'_{y,\text{ref}}(z,t)$:

$$\begin{cases} S'_{x,\text{ref}}(z,t) = d_{z,L} \otimes s_{\text{out},x}(z,t) \\ S'_{y,\text{ref}}(z,t) = d_{z,L} \otimes s_{\text{out},y}(z,t). \end{cases} \tag{1.23}$$

Finally, the power profile R is obtained by performing the correlation between $U(t)$ and $S'_{\text{ref}}(z,t)$ for each value of z:

$$R(z) = \text{corr}(U_y(t), S'_{x,\text{ref}}(z,t)) + \text{corr}(U_y(t), S'_{y,\text{ref}}(z,t)). \tag{1.24}$$

The correlation is performed on the complex signals and the power profile is a complex z-vector. Therefore, it is necessary to take the absolute value or the real value of the estimated profile. We note that the authors of [57] propose to linearize the exponential in Eq. (1.22) as $\exp(1 - i\epsilon|\cdot|^2) \approx 1 - i\epsilon|\cdot|^2$. Then, they only consider the non-linear part $i\epsilon|\cdot|^2$ for the last operation and final correlation.

1.4.4 Applications

Applications	Techniques	References
Identification and location of power losses	Correlation-based	[17, 22]
Identification of power losses and identification of fiber types	Adaptive DBP	[18]
Estimation of passband narrowing	Adaptive DBP	[55]
Raman-amplified power profile and Raman gain spectra estimation	Adaptive DBP	[56]
Location of PDL	Correlation-based	[60]
Location of reflection-induced multi-path interference	Correlation-based	[57]
Power profile estimation in C + L-band and amplifier gain profile estimation	Correlation-based	[53, 54]

Table 1.2: Summary of applications using power profile estimation techniques.

We gather in Table 1.2 some of the applications which were proposed using power profile estimation techniques. We show in Fig. 1.18 some of the results of [53] where they apply the "original correlation-based" technique to estimate power profiles from several WDM channels in C+L-band. From this, they were able to estimate the amplifier gain profile and tilt values.

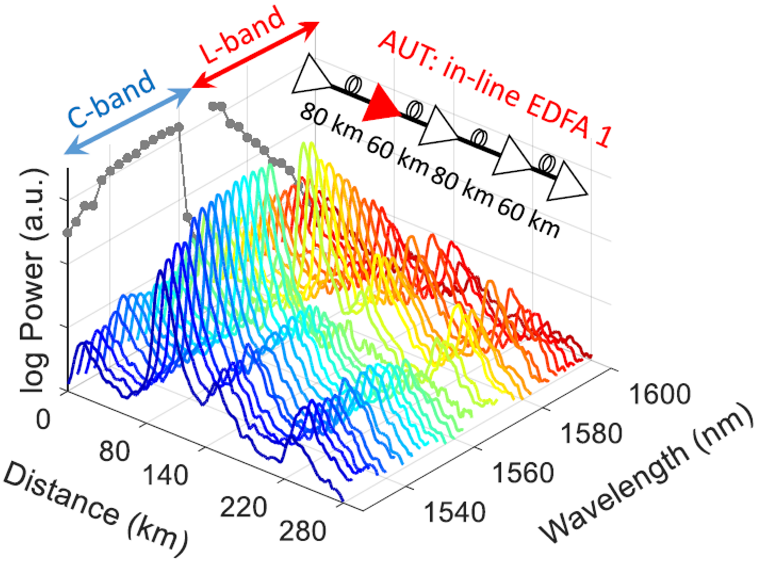

Figure 1.18: Estimated power profiles on channels with wavelengths on C+L-band from [53].

1.5 Conclusion

In this chapter, we reviewed the basics of optical communications, useful for the next chapters. We then highlighted the concept of monitoring. We explained the main goal of monitoring and we showed how it became even more useful with automated optical networks. Indeed, when automating a system, a constant monitoring is necessary to determine possible optimizations or detect potential anomalies. We then saw how DSP on received signals at the coherent receiver has opened the path for massive monitoring.

Recently, some techniques were proposed to estimate longitudinal power profiles by applying a specific DSP on received signals. Those techniques are based on the compensation of non-linear effects and do not require any additional hardware which decreases the cost of implementation. They also share the advantage that the estimation can be performed on a channel which carries data and that the technique can go trough amplifiers. We presented both pioneer techniques, proposed by Tanimura et al. in [17] and by Sasai et al. in [18]. We presented the anomaly detection scheme that they propose when they analyze what they call, an anomaly indicator which is the difference between a reference power profile and a monitoring one. They both identify power losses in multi-span links. Tanimura et al. also validates in [22] the location of the power losses with the technique, within a few kilometers, which is important for trouble shooting. However, none of the two works

[17, 18] focus on the estimation of those power losses. To get closer to the root-cause of the anomaly and to make smart decisions, a total characterization of anomalies is desirable. That it why, in Chapter 2, we propose a calibration-based method to fully characterize - both estimate and locate - power losses by introducing a simple model describing the behavior of the power profile computed by correlation-based power profile techniques.

Chapter 2

Calibration-based method to characterize power losses

2.1 Introduction

Power profile estimation techniques [17, 18, 22] are promising solutions for the monitoring of optical networks. As they are based on a digital signal processing (DSP) at the receiver side, they do not require additional hardware making them low cost monitoring techniques. Plus, the power is an important parameter to monitor for optimization and margin reduction [11]. Tanimura et al. propose the “original correlation-based” power profile estimation technique in [17] while Sasai et al. propose an “adaptive digital back propagation (DBP)” power profile estimation technique in [18]. The authors of both works propose to use this monitoring technique to detect power losses by comparing a current power profile to a stored reference power profile. In order for networks to make smart decisions - repairing, rerouting [41] or adapting transmitter parameters [13] - , it is important to perform the full characterization - position and value - of power losses. While in [17, 22], Tanimura et al. focused on the location of power losses, in [18], no study is performed on the accuracy of the power estimation.

This chapter is organized as follows. In Section 2.2, we describe the method that we propose to estimate power losses using power profiles computed with a correlation-based technique. The proposed method is based on a calibration and a model describing the behavior of the technique. In Section 2.3, we demonstrate the validity of this method through experiments and we assess the estimation accuracy.

2.2 The proposed method

In this section, we present our method to characterize - locate and estimate - power losses. We first present simulation parameters which we choose for the description of the method. Then, we propose a model to describe the behavior of the power profile computed with a correlation-based technique [17]. Based on this mathematical model, we finally describe how we propose to extract information about power losses from the longitudinal power profiles.

2.2.1 Description of the numerical set-up

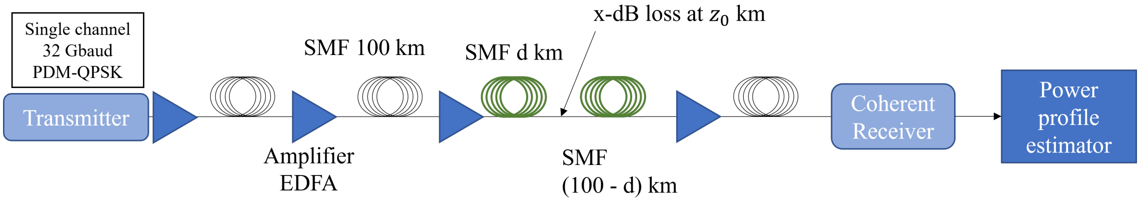

Figure 2.1: Numerical simulation set-up. A x-dB power loss is inserted at z_0 km, d km from the previous amplifier in span $k = 3$. SMF: single mode fiber. EDFA: erbium-doped fiber amplifier.

Simulation set-up

We choose a single channel transmission as the power profile estimation technique is based on self-phase modulation (SPM) effects. The symbol rate is set to 32 Gbaud. The transmitter sends random sequences modulated with 1024 polarization-division multiplexing (PDM)-quadrature phase shift keying (QPSK) symbols which are pulse-shaped with a root-raised cosine with $\rho = 0.01$ roll-off factor. We send $N_\mathrm{r} = 400$ sequences and the number of samples per symbol is set to $N_\mathrm{t} = 8$. A digital chromatic dispersion (CD) of 3000 ps/nm is applied to the transmitted signal. The wavelength of the signal is centered at $\lambda_0 = 1550$ nm. The launch power is set to 5 dBm to work in the non-linear regime.

The transmission line is composed of four 100-km spans of single mode fiber (SMF), each composed of an amplifier followed by a chunk of fiber. The fiber attenuation is set to $\alpha_\mathrm{dB} = 0.2$ dB/km. The dispersion parameter is $D = 17$ ps/nm/km, the non-linear index is $n_2 = 2.5 \cdot 10^{-20}$ m^2/W and the effective area is $A_{\text{eff}} = 80\ \mu\text{m}^2$. Amplifiers are set in a constant power mode, each targeting 5 dBm of total power (including noise) at the beginning of each span. The noise figure of the erbium-doped fiber amplifier (EDFA)s is set to 5 dB. Concerning physical effects, we model the propagation using the split-step Fourier method (SSFM) and we consider fiber attenuation, CD and non-linear effects (SPM since it is single channel). Finally, we insert power losses in a given span k, z_0 km from the beginning of the line, d km from the previous amplifier and of value x dB. All parameters - k, z_0 (or d equivalently) and x - can be varied and are the ones that we want to estimate accurately.

The optical field is received by the coherent receiver and the power profile estimation is performed.

Power profile parameters

To estimate power profiles, we use here the "original correlation-based" technique presented in Section 1.4.2 and whose algorithm is presented on a schematic diagram in Fig. 1.12. To obtain the power profile $R(z)$, we choose the Pearson coefficient ρ to measure the correlation between $S(z,t)$ and $S_{\text{ref}}(t)$:

$$R(z) = \rho(S(z,t), S_{\text{ref}}(t)) = \frac{\text{cov}(S(z,t), S_{\text{ref}}(t))}{\sigma(S(z,t)) \cdot \sigma(S_{\text{ref}}(t))}, \tag{2.1}$$

where cov· is the covariance and $\sigma\cdot$ is the standard deviation. In the rest of the manuscript, if not specified, the Pearson coefficient is used for the correlation. For the reference signal $S_{\text{ref}}(t)$, instead of performing the reconstruction after decision, in our simulations, we use the transmitted field. However, in our experiments discussed in Section 2.3, we use the reconstructed signal after decision, which is close to the ideally transmitted signal if there are not many errors. The non-linear phase remediator parameter ϵ is set to 0.01. The spatial granularity is set to $\Delta z = 1$ km.

2.2.2 Proposed model and metrics description

We now present the proposed model as well as the metrics that we will use. The general idea is to characterize power losses using the differences between a current state of the longitudinal power and a stored reference state.

We compute and store a reference power profile denoted by $R_{\text{ref}}(z)$ corresponding to a reference state. Then, during a second phase, we periodically monitor the power profile denoted by $R_{\text{mon}}(z)$. As an example, one raw reference profile and one raw

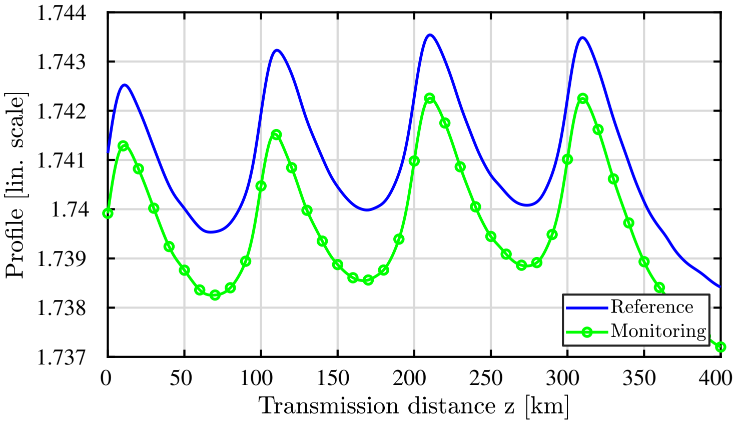

Figure 2.2: Reference and monitoring power profiles. In monitoring state, a 1-dB loss is inserted at $z_0 = 110$ km (in second span). Markers are drawn only every 10 data points.

monitoring profile are plotted in Fig. 2.2. Note that, in the following, markers in power profile curves are not drawn for every data point, to increase readibility. Here, it is plotted every 10 data points, i.e., every 10 kms since $\Delta z = 1$ km. The reference power profile only includes fiber attenuation whereas the monitoring power profile includes an aditionnal 1-dB power loss at $z_0 = 110$ km. We refer to these profiles as raw to highlight that no scaling factor was applied and that the offsets are not removed. The offsets [1] are different for both profiles since the amount of accumulated distortions is different for each state. We also see that there are four peaks corresponding to the high powers at the beginning of each span, followed by a decreasing $R(z)$ which corresponds to the power attenuated by the fiber. We can see that the variations of $R(z)$ are smoother than the true optical power $P(z)$ in the fiber. Indeed, when the power is supposed to be increased in the span of few meters in an amplifier, in the profile, it takes a few tens of kilometers. On top of that, whereas the power at the beginning of each span is 5 dBm for all four spans, we notice that all peaks have different values, due to an apparent bell-shaped enveloppe of the profile. This effect is decreased by the use of digital predispersion as proposed in [22].

Our goal here is to propose a method to estimate accurately power losses despite the obvious inaccuries that we have observed in the profile.

At the present form, $R(z)$ is a normalized correlation (see Eq. (2.1)) and there-

---

[1] The average value of both profiles is around 1.74. With the definition of $R(z)$ in Eq. (2.1), the highest possible value of $R(z)$ is 2, when the Pearson coefficient for each polarization is equal to 1. This case is not interesting as it corresponds to the case where the reference signal is perfectly correlated with $S(z)$, meaning that there is no non-linear effects (and no other noise) and no variations with z meaning no profile.

fore, to evaluate power losses, we propose to link $R(z)$ to the true power. Despite the smoother variations and the differences in peaks heights, we suggest an affine relationship between $R_i(z)$ and the optical power in the link $P_i(z)$ as follows:

$$R_i(z) = C \cdot P_i(z) + \theta_i, \tag{2.2}$$

where $i \in \{\text{ref}, \text{mon}\}$, $C > 0$ is a proportionality factor and θ_i is an offset factor. We assume that C is independent of the state of the link, i.e., reference or monitoring, for a given link and given transmission parameters. The offset θ_i depends on the overall distortions. Since some noise contributions and distortions (amplified spontaneous emission (ASE), SPM and cross-phase modulation (XPM) effects) depend on the state (reference or monitoring), so does θ_i. This can be seen on Fig. 2.2 where both profiles are not aligned.

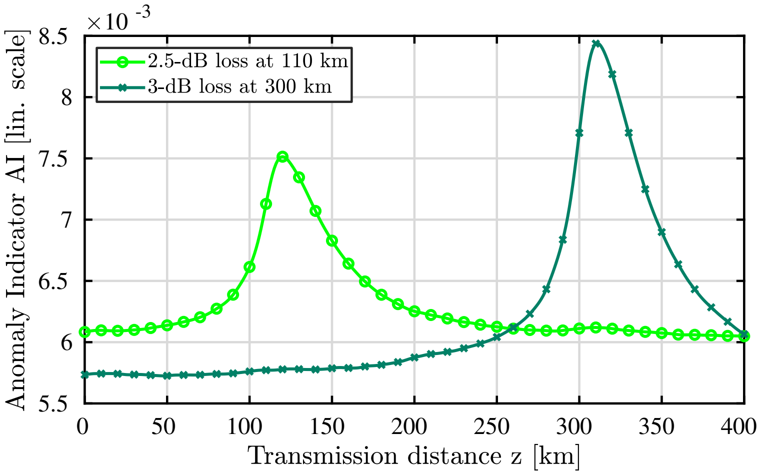

Figure 2.3: Raw anomaly indicators in two distinct cases: a 2.5-dB loss at 110 km and a 3-dB loss at 300 km. The maximum slopes of each peak correspond to the loss positions.

To monitor possible changes between the reference state and the monitoring state, we compute the so-called anomaly indicator (AI) defined as :

$$AI(z) = R_{\text{ref}}(z) - R_{\text{mon}}(z). \tag{2.3}$$

When a loss occurs, the AI function is different from a constant value since the current state is no longer the same as the reference state. We plot in Fig. 2.3 two raw AIs for two different loss values and positions: a 2.5-dB loss at 110 km and a 3-dB loss at 300 km. It is the direct difference between the raw profiles. In both curves, we see a peak which is an indicator of a mismatch in power between the two states. We can observe that each peak is located near the real loss position. As shown in [22], the position of each loss is given by the maximum slope of the peaks.

We can now use our proposed approximation for $R(z)$ presented in Eq. (2.2) to write $AI(z)$ as defined in Eq. (2.3):

$$AI(z) = C \cdot (P_{\text{ref}}(z) - P_{\text{mon}}(z)) + \Delta\theta, \tag{2.4}$$

with $\Delta\theta = \theta_{\text{ref}} - \theta_{\text{mon}}$. Let $z^{(k)}$ be the beginning of the span k in which the power loss occurs. If this loss is located at z_0, the power $P_{\text{mon}}(z)$ at a given point $z > z_0$ and up to $z^{(k+1)}$, is multiplied by a transmission factor $T_0 < 1$. Since in telecom optics the dB scale is commonly used, the loss value l_{dB} due to a power loss is thus expressed in dB. It is linked to the transmission factor T_0 through $l_{\text{dB}} = -10 \cdot \log_{10}(T_0)$. We gathered our notations in Table 2.1. Same notations will be used in following chapters.

Transmission factor	T_0
Loss factor	$1 - T_0$
Loss value [dB]	l_{dB}
Loss position [km]	z_0
Beginning position of span k [km]	$z^{(k)}$

Table 2.1: Notations used for proposed model.

At $z^{(k+1)}$, since the EDFA work in a constant power mode, the power $P_{\text{mon}}(z)$ is set to its initial value at the beginning of the transmission $z = 0$. Hence, we can express $P_{\text{mon}}(z)$ as:

$$P_{\text{mon}}(z) = \begin{cases} P_{\text{ref}}(z), & 0 \leq z < z_0 \\ T_0 \cdot P_{\text{ref}}(z), & z_0 \leq z < z^{(k+1)} \\ P_{\text{ref}}(z), & z^{(k+1)} \leq z < L. \end{cases} \tag{2.5}$$

Combining Eq. (2.5) and Eq. (2.4) implies that:

$$AI(z) = \begin{cases} \Delta\theta, & 0 \leq z < z_0 \\ C \cdot (1 - T_0) \cdot P_{\text{ref}}(z) + \Delta\theta, & z_0 \leq z < z^{(k+1)} \\ \Delta\theta, & z^{(k+1)} \leq z < L. \end{cases} \tag{2.6}$$

To precise the expression of $AI(z)$, we propose to rely on the following attenuation model for the power in the k^{th} span:

$$P_{\text{ref}}(z) = P_{\text{ref}}(z^{(k)}) \cdot 10^{-\frac{\alpha_{\text{dB}}}{10} \cdot (z - z^{(k)})}, \tag{2.7}$$

where α_{dB} is the fiber attenuation constant in dB/km. We can finally write the final expression of the $AI(z)$ as a function of the proportionality factor C, the power at the beginning of the span $P_{\text{ref}}(z^{(k)})$, the loss factor $(1-T_0)$ and the loss position z_0:

$$AI(z) = \begin{cases} \Delta\theta, & 0 \leq z < z_0 \\ C \cdot P_{\text{ref}}(z^{(k)}) \cdot (1-T_0) \cdot 10^{-\frac{\alpha_{\text{dB}}}{10}\cdot(z-z^{(k)})} + \Delta\theta, & z_0 \leq z < z^{(k+1)} \\ \Delta\theta, & z^{(k+1)} \leq z < L. \end{cases} \tag{2.8}$$

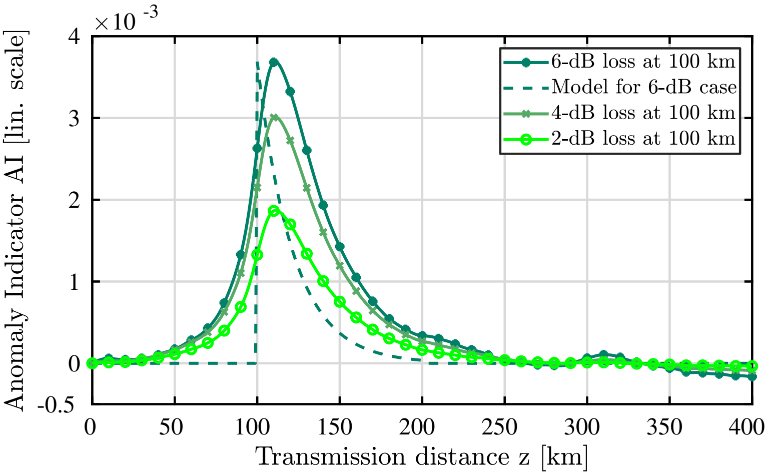

Figure 2.4: Anomaly indicators (aligned) in presence of losses located at the beginning of span 2 *i.e.*, at 100 km for 3 loss values and model from Eq. (2.8) for the 6-dB loss.

To understand the final expression of the AI, we plot in Fig. 2.4 three AIs for three loss values: 2 dB, 4 dB and 6 dB. All losses are located at 100 km, which is at the beginning of the second span. We choose to remove $\Delta\theta$ so that all AI are aligned. One can approximate $\Delta\theta$ to the value of $AI(z)$ far away from the peak. We also plot the model for $AI(z)$ for the 6-dB case, which corresponds to Eq. (2.8) with $z_0 = z^{(k)}$ - meaning that the loss is located at the position of the amplifier - and with $l_{\text{dB}} = 6$ dB or $T_0 \approx 0.25$. We see that the shape of the AI follows that of the model, with smoother variations. In particular, the position of the maximum value of the model is located at the position of the loss whereas this position corresponds to the maximum slope of the AI from simulations. We also see that, as the loss value l_{dB} is increasing, the peak amplitude increases, which is linked to the increase of $(1-T_0)$ in Eq. (2.8).

To understand the dependency with the loss position, we plot in Fig. 2.5, three AIs, with the same loss value $l_{\text{dB}} = 3$ dB but with different positions, 100 km, 110 km and 120 km. We can see that the peak amplitudes are decreasing when the loss is

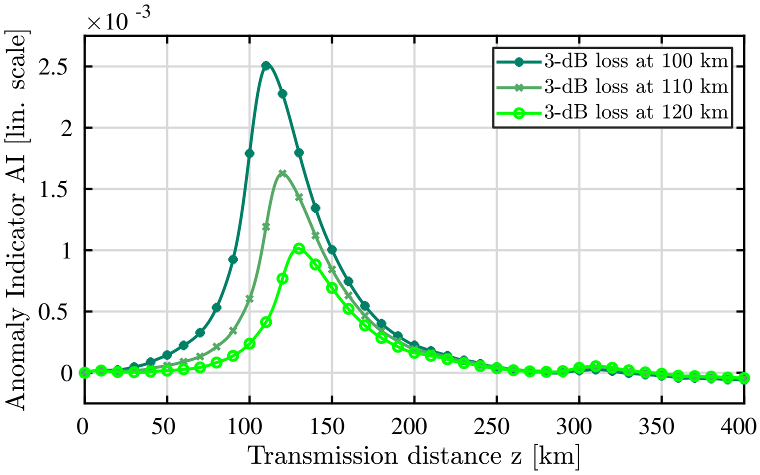

Figure 2.5: Anomaly indicators (aligned) in presence of three 3-dB losses located at 100 km, 110 km and 120 km.

located further away from the amplifier. This is phenomenologically accounted for by the exponential term appearing in the proposed Eq. (2.8) which accounts more precisely for the decreasing power in the link due to fiber attenuation.

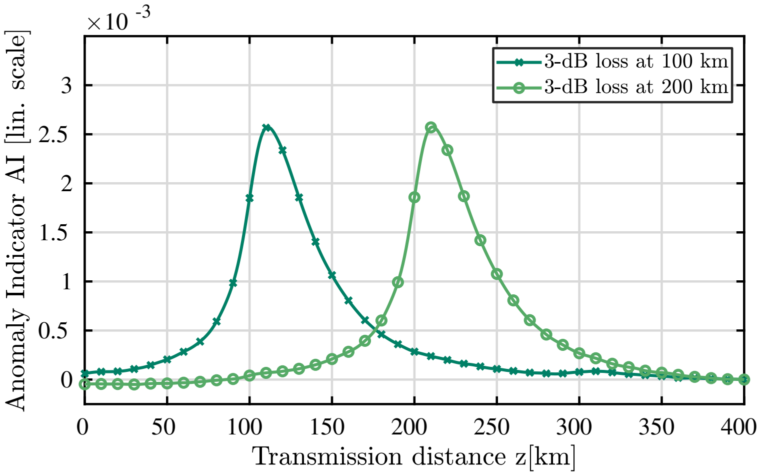

Figure 2.6: Anomaly indicators (aligned) in presence of two 3-dB losses at the beginning of 2nd and 3rd, *i.e.,* 100 km and 200 km, respectively. Input power of 2nd and 3rd span are both equal to 5 dBm.

Finally, to generalize the expression in Eq. (2.8), we plot in Fig. 2.6, the AIs for two 3-dB losses inserted at two positions: beginning of spans $k = 2$ and $k = 3$. The span input power is identical for all spans, so $P_{\text{ref}}(z^{(2)}) = P_{\text{ref}}(z^{(3)}) = 5$ dBm. In this case, we obtain identical AI shifted by 100 km. This is due to the fact that the span input powers are identical as well as the loss values. If the span input power differed from one span to another, for a given loss factor T_0, the obtained AI peaks would have a different amplitude.

We now focus our analysis directly on the peak amplitude A_{peak} induced by a loss located at z_0 and of loss factor $(1-T_0)$. We can write A_{peak} as:

$$\begin{aligned} A_{\text{peak}}(z_0, T_0) &= \max_{0<z<L}(AI(z)) - \Delta\theta \\ &= C \cdot (1-T_0) \cdot P_{\text{ref}}(z_0). \end{aligned} \tag{2.9}$$

Injecting Eq. (2.7) into Eq. (2.9), we finally obtain the expression of A_{peak}:

$$A_{\text{peak}}(z_0, T_0) = C \cdot (1-T_0) \cdot P_{\text{ref}}(z^{(k)}) \cdot 10^{-\frac{\alpha_{\text{dB}}}{10}\cdot(z_0 - z^{(k)})}. \tag{2.10}$$

From Eq. (2.10), we can see that A_{peak} is directly proportional to the proportionality factor C, the loss factor $(1-T_0)$, the power at the beginning of the k^{th} span $P_{\text{ref}}(z^{(k)})$ and an attenuation term linked to the fiber attenuation and the loss position z_0.

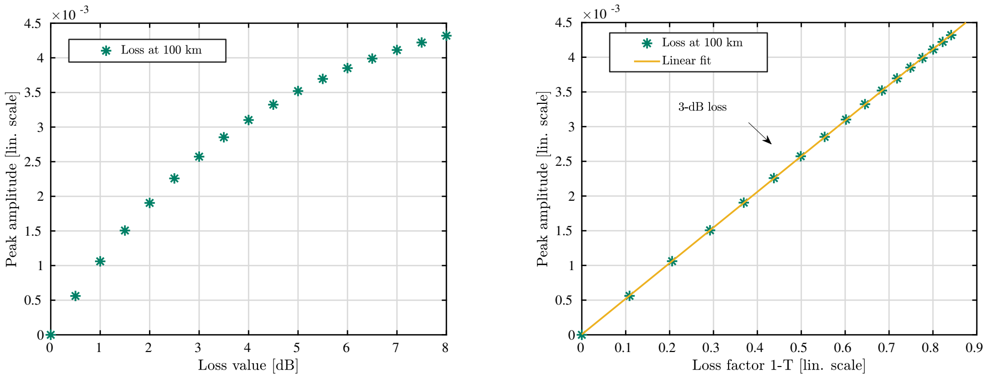

(a) Measured peak amplitudes as a function of loss values l_{dB}.

(b) Measured peak amplitudes as a function of loss factors $(1-T_0)$.

Figure 2.7: Measured peak amplitudes.

As a final numerical validation of the proposed model, we vary the loss value from 0 to 8 dB and loss position from 100 to 165 km. The latter corresponds to varying the loss distance from the amplifier position $z = z^{(2)} = 100$ km, from $d = 0$ to $d = 65$ km on our simulation set-up. For each loss value and position, we compute an AI and we measure the amplitude of the resulting peak $\widehat{A_p}$ as in Eq. (2.9). In pratice $\Delta\theta$ can be measured from the AI at $z = 0$, or $z = L$, ideally far away from the peak.

In Fig. 2.7, we plot the measured peak amplitude as a function of the loss value l_{dB} in Fig. 2.7a and of the loss factor $(1-T_0)$ in Fig. 2.7b. We can see on the latter that the measured peak amplitude is proportional to $(1-T_0)$, as predicted by the model.

In Fig. 2.8a, we plot, as a function of the loss distance d with respect to the previous amplifier, the measured peak amplitudes in linear scale with several loss values. We observe that the peaks are decreasing rapidly with the loss distances. In Fig. 2.8b, we plot the measured peak amplitudes in dB scale as well as a linear fit for the 1-dB case. The latter confirms a logarithm dependency of the peak amplitude with the loss distance, which was predicted by the model. On top of that, we can see that when the loss distance from the amplifier is varied from 0 to 50 km, the peak amplitude is decreased by -10 dB, corresponding to the 0.2 dB/km fiber attenuation, suggesting that the peak amplitude is directly proportional to the real power at the input of the power loss.

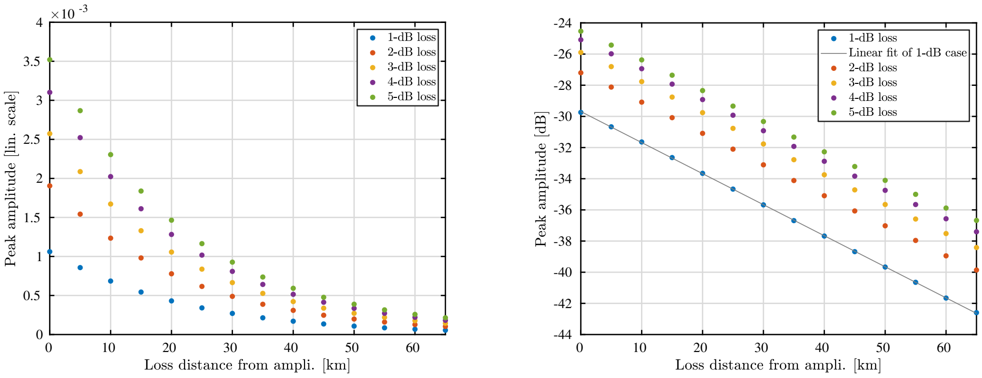

(a) Peak amplitudes expressed in linear scale.

(b) Peak amplitudes expressed in dB scale.

Figure 2.8: Measured peak amplitudes with respect to the loss distance d from the amplifier position $z^{(2)} = 100$ km.

In conclusion, we have proposed a model to describe the behavior of the power profile, which led to a description of the AI. We proposed to focus on the peak amplitude of the AI and wrote an expression of it. For each step, we showed how numerical simulations validate the model. Finally, we saw that the peak amplitude is a good candidate to characterize power losses because of the information it holds.

2.2.3 Principle of the calibration-based method

Now that the variations of the peak amplitude with the loss value and loss position are understood, we can go through the details of the proposed calibration-based method. The method is based on a calibration step and allows for the full characterization - value and position - of a power loss during the monitoring phase by an analysis of the peak of the AI.

Calibration step

This step has two main objectives : estimate the proposed calibration factor $C_p(k) = C \cdot P_{\text{ref}}(z^{(k)})$ and determine the position $z^{(k)}$ of the amplifier which is at the beginning of the span k we want to monitor. During this step, a **reference power profile** needs to be computed and stored. However, it can be recomputed and restored at a later moment to define a new reference state.

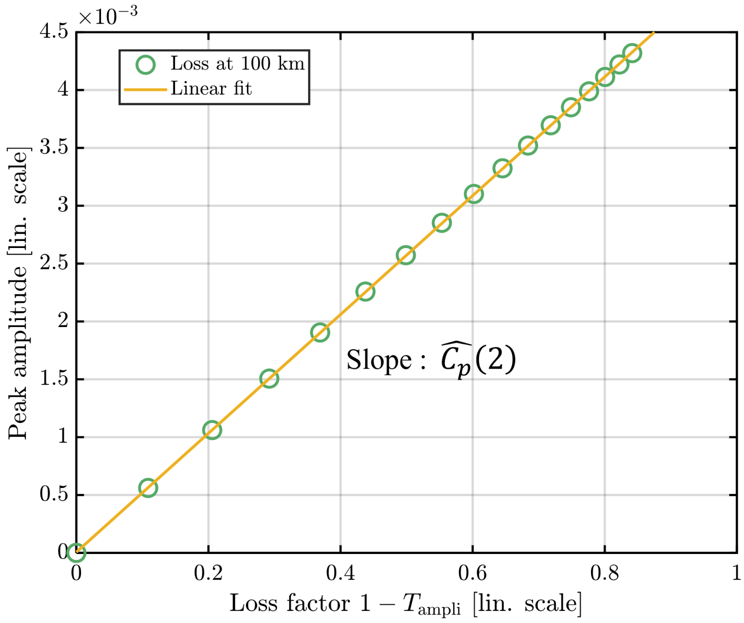

Figure 2.9: Measured peak amplitudes as a function of amplifier loss factors T_{ampli}. Output power of amplifier is $P(z^{(2)}) = P(100\text{ km}) = T_{\text{ampli}} \cdot P_{\text{ref}}(100\ km)$. The slope is the estimation of calibration factor $\widehat{C_p}(2)$.

To determine the **calibration factor** present in Eq. (2.10), we propose the following methodology. We propose to vary the output power - with respect to the reference one $P_{\text{ref}}(z^{(k)})$ - of an amplifier located at the beginning of a span to mimick power losses and evaluate the peak amplitude associated with a given loss value. Eq. (2.10) can be written in the case of $z_0 = z^{(k)}$ as:

$$A_{\text{peak}}(z_0 = z^{(k)}, T_{\text{ampli}}) = C_p(k) \cdot (1 - T_{\text{ampli}}), \tag{2.11}$$

where T_{ampli} is the transmission factor between the reference ouptut power and the new ouptut power $P(z^{(k)})$ such that $P(z^{(k)}) = T_{\text{ampli}} \cdot P_{\text{ref}}(z^{(k)})$. We plot in Fig. 2.9 measured peak amplitudes as a function of the amplifier loss factors $(1 - T_{\text{ampli}})$. The calibrated amplifier is located at 100 km. According to Eq. (2.11), $C_p(k)$ can simply be evaluated by performing a linear regression on these data. The estimation will be denoted as $\widehat{C_p}(k)$.

To determine the **position of the amplifier** at the beginning of span k, we rely on the AI peak position during calibration step. In Fig. 2.10, we plot - denoted by “Calibration” - the derivative of the AI when T_{ampli} is set to 0.5 such that the output power of the amplifier is $P(z^{(k=2)}) = 2$ dBm $= 10 \cdot \log_{10}(T_{\mathrm{ampli}}) + 5$ dBm. The position $z^{(k)}$ of the amplifier is estimated by searching for the peak position. In Fig. 2.10, we can see that the peak position is around 100 km so here the estimation $z_{\mathrm{cal}}^{(k=2)}$ is close to the real amplifier position $z^{(k=2)}$. In Fig. 2.11, we plot the AI for the same case. During calibration step, we also measure the peak position of the “Calibration” AI which is denoted by $\underline{z}_{\mathrm{cal}}^{(k=2)}$. We see that this position is slightly shifted from the $z_{\mathrm{cal}}^{(k=2)}$ and the shift depends on the peak shape and is found to be constant for given transmission parameters.

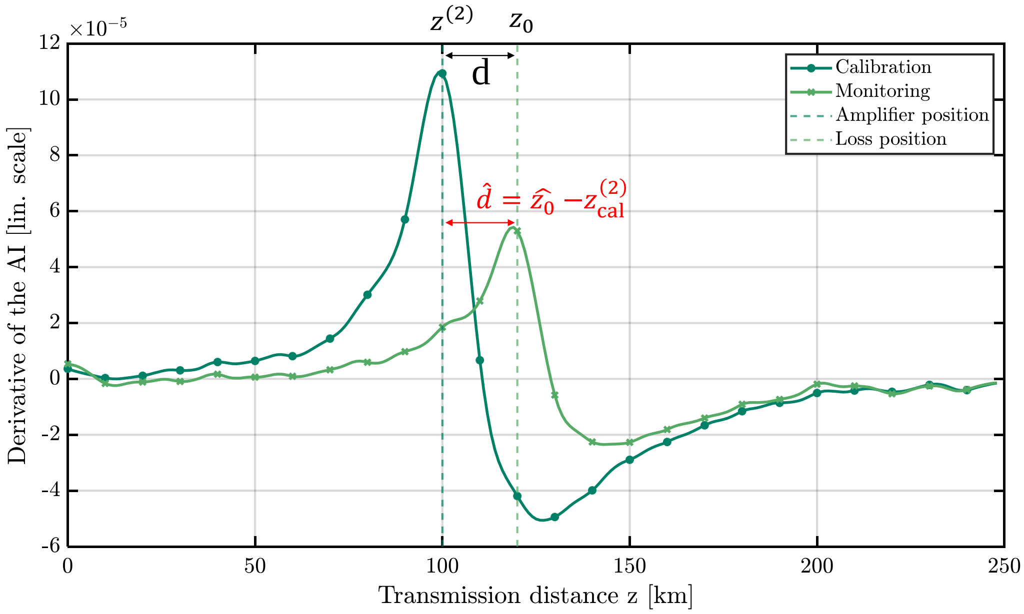

Figure 2.10: Derivative of the AI. Calibration: Output power of amplifier is set to $P(z^{(k=2)}) = 2$ dBm $= 10 \cdot \log_{10}(T_{\mathrm{ampli}}) + 5$ dBm. Monitoring: a 4-dB loss is inserted at $z_0 = 120$ km. Markers are drawn every 10 data points, i.e., every 10 kms.

The notation $\underline{z}$ indicates that the calibration or estimation is performed using the peak position in AI while the notation z is for the peak position in the derivative of the AI, as seen in Fig. 2.10. In all cases, the peak position is simply estimated as the maximum value.

Monitoring phase

During this phase, a monitoring power profile is computed periodically to study the evolution of the AI and possibily detect incoming power losses. To characterize

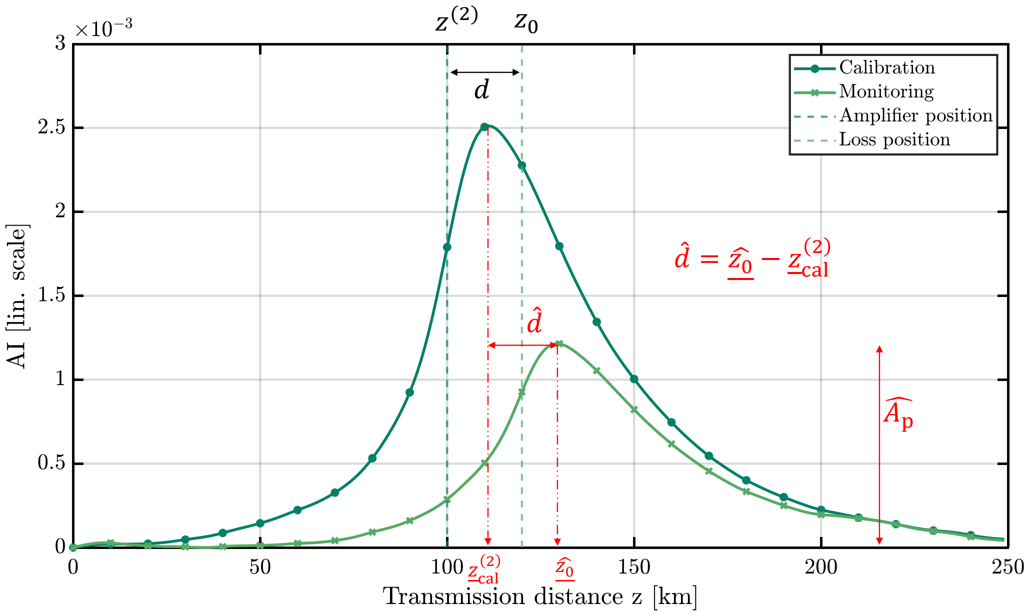

Figure 2.11: AI. Calibration: Output power of amplifier is set to $P(z^{(k=2)}) = 2$ dBm $= 10 \cdot \log_{10}(T_{\mathrm{ampli}}) + 5$ dBm. Monitoring: a 4-dB loss is inserted at $z_0 = 120$ km.

them, the position and the peak amplitude of detected peaks in the AI are measured. We rewrite Eq. (2.10) to have an expression of the loss factor which we want to estimate:

$$\widehat{T}_0 = 1 - \frac{\widehat{A}_p}{\widehat{C}_p(k)} \cdot 10^{\frac{\alpha_{\mathrm{dB}}}{10} \cdot \widehat{d}}, \tag{2.12}$$

where $\widehat{C}_p(k)$ is the estimation of the calibration factor $C \cdot P_{\mathrm{ref}}(z^{(k)})$ of span k during calibration step, $\widehat{A}_p$ is the measured peak amplitude and $\widehat{d} = \widehat{z}_0 - z_{\mathrm{cal}}^{(k)}$ is the measured position of the loss with respect to the calibrated position of the amplifier.

To determine $\widehat{d}$ two ways are possible, either by analyzing the derivative of the AI, or by using the AI itself. In Fig. 2.10, we plot the derivative of the AI during monitoring phase when a 4-dB loss is inserted at $z_0 = 120$ km, so $d = 20$ km after the second amplifier. We specifically show the quantity $\widehat{d}$ which is the estimation of d present in Eq. (2.12). $\widehat{z}_0$ is obtained by searching for the position of the peak in the “Monitoring” curve. Then, $\widehat{d}$ is obtained by retrieving the calibrated position of the amplifier $z_{\mathrm{cal}}^{(2)}$.

We can also obtain $\widehat{d}$ from the AI itself. For that purpose, in Fig. 2.11, we plot anomaly indicators for the “Monitoring” case and the “Reference” case with the same configurations as in Fig. 2.10. $\widehat{d}$ is the difference between the peak position for the "Monitoring" case $\widehat{\underline{z}_0}$ and the other calibrated position $\underline{z}_{\mathrm{cal}}^{(k=2)}$, which is the peak position for the "Reference" case.

These two positions do not correspond to absolute positions but they hold information about both cases. This second way of estimating the distance d of the loss with respect to the amplifier can be useful when there is already much noise in the AI. In this case, the derivative is even noisier which makes the measurement more accurate with the AI rather than with its derivative. In this manuscript, we will specify when using one or the other.

Finally, as shown in Fig. 2.11, on the "Monitoring" AI, we measure the peak amplitude $\widehat{A_p}$ and we can use Eq. (2.12) to obtain the estimation $\widehat{T_0}$ of loss factors .

2.3 Experimental demonstration

In this section, we will present the experimental demonstration of the proposed method on a 300-km optical link.

2.3.1 Experimental set-up

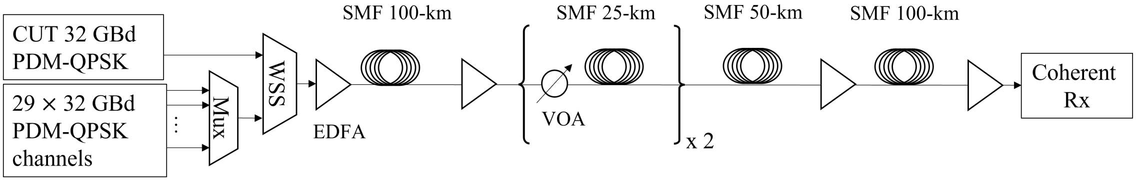

Figure 2.12: Schematic of the experimental set-up. Mux: multiplexer. WSS: wavelength selective switch. VOA: variable optical attenuator.

We depict in Fig. 2.12 a schematic of the experimental set-up we use to demonstrate the validity of the proposed method. We consider a 300-km fiber link composed of three 100-km spans of SMF. Thirty 32 GBd PDM-QPSK modulated channels are used. The channel under test (CUT) is digitally pre-distorted with a cumulated chromatic dispersion (CD) of 3000 ps/nm. The launch power at every span is 5 dBm for the CUT and 0 dBm for each adjacent channel. The attenuation constant of the fibers is equal to $\alpha_{\mathrm{dB}} = 0.206$ dB/km. The total cumulated CD of the link is 5100 ps/nm. A variable optical attenuator (VOA) is placed sequentially i) at 0 km, ii) at 25 km into the second span. The inserted losses may vary from 1.6 dB to 10.0 dB. We acquire samples from the four real-valued outputs of the coherent receiver sampling at a rate of 200 GSamples/s.

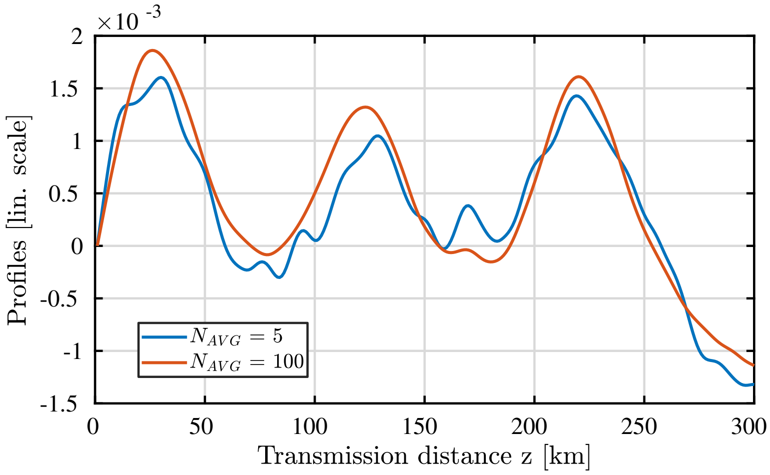

Figure 2.13: Experimental results. Aligned reference power profiles obtained with two different numbers of averaged elementary profiles $N_{\mathrm{AVG}} = 5$ and $N_{\mathrm{AVG}} = 100$.

To estimate power profiles, we use here the "original correlation-based" technique presented in Section 1.4.2 and whose algorithm is presented on a schematic diagram in Fig. 1.12, as in the simulations. We choose to compute power profiles by applying the algorithm on a field of length $N_{\mathrm{s}} = 2048$ samples at 2 samples per symbol (sps). We call elementary power profile a profile computed with one field of N_{s} samples. In experiments and in simulations, because of the different noises, several elementary power profiles need to be averaged to obtain a certain accuracy. We call N_{AVG} the number of averaged elementary power profiles. As an example, we plot in Fig. 2.13 two power profiles, one with $N_{\mathrm{AVG}} = 5$ and the other with $N_{\mathrm{AVG}} = 100$. They are aligned by removing their value for $z = 0$ for clarity. We observe that the level of noise is decreased by increasing N_{AVG}. As in previous simulations, we set the spatial granularity to $\Delta z = 1$ km, which means that in Fig. 2.13, there are 301 points. We also set the non-linear phase remediator parameter to $\epsilon = 0.01$.

2.3.2 Experimental results

We now apply the proposed method to characterize - locate and estimate - power losses and to evaluate its accuracy. After performing the calibration step, we present the results on the accuracy of the estimation of power losses.

Calibration step

The reference power profile is computed and stored with the initial output power of 5 dBm for all amplifiers. We plot in Fig. 2.14 three AIs corresponding to three power losses at 100 km : 1.6 dB, 3.79 dB and 5.86 dB. The AI are obtained with $N_{\mathrm{AVG}} = 20000$ averaged elementary AIs.

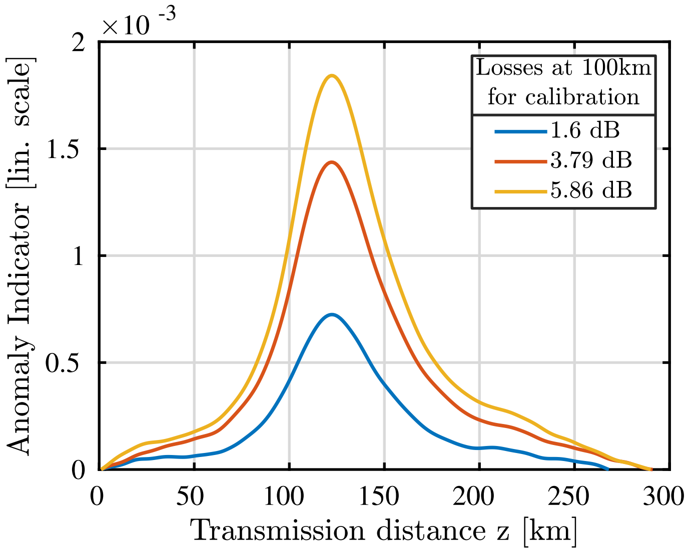

Figure 2.14: Experimental results. Anomaly indicators in presence of losses located at 100 km for the calibration step. Three curves are plotted corresponding to three different output powers of the amplifier. $N_{\mathrm{AVG}} = 20000$.

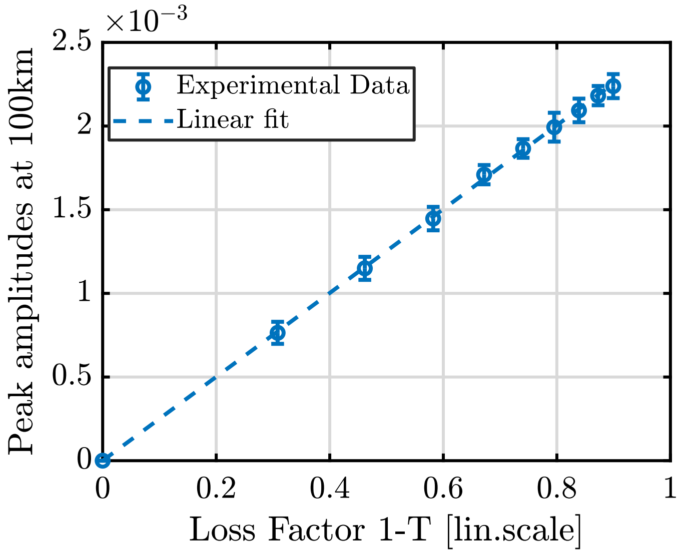

Figure 2.15: Experimental results. Averaged peak amplitudes as a function of loss factors for losses located at 100 km and 3-sigma error bars (over 30 realizations). $N_{\mathrm{AVG}} = 3000$.

For 30 realizations, we measure the peak amplitudes of the AI for every loss values from 1.6 to 9.97 dB and we plot the average value in Fig. 2.15 as a function of loss factors as well as 3-sigma error bars. For this figure, N_{AVG} was chosen to be 3000 in order to see the error bars.

We observe that the peak amplitudes are linear with the loss factors, as predicted by the model and observed by the simulations in Section 2.2. On top of that, the dispersion of the values is quite small. This confirms the relevance of peak amplitudes for loss value estimation.

To estimate the calibration factor, we choose $N_{\mathrm{AVG}} = 7000$ to compute the AI for each loss factor. We measure peak amplitudes and we perform a linear fit on $\widehat{A_p}(1-T)$. We obtain a calibration factor of $\widehat{C_{\mathrm{p}}}(2) = 2.51 \cdot 10^{-3}$. We also measure and store the position of the AI peak $\underline{z}_{\mathrm{cal}}^{(2)}$ and the position of the peak in the derivative of the AI $z_{\mathrm{cal}}^{(2)}$. The latter is the estimation of the position of the amplifier of the second span.

Loss values estimation

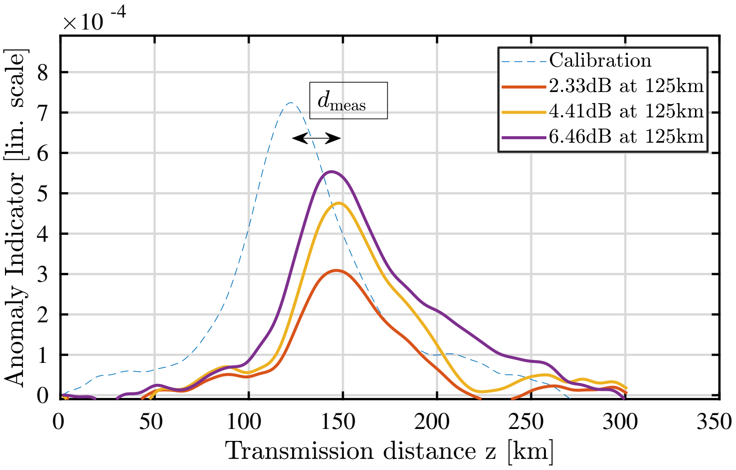

Figure 2.16: Experimental results. Aligned anomaly indicators in presence of 2.33, 4.41 and 6.46-dB power losses located at 125 km. In a dotted-line, aligned anomaly indicator in presence of a 1.6-dB loss for calibration. $N_{\mathrm{AVG}} = 20000$

.

We plot the AIs in the case of the 125-km power losses in Fig. 2.16 for three different loss values: 2.33, 4.41 and 6.46 dB. On the same graph, we plot as well the AI in the 100-km case in presence of a 1.6-dB loss to highlight the distance d to be measured between the calibrated amplifier position and the loss position. All AIs are plotted by averaging over $N_{\mathrm{AVG}} = 20000$ elementary AIs.

For each loss value, we measure 30 peak amplitudes and we plot the average values with 3-sigma error bars in Fig. 2.17 as a function of applied loss factors. We also replot the peak amplitudes from Fig. 2.15 for the 100-km case to compare both cases. As before, for this figure, N_{AVG} was chosen to be 3000 in order to see the error bars. As for the 100-km case, the peak amplitudes are linear with the loss factors,

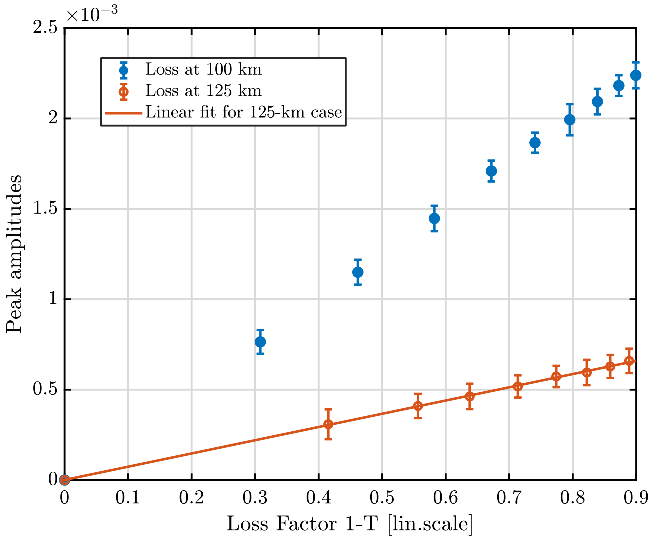

Figure 2.17: Experimental results. Average values of peak amplitudes with 3-sigma error bars (over 30 realizations) as a function of loss factors for the 100-km and 125-km cases. $N_{\text{AVG}} = 3000$.

as predicted by the model and observed by the simulations. We can see that, the dispersion of the values is quite similar to that of the 100-km case. However, since the peak amplitudes are much smaller, the 125-km case will not tolerate as much noise as the 100-km case.

For each loss value and for both cases - 100-km and 125-km -, we also measure the distance $\widehat{d}$. To do that, we choose to rely on the AI. For the 100-km case, the dispersion of obtained distances is very small, such that in 85% of cases, the AI peak is located at the exact same position as the calibrated amplifier position, making the distance equal to zero. This is rationnal since the loss is located at the position of the amplifier. To see the dispersion in the measured distances in the 125-km case, we plot in Fig. 2.18 an histogram of measured distances $\widehat{d}$ for $N_{\text{AVG}} = 20000$, for all 8 loss values and 31 realizations, such that there are 248 measured distances. The average value is 24.5 km and the standard deviation is 1 km.

Finally, we use Eq. (2.12) to estimate power losses for 100-km and 125-km cases and for all loss values. To assess the estimation accuracy, for each loss value, we use 30 AIs to perform 30 loss estimations. Each of those 30 AIs is computed by averaging over N_{AVG} elementary AIs. We plot in Fig. 2.19 the average estimation for the 100-km case for each inserted loss value as well as 3-sigma error bars. We observe that the estimation is quite good. We measure a bias and a standard deviation smaller than 0.2 dB for all loss values. We plot in Fig. 2.20 the average estimation for the 125-km case for each inserted loss value as well as 3-sigma error

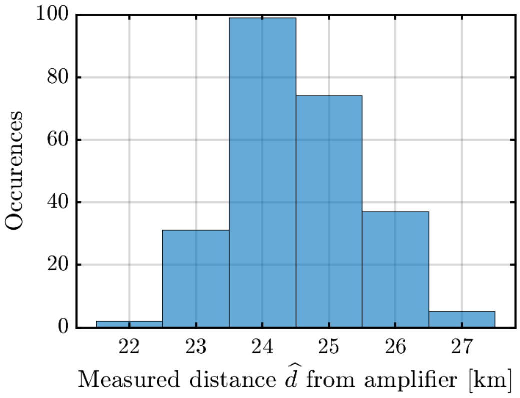

Figure 2.18: Experimental results. Histogram of the measured distances of loss from amplifier for the 125-km case. There are 31 distances for each of the 8 loss values, so 248 measured distances. $N_{\text{AVG}} = 20000$. Distances were measured using the AI.

bars. More specifically, we plot two cases. The one labeled "unknown" position corresponds to the case where both the position and the loss value are extracted from the AI. This is what was done for the 100-km case and is the realistic case. Indeed, obtaining elsewhere the information on the loss position is challenging, if no optical time-domain reflectometer (OTDR) is used. The one labeled "known position" corresponds to a case where the loss position is assumed to be known. In the latter case, in Eq. (2.12), we set $\widehat{d}$ to the value measured with an OTDR, which is 25 km. In the first case, the estimation is good for losses smaller than 5 dB since the bias is smaller than 0.2 dB and the standard deviation is smaller than 0.2 dB as well. For losses greater than 5 dB, we see that both the bias and the standard deviation are higher. If we look at the "known position" case, we see that both the bias and the standard deviation are smaller. Therefore, part of the uncertainty on the estimated loss values is due to the uncertainty on the estimation of the loss position. For example, for the loss value of 9.5 dB, the average - over the 30 realizations - estimated distance is 23.5 km, when it is 25.03 km for the loss of 3.5 dB which is more accurately estimated. Interestingly, we overestimate at 26 km for the loss of 4.41 dB. In the graph, for this loss, we see that the average estimated loss value is higher for the case "unknown" position than for "known" position.

Finally, we can observe that, even when assuming that the loss position is known, we still observe a certain estimation error, which is of 0.9 dB (8.6 is estimated instead of 9.5 dB) for the higher loss value. We can explain this by comparing in Fig. 2.17 the slopes of peak amplitudes of the 100-km case versus that of the 125-km case. The slope value of the 100-km case is the estimated calibration factor $2.51 \cdot 10^{-3}$. From Eq. (2.10), we know that the expected slope for the 125-km depends on

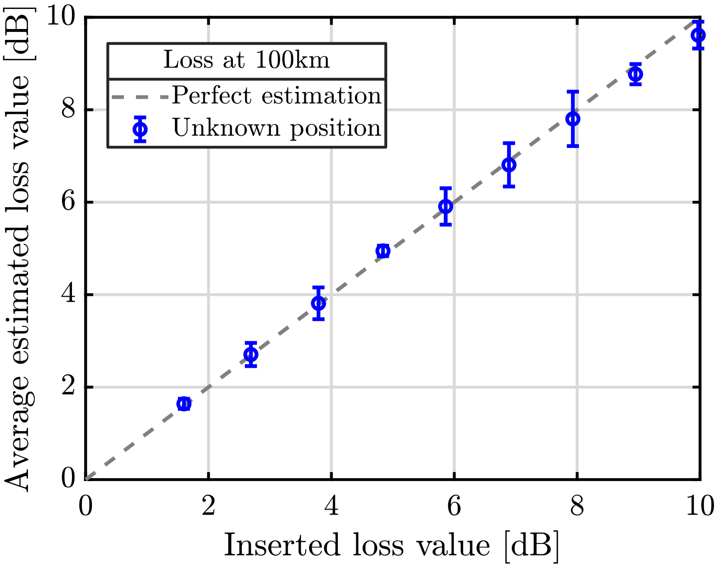

Figure 2.19: Experimental results. Average (over 30 realizations) estimated loss value with 3-sigma error bars as a function of inserted loss values in dB scale for the 100-km case. $N_{\text{AVG}} = 20000$.

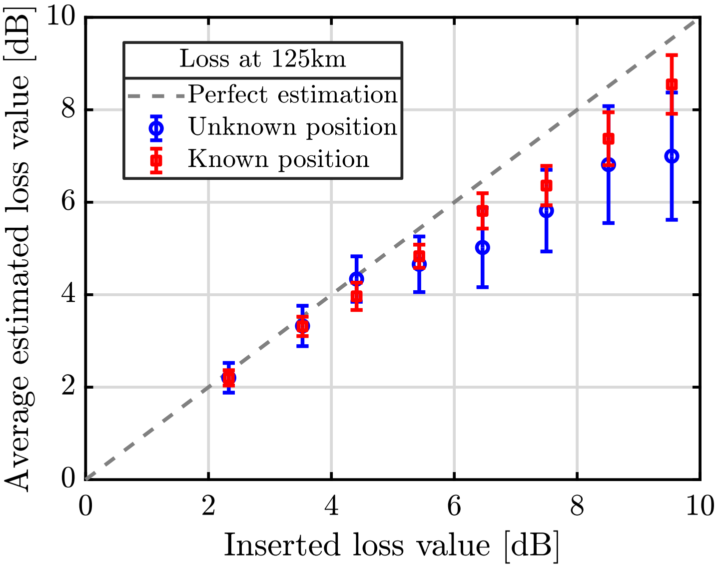

Figure 2.20: Experimental results. Average (over 30 realizations) estimated loss value with 3-sigma error bars as a function of inserted loss values in dB scale for the 125-km case. $N_{\text{AVG}} = 20000$.

the calibration factor and on the attenuation term. We can therefore calculate the expected value of the slope: $2.51 \cdot 10^{-3} \cdot 10^{-\alpha_{\text{dB}} \cdot 25/10} = 0.77 \cdot 10^{-3}$. When we perform a linear regression on the data shown in Fig. 2.17, we obtain $0.73 \cdot 10^{-3}$, which is a bit different from the expected value calculated ealier $0.77 \cdot 10^{-3}$. For the 125-km case, we thus measure peak amplitudes smaller than what is expected from the calibration factor or in other words from the 100-km data. We are thus underestimating power loss values. This explains why even when we suppose loss position to be known for the 125-km case in Fig. 2.20, the red squares are below the perfect estimation dotted-line.

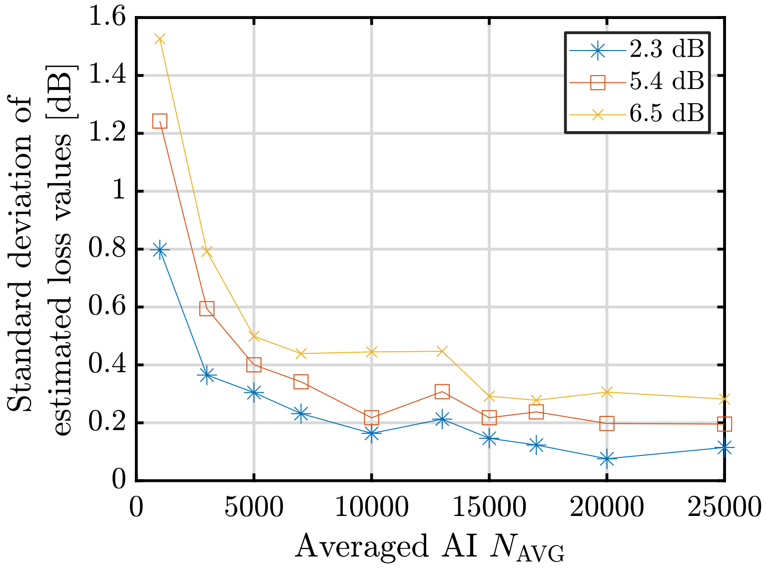

Figure 2.21: Experimental results. Standard deviation (over 20 realizations) of loss values estimations as a function of the number N_{AVG} of averaged elementary AIs.

Finally, we study the impact of increasing the number of used data samples to compute power profiles, or in other words, the number of averaged elementary AIs, on the accuracy of the estimation. To do that, we vary N_{AVG} from 100 to 25000 and we estimate loss values with 20 realizations per N_{AVG} and per loss value. We plot in Fig. 2.21, the standard deviation of loss value estimations over the 20 realizations for three loss values in the 125-km case as a function of N_{AVG}. We see that increasing the number of averaged elementary profiles increases greatly the accuracy. We also observe that, for N_{AVG} greater than 20000, the accuracy stops improving and we reach an asymptote.

2.4 Conclusion

In this chapter, we numerically and experimentally investigated the possibility to obtain accurate measurements with the correlation-based power profile estimation technique. For simulations and experiments, we use the “original correlation-based” technique initially proposed by Tanimura et al. in [17].

To this end, we propose a simple model describing the behavior of the power profile, and leading a mathematical description of the anomaly indicator (AI) and the AI peak amplitudes induced by power losses. The proposed model is first validated by numerical simulations using the split-step Fourier method (SSFM) to emulate non-linear effects and inserting power losses of different values at different positions. Drawing on this model, we propose a calibration-based method to estimate both the position and the value of potential power losses.

We then experimentally apply the proposed method on a 300-km link, composed of three 100-km spans. We inserted power losses at 100 km - which is the position of an amplifier - and at 125 km. We varied the power loss values from 1.6 to 10.0 dB. For losses at 100 km, the loss value estimation was very accurate, with a bias and a standard deviation lower than 0.2 dB for all loss values. The loss value estimation was also accurate for losses located at 125 km of up to 5 dB. For higher loss values, the bias and the standard deviation are increasing. A part of the uncertainty on the loss value estimation is due to the uncertainty on the loss position estimation which is found to be higher for higher loss values. Indeed, for the loss value of 9.5 dB, the average - over the 31 realizations - estimated distance is 23.5 km, when it is 25.03 km for the loss of 3.5 dB, closer to the real value of 25 km. We finally show how increasing the number of data samples used to compute power profiles helps increasing the estimation accuracy.

The estimation of both the value and the position of the loss is quite accurate, offering promising solutions for anomaly detection schemes. The estimation is more challenging when the loss is located further away from the amplifier since the peak amplitudes are smaller. For the same amount of noise in the profile and the same loss value, a higher signal-to-noise ratio (SNR) is expected for the peaks induced by losses close to the amplifier. In Chapter 3, we will investigate the use of multiple lightpaths in a meshed network to increase the estimation accuracy. We will also investigate anomaly detection on a long-haul optical link where the accumulated noise is quite high.

Chapter 3

Performance of power profile estimation in two use cases

3.1 Introduction

The calibration-based method to characterize power losses has been tested experimentally in a point-to-point scenario where the optical link is 300-km long. In real telecom systems, there can be various transmission scenarii, such as meshed networks for metro networks or ultra long links for submarine systems. Applying a longitudinal power monitoring technique coupled with a power losses characterization method is interesting for different reasons but can also imply several challenges.

In a meshed network, we can benefit from the various lightpaths and available monitoring information to improve the accuracy and reliability of the method. However, the growing number of transmission schemes could imply a high number of calibration factors to be estimated.

Monitoring of submarine links implies the surveillance of a high number of amplifiers which is an additional constraint in an environment where power requirements are stringent. In this context, only relying on the analysis of the output signal with this digital signal processing (DSP)-based power profile estimation technique can help reducing the complexity and the cost of monitoring. However, applying a method based on the analysis of the received signal on long transmission distances is a challenge because of the accumulated noise, such amplified spontaneous emission (ASE) or self-phase modulation (SPM) noises.

The chapter is organized as follows. In Section 3.2, we study experimentally the application of the power losses characterization method proposed in Chapter 2 in a meshed network. We show how using already monitored information can ease the implementation of the method and we estimate the gains in accuracy of combining estimations from multiple lightpaths. In Section 3.3, we study the application of the longitudinal power monitoring technique in a straight link of more than 10000 km. To our knowledge, the longest transmission distance over which a power profile was computed is 2000 km using a recirculating loop in [19]. We show the successful estimation of longitudinal power profiles perfomed on channels with two symbol rates and a total transmission distance of more than 10000 km as well as the successful detection of two simultaneous power anomalies.

3.2 Power losses characterization in a meshed network

3.2.1 Context

As already mentioned, a meshed network will bring additional features to our power losses characterization method. First, when an extra loss occurs in a fiber span, several lightpaths going through this fiber hold information on the loss characteristics. In this case, several estimations of the same loss can be performed at different receivers. Secondly, in a network, many parameters are already monitored, such as the ouptut and input optical powers of optical amplifiers. In Chapter 2, we observed that increasing the amount of samples helps decreasing the standard deviation of the loss value estimation. However, we observed that biases in the measurement of the loss value and position still remain. Those biases can be due to several factors, including but not limited to the deficient performance of a lightpath, an unaccurate total transmission distance or biases in the DSP algorithms. That is why we propose to study the combination of estimations from several lightpaths to decrease biases and to improve the accuracy of the method.

On another note, adapting the proposed method presented in Chapter 2 to an elastic network can imply many challenges. Indeed, in a network, lightpaths have various total lengths and span lengths. In an elastic network, each lightpath can have different transmission parameters, such as the symbol rate, the power or the modulation format. In Chapter 2, the method is based on a calibration step. The calibration factor, being estimated from correlation factors, depends on the total accumulated noise which itself depends on the transmission parameters. Therefore, a direct application of the method, for N given lightpaths with m given transmission parameters would require $N \cdot m$ calibration factors.

In this section, we first study how the calibration factors can be generalized for different lightpaths and for various powers. Then, we estimate the gains in accuracy of combining estimations from several lightpaths.

3.2.2 Experimental set-up

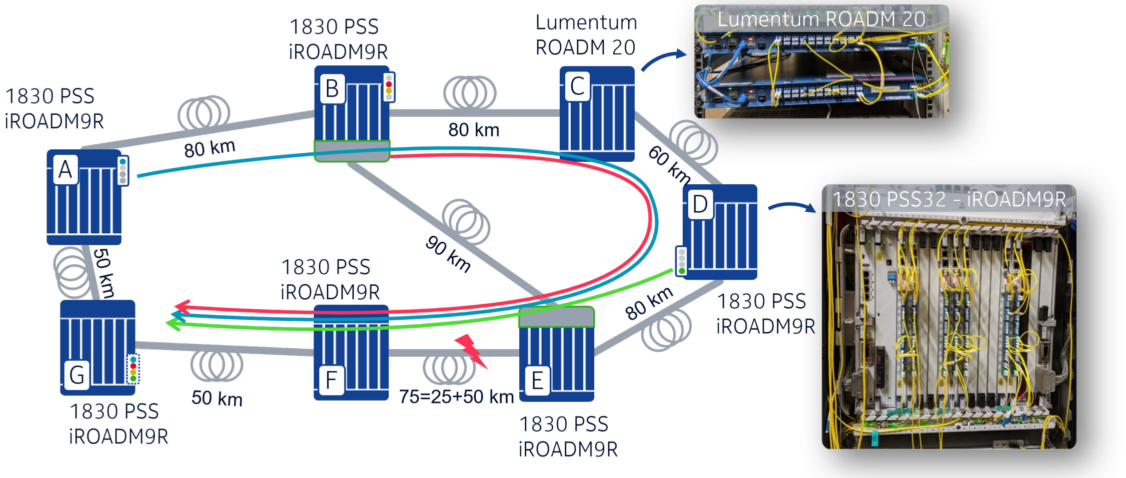

Figure 3.1: Experimental set-up of the meshed network.

To conduct the two studies, we performed experiments on the meshed optical network testbed depicted in Fig. 3.1. It is composed of seven nodes built from 3 vendors (Nokia, Lumentum and a prototype). The outer ring ranges 475 km of standard single mode fiber (SSMF) optical fiber. The testbed devices are operated via Netconf thanks to ADONIS Open agent [61], also enabling enhanced monitoring. We load the network with 20 ASE channels aligned on the 50GHz ITU grid. Three 32 GBaud polarization-division multiplexing (PDM)-quadrature phase shift keying (QPSK) channels are generated by a Nokia 1830 PSI-2T, named Line 1, 2 and 3 (in blue, red, and green), injected from distinct source nodes, A, B and D and received at the same destination node G after propagating through 421 km, 341 km and 202 km of optical fiber, respectively. These optical channels are both decoded by a Nokia 1830 PSI-2T and are also sent to an offline coherent receiver with 70 GHz bandwidth and 200 GSamples/s real-time oscilloscope. The network testbed is operated in a constant power mode, i.e., the output power of nodes is maintained constant regardless of the input power. Finally, a programmable variable optical attenuator (VOA) is placed after 24.02 km (optical time-domain reflectometer (OTDR) estimation) of propagation in the penultimate fiber span, i.e., between node E and F, and enables the insertion of extra power loss (red lightning in Fig. 3.1). The loss values are varied from 0.5 to 8 dB. When not specified, the channel launch power is 5 dBm.

3.2.3 Longitudinal power profile monitoring with three lightpaths

In this section, we present the methodology of the conducted experiment as well as the common thread between the two following studies.

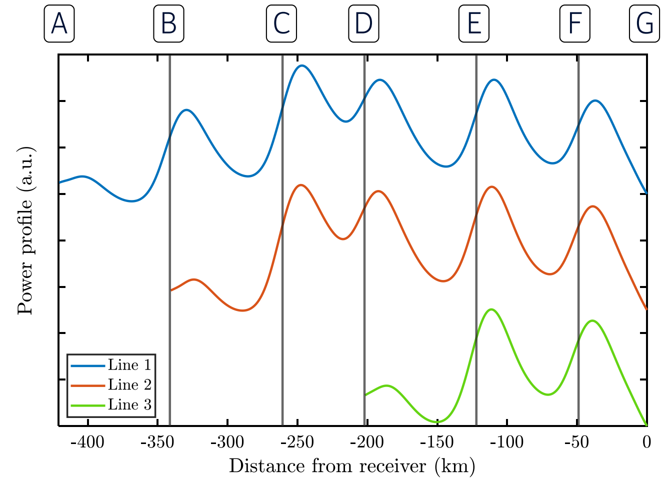

(a) Reference power profiles.

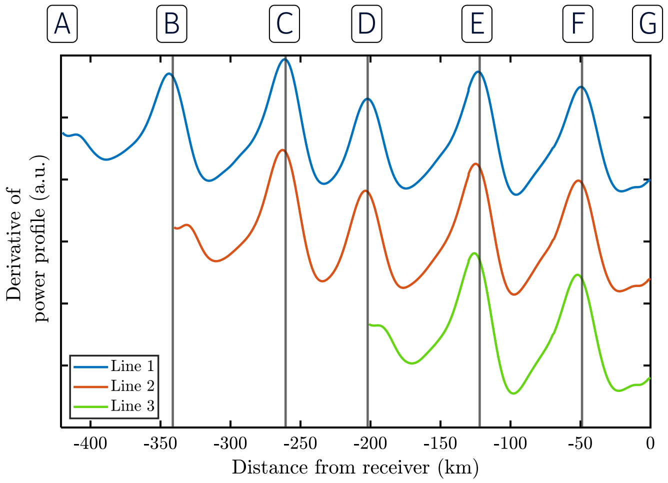

(b) Derivative of the reference power profiles.

Figure 3.2: Reference power profiles for the three lines. Vertical black lines correspond to the position ot the amplifiers. Letters correspond the node indices presented in Fig. 3.1.

Computing reference power profiles

To monitor our meshed network, we first compute reference power profiles for each of the three lines 1, 2 and 3 with the "original correlation-based" technique presented in Section 1.4.2 and whose algorithm is presented on a schematic diagram in Fig. 1.12. Each elementary power profile is computed using 2048 received samples, as in the experiments shown in 2.3. As before, the step chosen is $\Delta z = 1$ km and the non-linear phase remediator parameter is set to $\epsilon = 0.01$.

We plot in Fig. 3.2a the average power profiles for each of the three lines and in Fig. 3.2b their derivative as a function of the distance in km with respect to the common receiver of node G. Here, we averaged over $N_{\mathrm{AVG}} = 65000$ elementary power profiles, which is the total available number of profiles. We add the indices (letters) of nodes along with vertical lines to show their position. In Fig. 3.2b, we notice that the position of the maximum of the peaks correspond to the nodes position (solid black line).

Calibration step

We then proceed to the calibration step for each of the three lines, which is identical to the one described in 2.2. We attenuate the output power of the amplifier at node E from the initial value $P_0 = 5$ dBm to $P = -3$ dBm by steps of 0.5 dB. In other words, we vary the transmission factor T so that the various output powers P can be written $P = T \cdot P_0$. For each P and each of the three lines, we compute an anomaly indicator (AI) and we measure the amplitude of the peak $\widehat{A}_{\mathrm{p}}$. We can then perform a linear regression of the data set $\widehat{A}_{i,\mathrm{p}}$ with $(1 - T)$ as the x-axis and obtain the calibration factor for each of the three lines $\widehat{C}_{\mathrm{p},i}(\mathrm{E})$ with $i = \{1, 2, 3\}$. For clarity, $\widehat{C}_{\mathrm{p},i}(\mathrm{E})$ is the calibration factor estimated by varying the output power of the egress amplifier of node E and analysing data from line i. It allows the estimation of power losses located between node E and node F. A number of $N_{\mathrm{AVG}} = 65000$ elementary AIs was used for this calculation.

Monitoring phase

Finally, we can focus on the monitoring phase. We plot in Fig. 3.3 the AIs for each line as well as their derivative. 65000 elementary AIs were used for these two graphs. They are plot in presence of a 3-dB loss 25 km from the node E. The vertical dotted line coresponds to the position of the loss. We notice that all three peaks are located - with small errors - at the position of the loss in Fig. 3.3b, which is a first validation of the monitoring of this meshed network. We also notice that each of the three peaks in Fig. 3.3a are quite similar in terms of amplitude. In the following, we will rely on the loss value and loss position estimations, performed for each 3 lines and each 16 values of attenuation. Those estimations are performed in the same way as

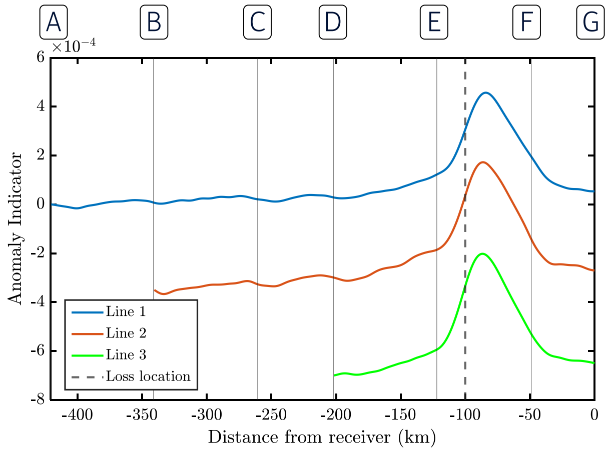

(a) Anomaly indicators.

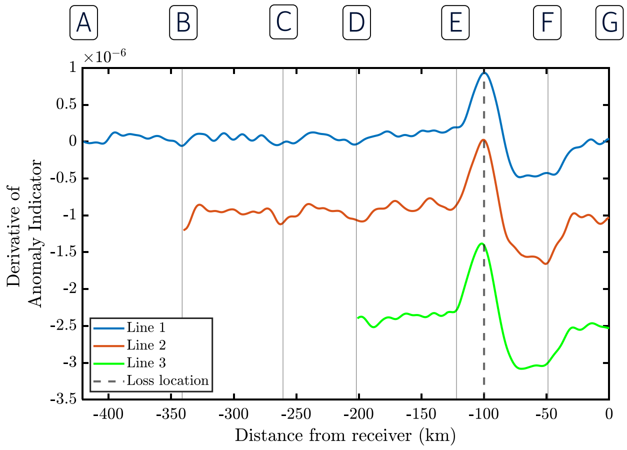

(b) Derivative of the anomaly indicators.

Figure 3.3: Anomaly indicators for the three lines for a 3-dB loss at 25 km from node E. Vertical dotted-line corresponds to the position of the inserted loss.

described in Section 2.2. The number N_{AVG} of averaged profiles or AIs used for the estimations will be provided in each of the two following studies.

3.2.4 Calibration generalization in an optical network

The first study concerns a generalization of the calibration factors.

Generalization over the three lines

First, we study the feasibility to use the same calibration factor for several lines. To do that, we perfom loss value estimations for lines 1 and 3 with different calibration factors: one with the corresponding factor (inner calibration) and one with the factor of another line (outer calibration). For each loss value, 5 estimations are performed,

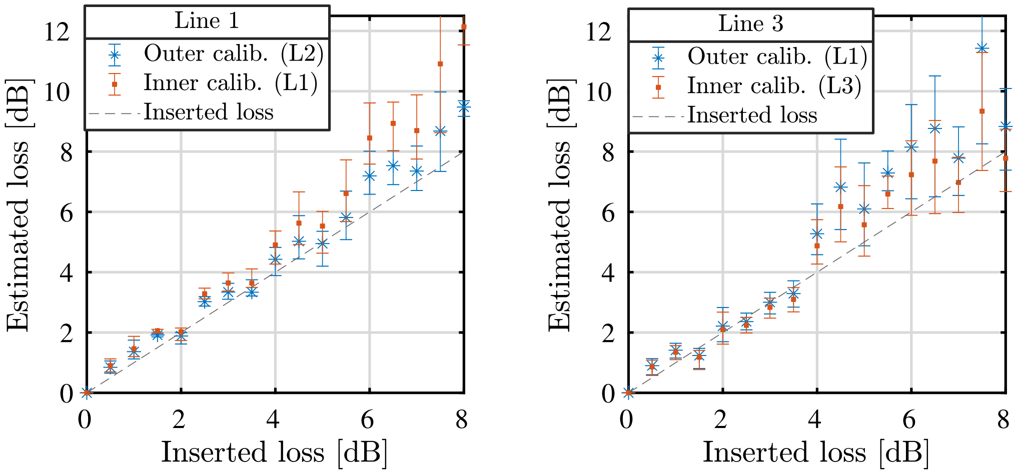

(a) Loss value estimations for line 1. **(b)** Loss value estimations for line 3.

Figure 3.4: Loss value estimations for line 1 and 3 using the inner calibration factor and the calibration factor of another line (outer).

each using a power profile obtained by averaging over 12000 elementary ones. We plot in Fig. 3.4 the average estimated loss (over 5 realizations) for line 1 versus the inserted loss value when the calibration factors of line 1 and 2 are used, (resp. for line 3 with factor of line 3 and 1). The errors bars correspond to the maximum and minimum estimated values.

We notice that though the estimation is better when the inner calibration factor is used in Fig. 3.4b (red squares), in Fig. 3.4a, it is not the case. We attribute such discrepancy to the intrinsic error of the estimation which is of the same order of magnitude as the error obtained when using an outer calibration error. Either way, we see that the estimation remains accurate when using the calibration of another line, which has a different propagation distance, from 202 km (line 3) to 421 km (line 1), a different performance and a different wavelength.

Generalization over the input power

Secondly, we study the generalization of the calibration factors with different launch powers. To perform that, we determine $\widehat{C}_{\mathrm{p}}(\mathrm{E})$ for various span launch powers per channel, from 5 dBm (3.16 mW) to -2.5 dBm (0.56 mW). The results are reported for each line in Fig. 3.5. We see that the calibration factors $\widehat{C}_{\mathrm{p},i}(\mathrm{E})$ are proportional

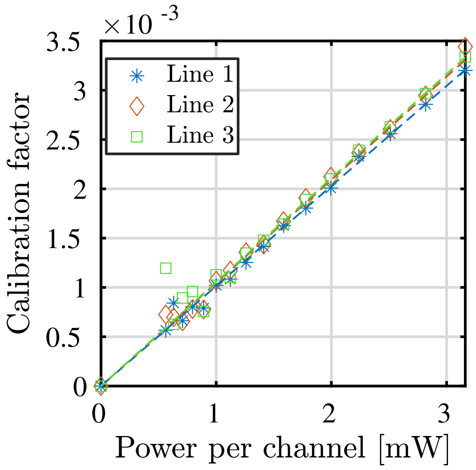

Figure 3.5: Calibration factors $C_{\mathrm{p},i}(\mathrm{E})$ for each of the three lines as a function of the power per channel in mW.

to the launch power P. We can look back at the expression of the calibration factor $C_{\mathrm{p}}(\mathrm{E})$ given by the model in Section 2.2: $C_{\mathrm{p}}(\mathrm{E}) = C \cdot P_{\mathrm{ref}}(\mathrm{E})$ where $P_{\mathrm{ref}}(\mathrm{E})$ is the power at node E. We see here that this experimental study confirms the validity of this formulation. We confirm here that the knowledge of one calibration factor is enough if the information of the launch power is known.

To conclude, we experimentally showed a sufficient accuracy when using the calibration factor of another line, which is different in terms of distance and wavelength. We also showed that calibration factors can be extrapolated from a single one with the knowledge of launch powers.

3.2.5 Gains of combining multiple lightpaths

The second study concerns the leveraging of several lightpaths to increase the accuracy of the method. The goal is to estimate the gain in accuracy from using several lightpaths, in terms of position and value estimation. In this study, the AIs are computed using 28000 elementary profiles with a 1-km resolution. Following the conclusion of the calibration generalization study and our goal to decrease complexity, we use only one calibration factor (from Line 2) for the loss value estimations. For each line and each loss, we estimate the distance $\widehat{d}$ from node E and loss value using directly the position of the peaks in the AI.

In Fig. 3.6, we report the mean, maximum and minimum estimated loss distances $\widehat{d}$ from the node E over the three lines as a function of inserted losses. For example, for an attenuation of 3.5 dB, one of the lines gives an estimated distance of 21 km. We see that the mean estimated distance over lines is very close to its measured value

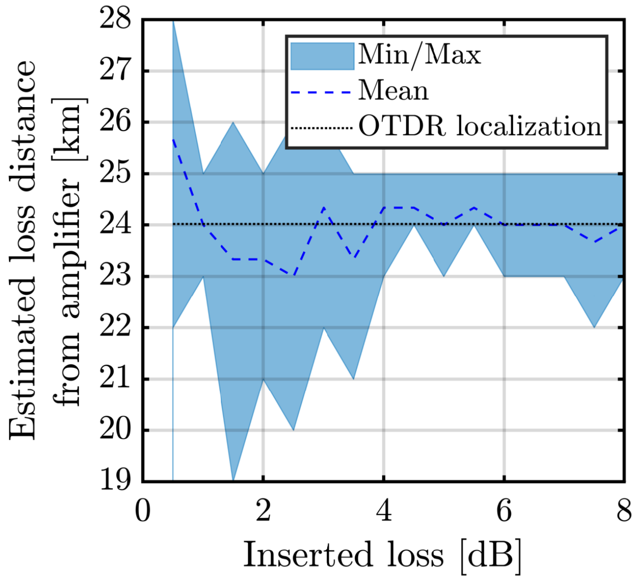

Figure 3.6: Mean, maximum and minimum estimated loss distances $\widehat{d}$ over the three lines versus inserted loss values.

(by OTDR) 24.02 km. We observe that for small losses, the single line estimations (maximum or minimum) can be quite far away from the OTDR value. For instance, for a loss of 2.5 dB, the single line location error can be up to 4 km, while it is reduced to 1 km when the three estimations are averaged. Thus, estimation diversity helps reducing the location error. This increase in location accuracy will also reduce the error on the fiber propagation loss term in Eq. (2.12) and thus reduce the loss estimation error.

In Fig. 3.7, we report the maximum and minimum estimated loss values over the three lines as a function of inserted losses. We also plot the mean, which is calculated using the mean (over the three lines) value of distances (showed in 3.6) and mean value of peak amplitudes. We observe that taking these mean values to perform the estimation allows an improvement of the accuracy. For example, for a 3-dB attenuation, the combined estimation error is 0.50 dB whereas one of the three lines alone gives an error of 1.40 dB. Overall, for all losses, the maximum error of the mean value is < 1.0 dB, and < 0.7 dB for losses < 4 dB. This highlights the benefits of combining the results of several lines.

As a conclusion, we proposed to combine estimations of the same loss from the analysis of multiple lightpaths. In this section, we estimated experimentally the gains of this combination. Estimating the same loss from multiple lightpaths allows two separate outcomes. First, combining them increases the accuracy of the estimations, both the loss value and the loss position. Secondly, it increases

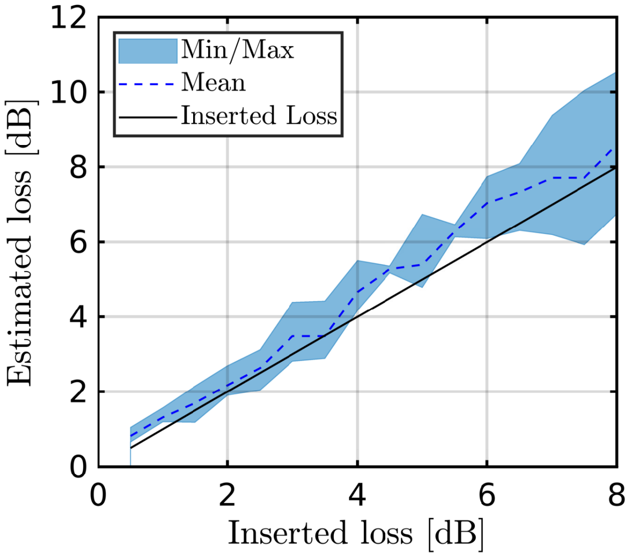

Figure 3.7: Mean, maximum and minimum estimated loss values over the three lines versus inserted loss values.

reliability since it avoids having to rely on a single line for monitoring.

3.3 Anomaly detection in a straight submarine link

3.3.1 Context

As briefly mentionned in the introduction of this chapter, applying a DSP-based method to monitor the longitudinal power is quite relevant for long-haul transmissions. Up to now, the OTDR, or a variant of it, is the standard tool to monitor longitudinal power in submarine systems [62]. However, it has its drawbacks. With the accumulated ASE noise and low-power Rayleigh backscattering, long averaging windows are required to obtain a reliable power profile estimation from the OTDR trace. Moreover, since the OTDR signal cannot go through amplifiers, a special scheme with filters and couplers is implemented. Given the high number of amplifiers, the cost of implementation can be quite high. Finally, since the electrical consumption of components is an important cost center and a technological challenge, passive solutions are quite attractive. That is why, being able to monitor in-service the longitudinal power without having to add special hardware and only based on a DSP analysis of the received signal is a very attractive monitoring solution for submarine systems.

However, the application of the power profile longitudinal technique for long-haul system encounters some challenges. Some are similar to that of the OTDR. The high amount of accumulated noise is a challenge for methods which are based on the analysis of received signal. On another note, previous demonstrations of power profile monitoring techniques all use a input power per channel of 5 dBm to exalt non-linear effects and more especially SPM effects. This power level is far from the optimal power used in submarine systems. Finally, in most correlation-based power profile demonstrations [17, 21], a certain amount of predispersion was digitally applied, from 15 to 40 % of total transmission distance. The objective of adding predispersion was to flatten the bell-shaped enveloppe of the profile and to decrease the difference in amplifier peaks seen in Section 2.2.2. In submarine systems, the total transmission distance is such that the amount of predispersion needed would be too high to be applied.

Therefore, a demonstration is needed to validate the use of this method in a submarine system. We choose to stick to the correlation-based techniques. Indeed, we believe that these techniques have a lot of potential for long-haul transmissions. With correlation-based techniques, each point of the profile can be computed independently from the others while for other techniques such as minimum mean square error (MMSE)-based, the full propagation must be performed. It can be quite complex and time-consuming for a simple monitoring task if the transmission is very long. This demonstration is the opportunity for us to apply the updated version “forward correlation-based” presented in Section 1.4.3 and whose algorithm is presented on a schematic diagram in Fig. 1.17. This is important because this updated version has a closed-form expression which can be useful for future investigations.

3.3.2 Experimental set-up

The experimental set-up is depicted in Fig. 3.8. We perform our experiments with a multi-channel transmission. The channel under test (CUT) are PDM-QPSK modulated. They are shaped with a root-raised-cosine filter with 0.01 roll-off factor. No digital chromatic pre-dispersion is applied. For the transmitted configurations, we consider two configurations depicted as i) and ii) whose differences are shown in bold in Fig. 3.8a and Fig. 3.8b. We indicate that the experiments in configuration i) were performed by the Alcatel Submarine Networks team at Nozay. They performed several acquisitions which they shared with us to perform a first demonstration of the longitudinal monitoring. For configuration ii), we define with them the experimental

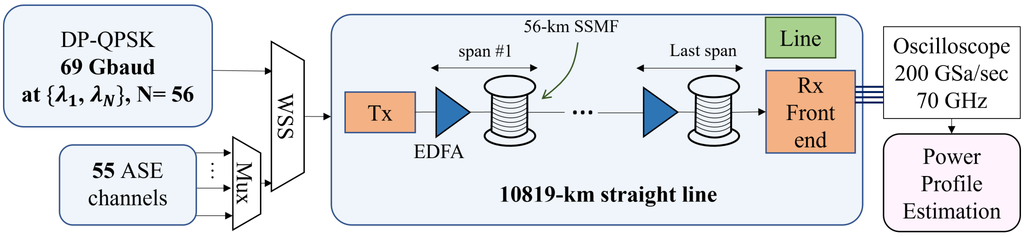

(a) Configuration i).

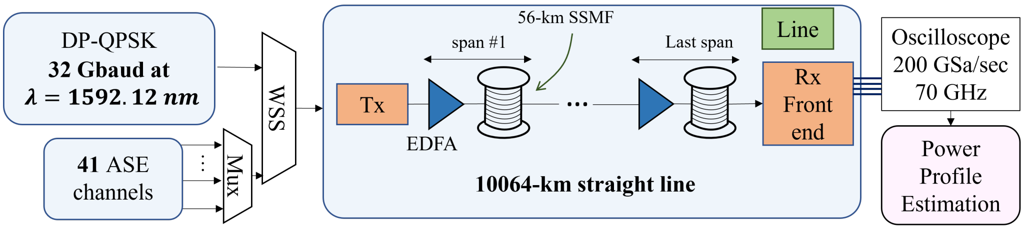

(b) Configuration ii).

Figure 3.8: Experimental setup.

set-up which we needed and participated in the experiments in October 2022. For both cases, we performed the DSP and additionnal processing for the longitudinal monitoring.

For configuration i), the baud rate is 69 Gbaud. The CUT is successively positioned at 56 different wavelengths ranging from 1534.25 to 1567.34 nm. Sequences of 2^{15} symbols are used for the transmitted signal. For configuration ii), the baud rate is 32 Gbaud and the wavelength of the CUT is set at 1550.12 nm. The bandwidth is loaded with ASE channels to reach for i) 56 channels 75-GHz spaced or for ii) 42 channels 100-GHz spaced. Sequences of 2^{17} symbols are used for the transmitted signal.

The channels are sent into a straight line of 56km-long Pure Silica Core Fiber spans with 110 μm^2 effective area. For the i) 69-Gbaud case, the line reaches 10819-km and 10064-km for the ii) 32 Gbaud case. We note that, in both cases, in the end of the line, a few spans of 70 to 80 km are present. We amplified the signal using 4.2 THz-wide C-band erbium-doped fiber amplifier (EDFA) operated in constant output power mode at 16.5 dBm to approach a real submarine operating point configuration. Under the hypothesis of the same power for all channels, the input span launch power of each channel is therefore equal to -0.98 dBm in the 69-Gbaud case and 0.27 dBm in the 32-Gbaud case. This power corresponds, for the 69-Gbaud case, to a power 0.5 dB below the nonlinear threshold.

For both configurations, the CUT is then sent to an offline coherent receiver with a 70 GHz bandwidth and 200 GSamples/s real-time oscilloscope and processed offline. For the configuration (i), 2 acquisitions of 4 million samples for each of the

56 channel frequencies are recorded. For the configuration (ii), we emulate power anomalies by modifying the target output power of the amplifiers at the beginning of two spans. We record 100 acquisitions of 50 million samples for each of the 3 dispositions: no attenuation, a 3-dB anomaly at 4804 km, two 3-dB anomalies at 4804 km and 7111 km.

The experimental parameters of both configurations are gathered in Table 3.1.

Configuration	i)	ii)
Baud rate [Gbaud]	69	32
Number of channels	56	42
Number of CUT	56	1
Input power per channel [dBm]	-0.98	0.27
Transmission distance [km]	10819	10064
Samples at 2 samples per symbol (sps) for elementary power profile	$2.6 \cdot 10^6$	$1.4 \cdot 10^6$
Number of profiles N_{AVG}	112	1000

Table 3.1: Experimental parameters of both configurations.

3.3.3 Longitudinal power profile monitoring

In this section, we present briefly how we compute power profiles for both configurations. This time, we choose the "forward correlation-based" technique presented in Section 1.4.3 and whose algorithm is presented on a schematic diagram in Fig. 1.17. Though the technique is almost similar in terms of results, its theoretical derivation is easier to perform, allowing for closed-form expressions [59, 63].

As in [19], we assume the transmitted sequence is known and acts as the reference signal S_{ref} in Fig. 1.17. The correlation is done with the fields at 2 sps. To map the distance with the chromatic dispersion, we use the ratio of the accumulated value of the dispersion over the total distance to define the amount of CD to be compensated at each coordinate of the profile. However, this ratio is only an average value and adds uncertainty to the coordinates.

We apply this updated algorithm to both configurations. For configuration i), each elementary power profile is computed using 1 acquisition which, with the several DSP operations amounts to $2.6 \cdot 10^6$ samples at 2 sps. 112 elementary power profiles are available. For configuration ii) each elementary power profile is computed using $1.4 \cdot 10^6$ samples at 2 sps and 1000 are available for averaging. These values are added in Table 3.1.

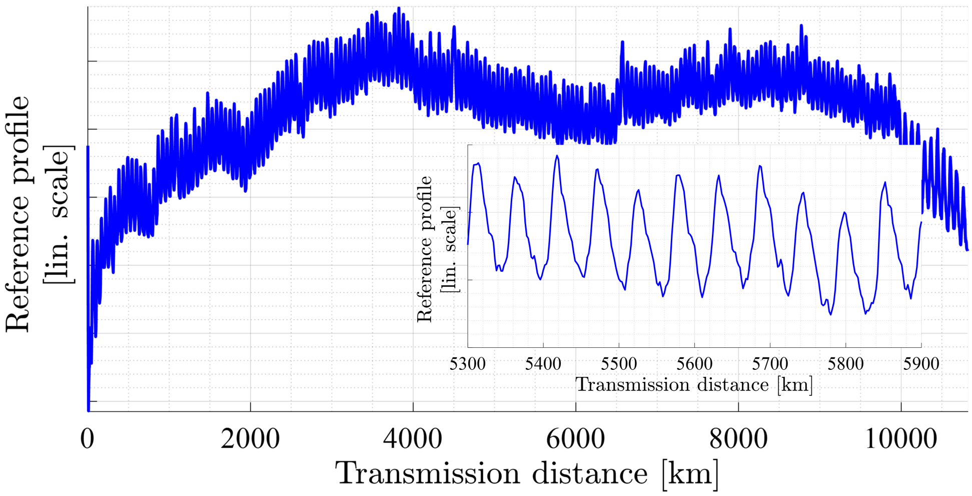

Figure 3.9: Reference power profile for configuration i) i.e., at 69 Gbaud and for 10819 km. Inset: reference profile over the range [5300 − 5900] km.

We plot in Fig. 3.9 and in Fig. 3.10 the reference power profiles for the configurations i) at 69 Gbaud and ii) at 32 Gbaud, respectively with insets corresponding to subset sections of the z-axis. Both profiles were computed using all available profiles, *i.e.,* 112 for the 69-Gbaud case and 1000 for the 32-Gbaud case. The chosen step is 4 km, except for two subsets [5300 − 5900] and [9800 − 10250] km where the chosen step is 2 km. For the 32-Gbaud case, in the subset [6850 − 7400] km, the step chosen is also 2 km. First, if we look at the insets, we see variations with a period of around 50 km over the z-axis, which is a first confirmation of the estimation of power variations. Plus, we observe that variations are sharper for the 69-Gbaud case, which is in line with the study in [22] where they show that increasing the symbol rate increases the spatial resolution. Then, if we look at the whole profiles, we notice a common shape, which is the bell-shaped enveloppe seen in 2.2.2. Much smaller values are observed with z close to 0 km and to 10819 km. In between, we also notice some waves. This is not in line with the expected set-up where each amplifier is set to target the same constant output power. Though the power should be varying between amplifiers due to attenuation, the power should always go back to the same one after each span. Other works managed to partially mitigate this distortion using digital predispersion of the transmitted field as proposed in [22]. We also used this in Chapter 2 and for the meshed network study. Here, we chose not to use a digital predispersion. This should not be an issue for the chosen context.

In the two following sections, we are going to first see the link between the observed profile and the actual topology in subset sections of the z-axis and then we will investigate anomaly detection.

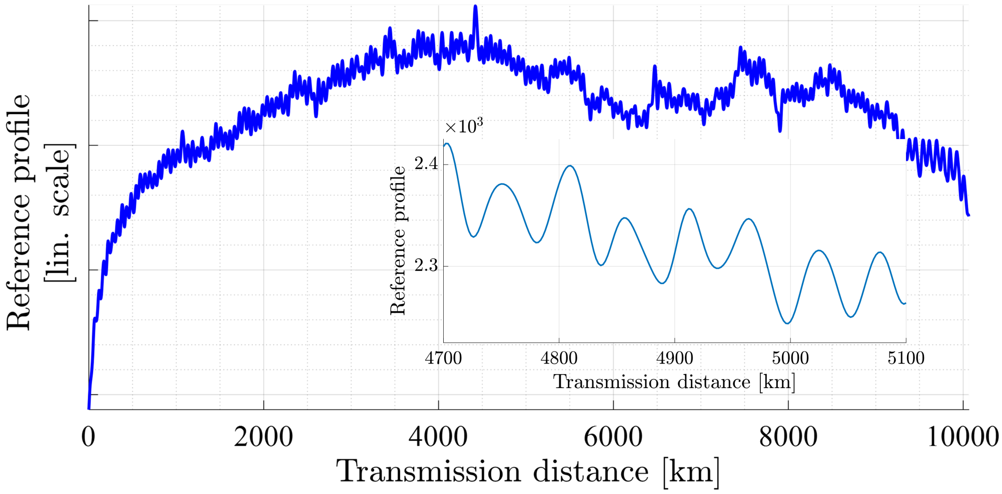

Figure 3.10: Reference power profile for configuration ii) i.e., at 32 Gbaud and for 10064 km. Inset: reference profile over the range [4700 – 5100] km.

3.3.4 Link between power profiles and topology

In this section, we study the link between the power profiles and the real topology with this long transmission distance and high number of amplifiers. To do that, we rely on the experimental results of the 69-Gbaud configuration defined in the previous section.

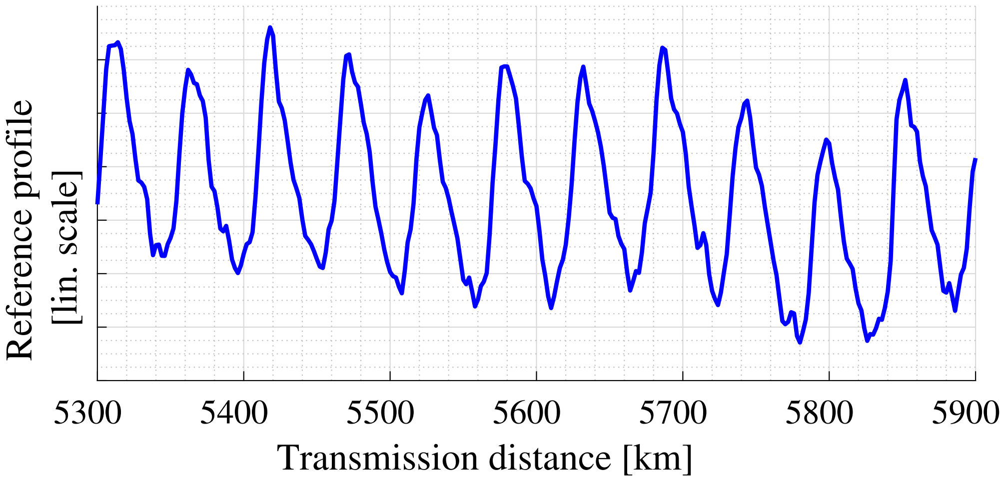

Figure 3.11: Subset of reference power profile for configuration i) over the range [5300 – 5900] km.

In Fig. 3.11 and in Fig. 3.12, we plot the power profiles obtained with the 69-Gbaud configuration for z in [5300 – 5900] and [9800 – 10250] km. Both profiles were obtained by averaging over the 112 elementary power profiles. The step here is 2 km.

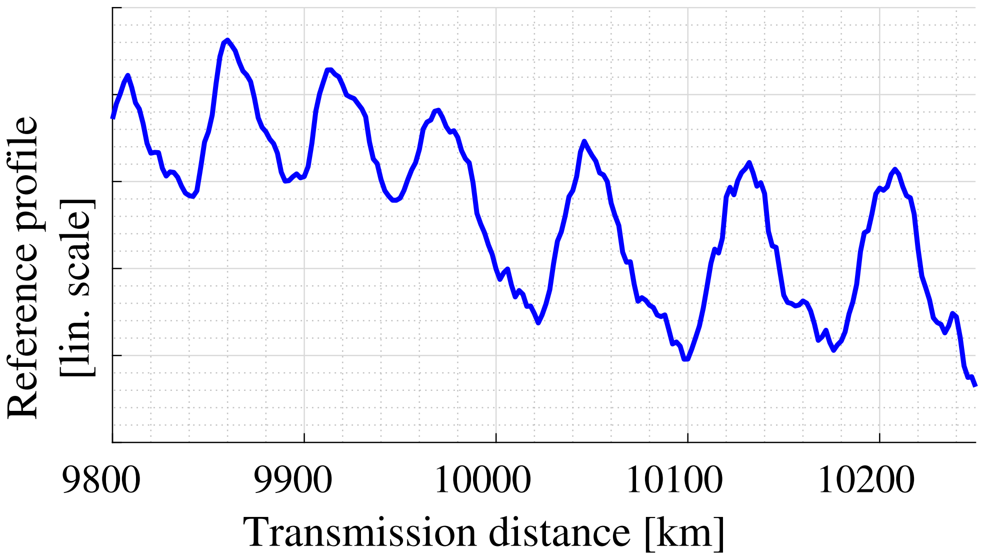

Figure 3.12: Subset of reference power profile for configuration i) over the range [9800 – 10250] km.

In Fig. 3.11, we see that the peaks are distributed periodically, which shows that the spans have the same length. To estimate the accuracy of the measured topology, we calculate, for 22 profiles, each obtained by averaging over 5 elementary profiles, the distance for 10 spans and then we divide by ten. For these 22 realizations, we get a mean value of 54.9 km with a standard deviation of 0.49 km for the average span length over these 10 spans. This value is close to the averaged span length of 55.3 km in this distance range. The step used being 2 km, the maximum accuracy is 0.2 km (step size/number of spans).

In Fig. 3.12, we see three spans with a length of around 55 km, whereas the last spans are around 75 or 80 km. This is in line with the actual topology.

To sum up, by leveraging the number of channels to compute power profiles, we can infer the topology of the 10819-km link, here demonstrated on a subset of the link, fitting well the actual topology. The study is all the more useful for submarine systems, since it allows us to make use of the several channels which share a common long path.

3.3.5 Gain anomaly detection

In this section, we study the possibility to locate simultaneously multiple power anomalies along this ultra long optical link. To do that, we rely on the experimental results of the 32-Gbaud case defined earlier. Specifically, we perform acquisitions in 3 specific dispositions, one with all amplifiers having the same output power, the reference configuration, one with one amplifier with a 3-dB lesser output power and finally one with two amplifiers with the 3-dB lesser output power.

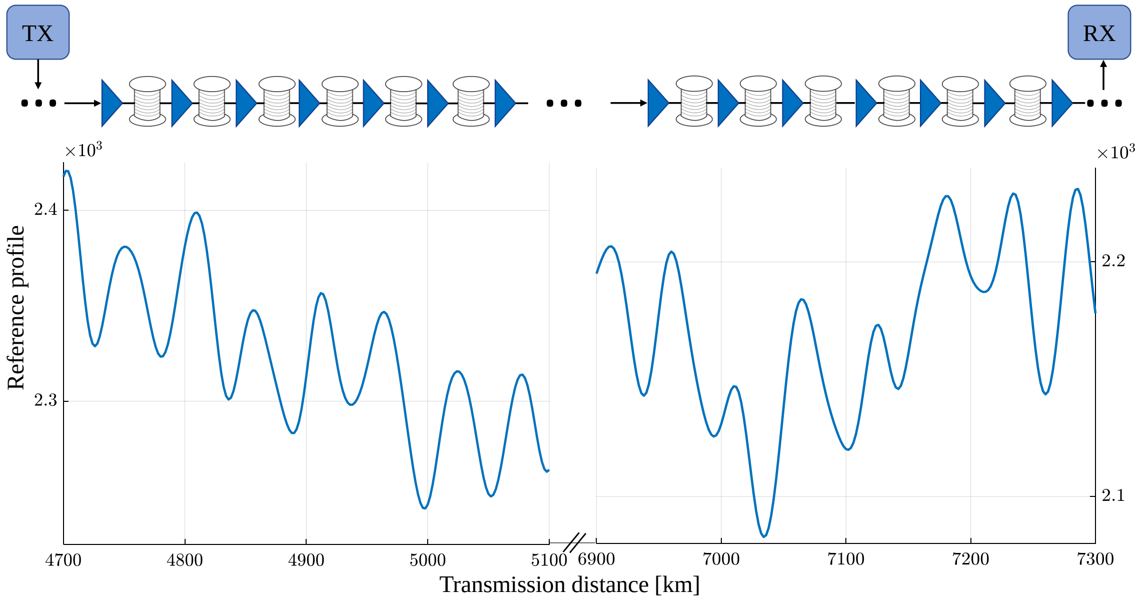

Figure 3.13: Top: Optical link from Tx to Rx with succession of amplifiers and fiber spans. All amplifiers have the same output power. Bottom : Reference power profiles for configuration ii) over [4700-5100] and [6900-7300] km.

At the top of Fig. 3.13, we draw an optical line from Tx to Rx with the succession of triangles for amplifiers and fiber spans. All amplifiers deliver the same output power which is indicated by the same blue color for all triangles. We also plot the reference power profile for two subsets of z-axis for the 32-Gbaud configuration. The chosen step is 2 km and all 1000 elementary profiles were averaged to obtain the profile, which is the case for the following graphs. We observe periodic peaks, every 55 km, as for the 69-Gbaud case, in line with the known topology.

At the top of Fig. 3.14, we draw the optical line as well. This time, a red triangle at 4800 km indicates the amplifier which has a 3-dB power anomaly. We also plot the anomaly indicator in the same two subsets as in Fig. 3.13. We successfully observe one peak which is located around the position of the faulty amplifier in the first subset. In the second subset, as expected no peak is found. Indeed, the amplifiers' output powers are the same as the reference configuration ones.

In Fig. 3.15, two red triangle at 4800 km and at 7111 km indicate the two amplifiers which have a 3-dB power anomaly. We also plot the anomaly indicator in the same two subsets as in Fig. 3.13. We successfully observe two peaks, one in each subset, located around the position of the two faulty amplifiers. Regarding

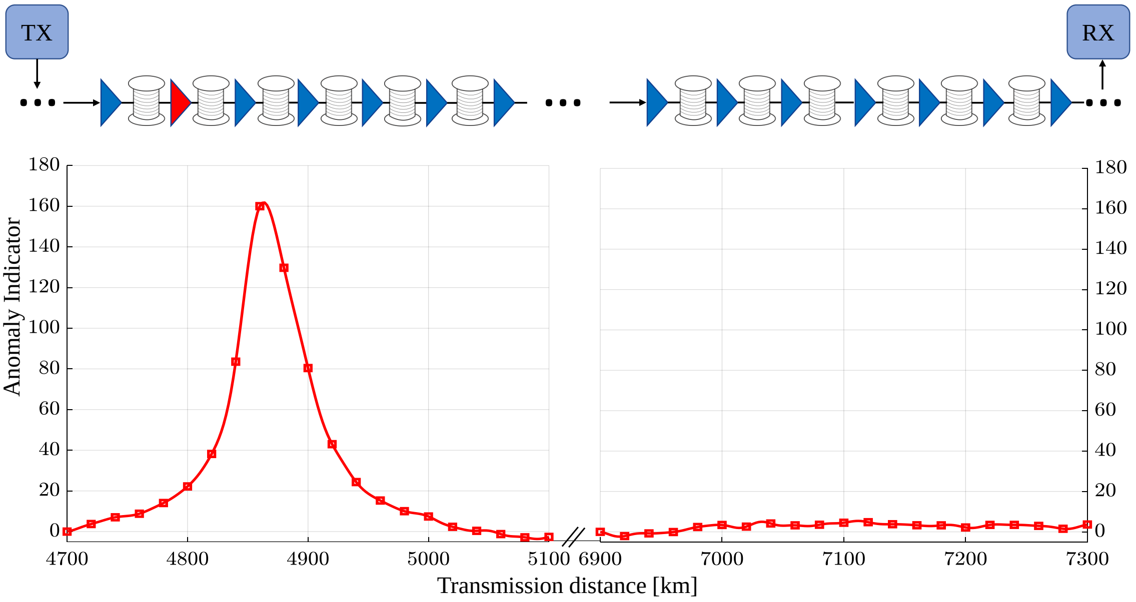

Figure 3.14: Top: Optical link from Tx to Rx with succession of amplifiers and fiber spans. One amplifier at 4804 km has a 3-dB power anomaly. Bottom : Anomaly indicators over [4700-5100] and [6900-7300] km. Markers are drawn only every 10 data points to increase readability.

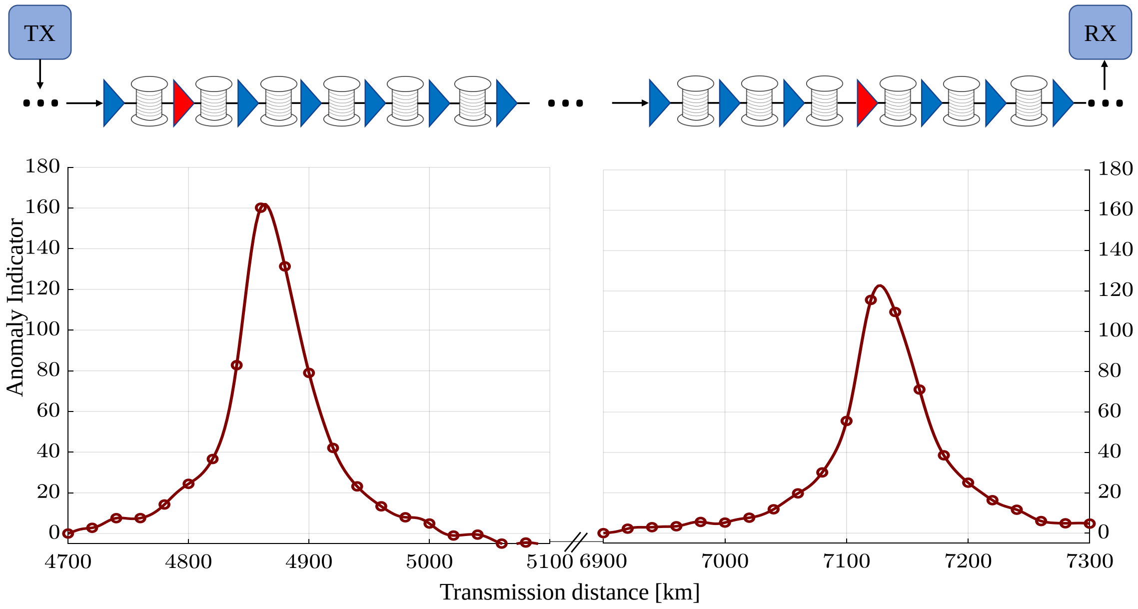

Figure 3.15: Top: Optical link from Tx to Rx with succession of amplifiers and fiber spans. Two amplifiers have a 3-dB anomaly, one at 4804 km and the other at 7111 km. Bottom : Anomaly indicators over [4700-5100] and [6900-7300] km. Markers are drawn only every 10 data points to increase readability.

the peak heights, we notice that the peaks corresponding to the first amplifier at 4804 km are almost the same height in both configurations depicted in Fig. 3.14 and in Fig. 3.15. Indeed, while it is 161.79 for the first one, it is 161.86 for the second. This is expected since the power anomaly is 3-dB in both cases and the concerned amplifier is the same. However, in Fig. 3.15, we observe that the two peaks, indicating the faulty amplifiers, do not have the same height (162 compared to 123) while the amplifier power anomalies are the same. It can be due to the inhomogeneous amplitudes that we observe in the reference power profile in Fig. 3.13.

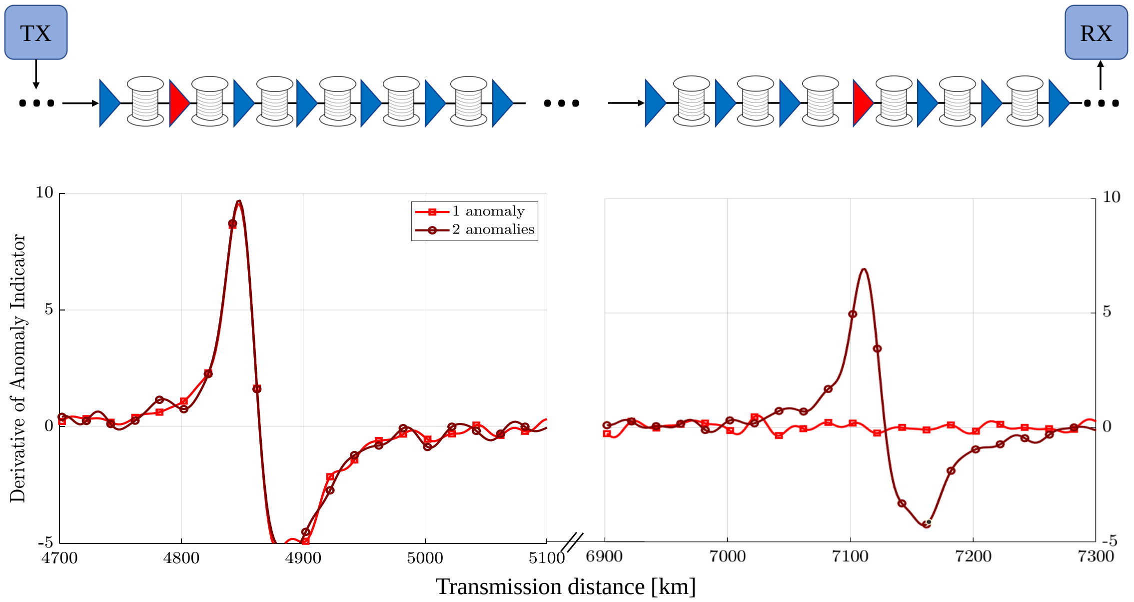

Figure 3.16: Top: Optical link from Tx to Rx with succession of amplifiers and fiber spans. Two previous cases are shown, the one with one anomaly and the other with two anomalies. Bottom : derivative of anomaly indicators over [4700-5100] and [6900-7300] km. Markers are drawn only every 10 data points to increase readability.

Finally, in Fig. 3.16, we gather the results of the two previous dispositions where either one or two amplifiers are at fault. We plot the derivative of the anomaly indicator in the same two subsets as in Fig. 3.13 for the two configurations. In the first subset, in each curve, we observe a peak. We can confirm here the high ressemblance of the two peaks. In the second subset, we observe either zero peak or one when the output power of the amplifier at 7111 km is modified.

To conclude our investigations of this straight link, we perform a preliminar study on the location of the anomalies. We focus on the absolute position of the anomalies, *i.e.*, the position with respect to the beginning of the line. The estimate $\widehat{z}_0$ of the absolute loss position is the position of the peak in the derivative of the AI, plotted in Fig. 3.16. This time, we do not average directly over the 1000 elementary power profiles. We vary the number of used power profiles for averaging from $N_{\text{AVG}} = 1$ to $N_{\text{AVG}} = 30$ (over the 1000 which are available). To have a statistics, for each number of N_{AVG}, we perform 10 realizations and therefore we have 10 estimations $\widehat{z}_0$ of loss positions for each N_{AVG} and we can estimate an average value and a standard deviation.

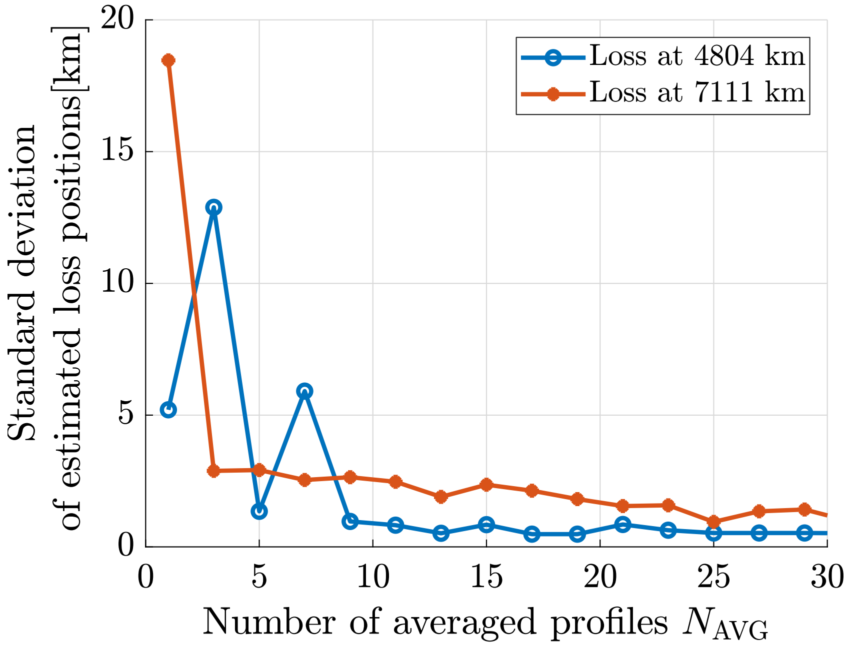

Figure 3.17: Standard deviation (over 10 realizations) on the estimated absolute loss positions $\widehat{z}_0$ for the two anomalies with respect to the number of segments.

First, let us have a look at the evolution of the standard deviation. We plot in Fig. 3.17 the standard deviation of the estimated loss positions (over 10 realizations) with respect to the number of averaged power profiles N_{AVG} for the two power anomalies. As expected, the standard deviation decreases highly with the number of averaged elementary profiles, and reaches an asymptote for $N_{\text{AVG}} = 13$, which correspond to a little bit more than 1 acquisition, which itself corresponds to $1.4 \cdot 10^6$ samples at 2 sps. The reached values are 0.5 km for the power anomaly at 4804 km and 1.9 km for the power anomaly at 7110 km. These values are quite low which is interesting for an accurate location of power anomalies. We note, the reached value does not change when we go up to $N_{\text{AVG}} = 100$, corresponding to 10 acquisitions, which confirms that this stability is kept over other acquisitions.

Then, we look at the evolution of the average estimation of the anomaly positions with the used segments. This is also the opportunity to find out about the error in the absolute location of the anomalies over 10000 km. We plot in Fig. 3.18 in

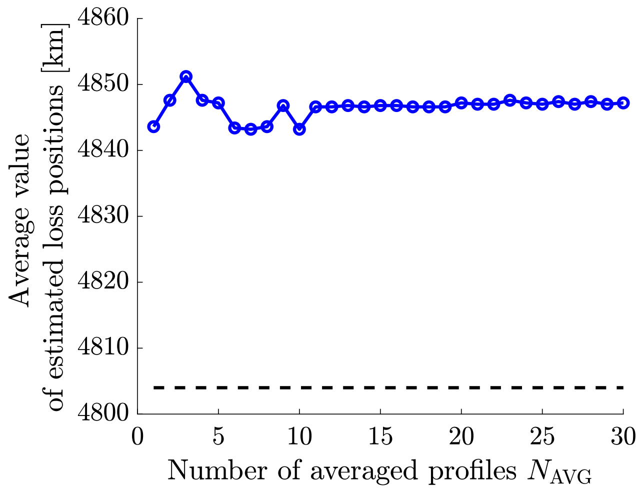

(a) Power anomaly at 4804 km.

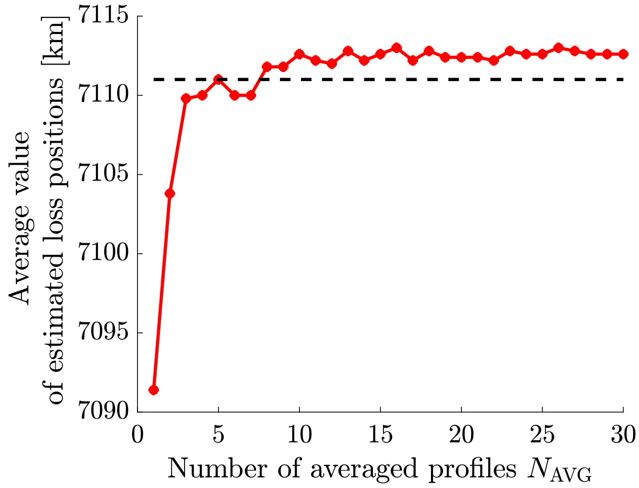

(b) Power anomaly at 7111 km.

Figure 3.18: Average estimation (over 10 realizations) of loss positions $\widehat{z}_0$ with respect to the number of averaged profiles N_{AVG}.

separate graphs the average estimation of the loss positions (over 10 realizations) with respect to the number of N_{AVG} for the two power anomalies. We plot as well in a black dotted line, the loss positions given by the topology file of the line. In both graphs, we see that after $N_{\text{AVG}} = 10$, the average estimation does not vary much and reaches an asymptote. For the anomaly at 7110 km, we see that the reached average estimation is very close to the real position, 7112 instead of 7111 km. However, for the anomaly at 4804 km, a bias of 40 km is observed. Overall, even with the bias of 40 km, for a total transmission distance of more than 10000 km, the location is quite satisfactory and allows for a high reduction of the field of research of the anomaly. However, we can wonder what can lead to an error of 40 km. One of the reasons can be the choice of using only an average value of the dispersion coefficient for the whole transmission in the algorithm. Indeed, there can be small variations of the chromatic dispersion coefficients and with such a long transsion, even small amount (20.3 to 20.7 ps/nm/km) of change can lead to a distortion (compression or dilation) of the z-axis and therefore to the shift of peaks.

3.4 Conclusion

In this chapter, we experimentally investigated the longitudinal monitoring over two types of links, terrastrial and submarine link.

In Section 3.2, we investigated the power losses calibration-based characterization method in a meshed network with a total ring of 475 km with three lightpaths. We experimentally showed a sufficient accuracy when using the calibration factor of another line, which is different in terms of distance and wavelength. We also showed that calibration factors can be extrapolated from a single one with the knowledge of launch powers. This is a first step towards the application of the method on a complex network where the high number of parameters could increase the complexity of the calibration step. Then, we proposed to combine the estimations of the same loss from the analysis of multiple lightpaths. We showed that it increases the accuracy of the characterization. For example, for a loss of 2.5 dB, the single line location error can be up to 4 km, while it is reduced to 1 km when the three estimations are averaged. It also increases reliability since it avoids having to rely on a single line for monitoring.

In Section 3.3, we performed two set of experiments to study the power profile monitoring over a long transmission link to pave the way for the use of this technique for submarine systems. We showed the successful estimation of power profiles over the link of more than 10000 km for two different symbol rates: 32 Gbaud and 69 Gbaud. We showed, for the 69-Gbaud case, the possibility to link a subset of the power profile with a subset of the line topology. We finally showed the successful detection and location of two power anomalies, paving the way for the detection of faulty amplifiers in super long links.

These two experimental works provide answers on the accuracy that we can obtained in two network scenarii, a meshed network and a long-haul optical link. It also highlights the potential gains of the network for the characterization of power losses, coming from already monitored information and the presence of multiple lightpaths. The second work provides a confirmation of the use of a DSP-based power profile estimation technique to monitor amplifiers in a long-haul links where more than 100 amplifiers can be present.

Now that the longitudinal monitoring has been used to i) characterize power losses in a point-to-point scenario and in a meshed network, and ii) detect power losses in a long-haul link, in Chapter 4, we investigate the possibility of using it to monitor another type of anomalies, polarization-dependent loss (PDL) variations.

Chapter 4

Polarization-dependent loss estimation

4.1 Introduction

To allow for a lucid diagnosis of an optical network and better decision making, monitoring has to provide as much information as possible about the incoming event, whether it be on the location, amplitude or the type of the event. In previous chapters, we focused on the detection and characterization of power anomalies in a point-to-point link, a meshed network and in a long-haul transmission. In those chapters, we considered power anomalies which impact both transmitted polarizations in the same way. However, some components have a polarization-dependent behavior, such as erbium-doped fiber amplifier (EDFA) and wavelength selective switch (WSS), which may also change with wavelength, time or their operating point. Therefore, for those components, both transmitted polarizations do not experience the same power loss when there is a power anomaly. This phenomena is called polarization dependent loss, or polarization-dependent loss (PDL). For instance, a WSS exhibits a PDL which does not only depend on the wavelength but also on the applied attenuation values per frequency slot [30]. As another example, optical amplifiers such as EDFA also show a polarization dependent behavior as their gain value slightly depends on the input polarization state of the optical signal. Since the PDL phenomena has an impact on the quality of transmission (QoT), several techniques are developped to monitor it, some of which with coherent digital signal processing (DSP) [15, 64, 65] which are interesting since they do not require additionnal hardware. However, such approaches cannot search for the location of PDL in the link but they can only monitor its accumulated amount.

Since PDL is a power loss, it has an impact on the longitudinal power of the optical link. That is why we propose to use the previously investigated power profile monitoring technique for the monitoring of the PDL. The technique as it stands previously does not allow for the distinction between a pure power loss or a PDL, which is problematic for a precise monitoring of the event and an informed decision making. Indeed, if we can distinguish polarization-independent losses from polarization-dependent ones, we can tailor a better transceiver adaptation to the detected link anomaly: changing the power margin [66] or changing the modulation and coding scheme. For instance, if moderate to high PDL values are detected, a polarization rotation of the signal tributaries at the transmitter side can help in reducing the bit-error-rate degradation induced by PDL without an increase in the average transmitted power [67].

In this chapter, we extend the power profile estimation technique proposed in [22] to detect PDL variations of an optical element with respect to precomputed levels obtained from an initial characterization of the components in the network.

This chapter is organized as follows. In Section 4.2, we recall the PDL effect of an optical element and its modelling. In Section 4.3, we study the behaviors of power profiles in presence of PDL. In Section 4.4, we present the proposed method. Finally, in Section 4.5, we assess the performance of the proposed method through numerical simulations. Concluding remarks are drawn in Section 4.6.

4.2 Polarization dependent loss

4.2.1 Effects and sources

PDL refers to the polarization dependence of the insertion loss of an optical element. We consider a PDL element represented in Fig. 4.1.

If $\boldsymbol{E}_{\mathbf{in}} = (E_{x,\text{in}}, E_{y,\text{in}})^T$ is the initial complex field at the entrance of the PDL element, then the output field is $\boldsymbol{E}_{\mathbf{out}} = \boldsymbol{H}_{\mathbf{PDL}} \cdot \boldsymbol{E}_{\mathbf{in}}$, where $\boldsymbol{H}_{\mathbf{PDL}}$ is the transfer matrix of the PDL element. To describe it mathematically, we use the Jones formalism (ref):

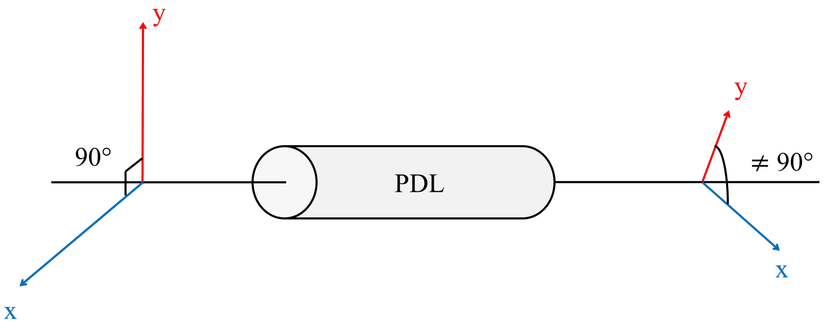

Figure 4.1: Description of the impact of a PDL element on a polarized field.

$$\boldsymbol{H}_{\mathbf{PDL}} = \mathrm{Mat}_{\mathrm{R}}(\theta,\beta)^{-1} \cdot \begin{pmatrix} 1 & 0 \\ 0 & \gamma \end{pmatrix} \cdot \mathrm{Mat}_{\mathrm{R}}(\theta,\beta). \tag{4.1}$$

where the matrix $\mathrm{Mat}_{\mathrm{R}}(\theta,\beta)$ describes the mismatch of axes between the polarization states of the incident signal and the eigenstates of the PDL element defined by the eigenangles θ and β. It can be written as follows:

$$\mathrm{Mat}_{\mathrm{R}}(\theta,\beta) = \begin{pmatrix} \cos(\beta) & i\cdot\sin(\beta) \\ -i\cdot\sin(\beta) & \cos(\beta) \end{pmatrix} \cdot \begin{pmatrix} \cos(\theta) & \sin(\theta) \\ -\sin(\theta) & \cos(\theta) \end{pmatrix}. \tag{4.2}$$

The diagonal matrix in Eq. (4.1) describes the resulting imbalance of attenuation values between the least and the most attenuated polarization states. The so-called PDL coefficient ρ_{dB} is simply the ratio between the squares of the highest and lowest coefficients of the diagonal matrix in $\boldsymbol{H}_{\mathbf{PDL}}$, expressed in dB scale. Therefore we get $\gamma = 10^{-\rho_{\mathrm{dB}}/20}$.

According to Eq. (4.1), if both components of the dual-polarized input field have the same power, they suffer from power losses and may experience a loss of orthogonality after passing through a PDL element, as illustrated in Fig. 4.1.

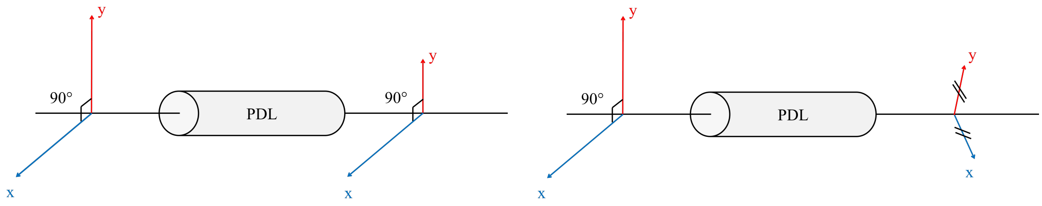

(a) $\theta = 0$ rad.

(b) $\theta = \pi/4$ rad $= 45°$.

Figure 4.2: Description of the impact of a PDL element on a polarized field for $\theta = 0$ rad and $\theta = \pi/4$ rad. In both cases $\beta = 0$.

To highlight two specific cases, we draw in Fig. 4.2 the cases where θ is equal to 0 rad and to $\pi/4$ rad with the second angle β equal to 0 rad. If we look at Eq. (4.2), when θ and β are both equal to 0, the PDL matrix is equal to a diagonal matrix. In that case, γ only acts on the "y" polarization and "x" polarization does not lose any power. There is no loss of orthogonality here, but only a power loss. In the second case, when θ is equal to $\pi/4$ rad, both components lose the same amount of power. There is a loss of orthogonality here since $\boldsymbol{H}_{\mathbf{PDL}}$ is no longer a pure diagonal matrix since the middle matrix is surrounded by two polarization rotation matrices that are not proportional to the identity matrix or to a permutation matrix. For intermediate values of θ and β, the polarization states suffers from a mixture of these two impairments: different amount of lost power for each polarization and loss of orthogonality. For all these cases, PDL will have an impact on the performance of the transmission.

In an optical line, several components can suffer from PDL. EDFA is a major source of PDL since the gain depends on the alignement of the polarizations of the pump lasers and the signal. PDL can also be induced by the optical isolators in the EDFA and by WSS [30]. Therefore, as we draw in Fig. 4.3, the optical line is composed of a succession of PDL elements.

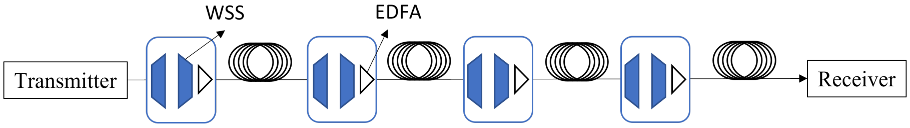

Figure 4.3: Optical line comprised of optical elements, EDFA and WSS, susceptible to carry PDL.

To minimize the effect of PDL, the individual PDL value of each component is kept as small as possible, usually much smaller than 1 dB. However, due to the large number of optical components, large accumulated PDL values can be measured at the end of the line (up to 3 dB in an installed link of 2000 km [68]).

4.2.2 Management and monitoring

In Chapter 1, we described how different effects were digitally compensated through DSP, such as chromatic dispersion (CD), polarization effects through the constant modulus algorithm (CMA), or mismatch between lasers at the reception through the carrier frequency estimation (CFE). In current systems, PDL is not mitigated through DSP. Instead, margins (up to 3 dB for polarization-division multiplexing

(PDM) systems [69]) are considered to take into account the PDL-induced penalties and to ensure a target performance.

In some works, it was proposed to reduce those penalties by decorrelating the noise on the “x” and “y” polarizations [70] or by estimating the state of polarization (SOP) of the signal and applying a certain channel inversion operation to cancel PDL [71]. Some others works proposed a Polarization-Time code at the transmitter side to mitigate the impact of the PDL [72].

In order to achieve a full optimization of the network, other works focused on the monitoring of PDL. Thanks to coherent detection, some works propose to monitor PDL by using DSP at the receiver, avoiding the use of additional hardware [15, 64, 65]. For example, it can be done by analyzing adaptive equalizer filter coefficients.

In all this manuscrit, the goal has been to monitor events and get as much information as possible about them. Most recent works focused on the total amount of accumulated PDL. However, as seen before, the optical line is comprised of multiple PDL elements. Getting the information on the location of a variable PDL or a PDL much higher than others could be beneficial to decision-making. Indeed, if the faulty optical element is detected various decisions could be made, including repairing or adapting the routing.

There have been yet little work on the location of PDL elements. In [66], thanks to an extraction of data at different nodes, the authors show the estimation of several PDL elements linked to the span in which it is located. The goal here is to accurately estimate PDL of optical elements in order to decrease the needed margins. Finally, in [60], they show experimentally the location of a PDL element by rotating the polarization at the receiver and by using a power profile estimation technique. This last work has some similarities to what we propose in this chapter. Both works, [60] and ours, were published almost simultaneously.

4.3 Power profile behavior in presence of PDL

We established that we target a distributed information about PDL along an optical line. PDL being an effect which impacts the power distribution, we propose to investigate the behavior of the power profile estimation tool in presence of PDL.

As in previous chapters, we rely on the power profile estimation technique presented in [17]. We first introduce a modified version of power profile estimation. Then, we provide numerical values of the parameters related to the propagation of a dual-polarized optical field. Finally, we study the behaviors of the modified estimation tool in presence of PDL.

4.3.1 Modified power profile estimation

The “original correlation-based” power profile estimation technique [17] presented in Section 1.4.2 and whose algorithm is presented on a schematic diagram in Fig. 1.12 is demonstrated with dual-polarized signals. However, the goal of the authors was to analyze only the total power and not the distribution of the power over the polarizations. Therefore modifications have to be done as illustrated in Fig. 4.4 where we have drawn a scheme of the modified algorithm. To monitor PDL, two simple changes are proposed:

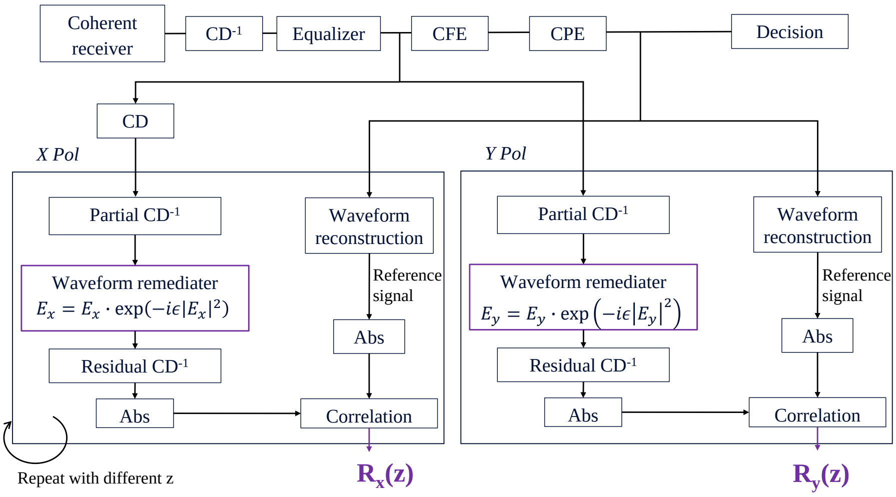

Figure 4.4: Description of the updated power profile estimation algorithm to monitor PDL. CFE: carrier frequency estimation. CPE: carrier phase estimation (CPE).

- The phase rotation that partially compensates for the self-phase modulation (SPM) is computed by only considering the power of the corresponding polarization tributary instead of the total power. In other words, we perform $E_{x,y} = E_{x,y} \cdot \exp(-i\epsilon|E_{x,y}|^2)$ instead of $E_{x,y} = E_{x,y} \cdot \exp(-i\epsilon(|E_x|^2 + |E_y|^2))$.

- Instead of analyzing the sum of power profiles over the two polarizations as proposed in [17] and as done in [21, 54] as well as in this manuscrit in previous chapters, we propose to analyze one power profile per polarization.

4.3.2 Numerical parameters

In this section, we describe the parameters of the transmitted signal, the parameters of the propagation in the fiber and finally the parameters chosen for the optical link.

Propagation parameters

The transmission consists in a single PDM-quadrature phase shift keying (QPSK) channel modulated at 32 Gbaud with an input power of 5 dBm. To simulate the propagation in the fibre, we use the split-step Fourier method (SSFM) along with Manakov equation described in Chapter 1 to take into account polarization effects. Each fiber span is modelled as the product of $N = 500$ independant waveplates with a polarization mode dispersion (PMD) parameter equal to $D_{\mathrm{PMD}} = 0.1$ ps/$\sqrt{\mathrm{km}}$. More precisely, each waveplate of length L_{wp} is represented by the following matrix:

$$\boldsymbol{H}_{\mathbf{wp}} = \mathrm{Mat}_{\mathrm{R}}(\theta_i, \beta_i)^{-1} \cdot \begin{pmatrix} \exp(i\omega\tau/2) & 0 \\ 0 & \exp(-i\omega\tau/2) \end{pmatrix} \cdot \mathrm{Mat}_{\mathrm{R}}(\theta_i, \beta_i), i = \{1, N\}, \tag{4.3}$$

where $\tau = D_{\mathrm{PMD}}/\sqrt{L_{\mathrm{wp}}}$.

Finally, we present the optical line as well as the monitoring scheme. The optical line is comprised of three 100-km spans of standard single mode fiber (SSMF), where the attenuation coefficient is equal to $\alpha_{\mathrm{dB}} = 0.2$ dB/km, the non-linear refraction index $n_2 = 2.5 \cdot 10^{-20}$ m^2/W and the effective core area $A_{\mathrm{eff}} = 80$ μm^2. EDFA are set to constant output power mode and generate amplified spontaneous emission (ASE) with a noise figure equal to 5 dB.

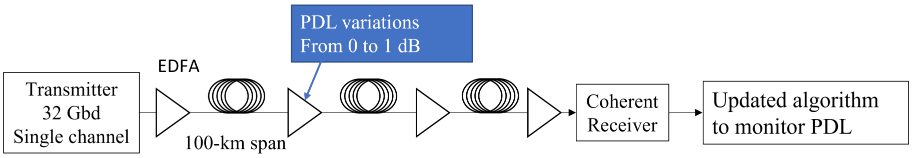

Figure 4.5: Description of the numerical set-up.

To mimick a PDL in a WSS or in an EDFA, we insert a variable PDL element, using the transfer function shown in Eq. (4.1). As seen in Fig. 4.5, we place it at the beginning of the second span, at $z = z_{\mathrm{PDL}} = 100$ km, where the node with optical components would have been. We will tune its amplitude as well as the mismatch of axes between the polarization states of the incident signal and the eigen states of the PDL, by varying γ, θ and β.

Power profile parameters

To compute power profiles, we use the updated algorithm shown in Fig. 4.4.

- As it is a simulation, we have access to the transmitted signal. As a result, the equalizer used is a least square equalizer which compares the received samples with the sent one. Moreover, the reference signal used is simply the transmitted signal.

- Each elementary profile is computed using a sequence of 1024 symbols at 2 samples per symbol (sps). The number of profiles N_{AVG} used for averaging noises is set to 500.

- The profiles parameters are the following. The non-linear rotation parameter ϵ is set to 0.01. The chosen step is 1 km.

4.3.3 Numerical analysis

In this section, we study the behavior of the power profile in presence of PDL. As in most of the manuscrit, we characterize a given state with respect to a reference configuration. We first describe the impact of PDL on the involved optical powers in the link for both configurations. Notations will be introduced. Then, we describe the different metrics involved in the PDL estimation - power profile, anomaly indicator (AI) and peak amplitudes - and we link our observations with the mathematical descriptions presented previously.

Preliminary on the effect of PDL element

We first use the PDL transfer matrix defined in Eq. (4.1) to write the impact of the PDL element on the power of each polarization in both configurations as a function of P_0, θ and γ. P_0 is the total power of the field at the entrance of the element so that $P_0 = |E_{x,\mathrm{in}}|^2 + |E_{y,\mathrm{in}}|^2$.

In Eq. (4.4), we gather power values in both configurations, reference and monitoring, before and after the PDL element. Regarding notations, as an example, $P_{x,\mathrm{out},\mathrm{mon}}$ corresponds to the power of the "x" polarization, at the output of the PDL element, *i.e.*, for $z = z_{\mathrm{PDL}}^{+}$ and in the monitoring configuration.

$$\begin{cases} P_{x,\text{in,ref}} = P_{y,\text{in,ref}} = P_{x,\text{in,mon}} = P_{y,\text{in,mon}} = P_0/2 \\ P_{x,\text{out,ref}} = P_{y,\text{out,ref}} = P_0/2 \\ P_{x,\text{out,mon}} < P_0/2 \\ P_{y,\text{out,mon}} < P_0/2. \end{cases} \tag{4.4}$$

The first line in Eq. (4.4) is simply a consequence of the definition of P_0, the total power at the entrance of the PDL element. For each configuration, this power is equally divided between each polarization since we do not consider additional PDL elements. Then, for the reference configuration, it is also trivial since we do not consider any PDL elements. The power is not modified after $z = z_{\text{PDL}}$, therefore $P_{x,\text{out,ref}} = P_{y,\text{out,ref}} = P_0/2$. Finally, of the presence of a non-zero PDL element in the monitoring configuration, the power of each polarization is smaller than $P_0/2$ and they are, *a priori*, different from each other. From Eq. (4.1), we obtain the output powers of each polarization for the monitoring configuration $P_{x,\text{out,mon}}$ and $P_{y,\text{out,mon}}$ and we gather them in Eq. 4.5.

$$\begin{cases} P_{x,\text{out,mon}} = P_0/2 \cdot (\cos^2(\theta) + \gamma^2 \sin^2(\theta)) \\ P_{y,\text{out,mon}} = P_0/2 \cdot (\sin^2(\theta) + \gamma^2 \cos^2(\theta)). \end{cases} \tag{4.5}$$

If we sum both powers, we obtain the total output power in the monitoring configuration after going through the PDL element:

$$P_{x,\text{out,mon}} + P_{y,\text{out,mon}} = P_0/2\ (1 + \gamma^2). \tag{4.6}$$

We see that if there is no PDL, which means that γ is equal to 1, *i.e.*, $\rho_{\text{dB}} = 0$, the total power is equal to P_0. However, if γ is equal to 0, the total power is divided by 2, which is the highest loss which the PDL can induce.

Power profile per polarization

As previously decribed, we consider one power profile per polarization which we compute according to the schematic shown in Fig. 4.4. Drawing from Chapter 2, we denote them by R_x and R_y. More precisely, $R_{x,\text{ref}}$ and $R_{y,\text{ref}}$ correspond to both reference power profiles whereas $R_{x,\text{mon}}$ and $R_{y,\text{mon}}$ correspond to monitoring ones.

The goal here is to monitor a possible PDL variation with respect to the reference configuration. In our simulation, for simplicity, the reference configuration is PDL-free.

An example of the monitoring power profiles for “x” and “y” polarization is given

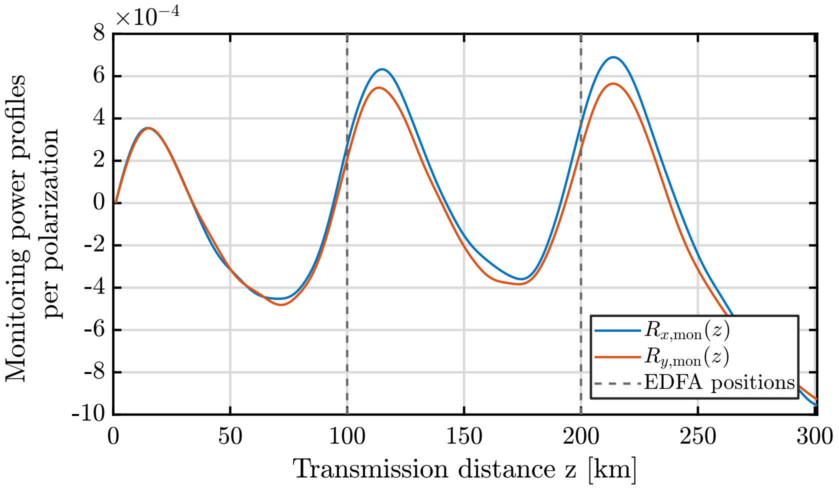

Figure 4.6: Monitoring power profiles for “x” and “y” polarization in the case of a PDL element in the monitoring configuration of value $\rho_{\text{dB}} = 0.25$ dB and $\theta = 0$ rad.

in Fig. 4.6 for a PDL of $\rho_{\text{dB}} = 0.25$ dB and $\theta = 0$ rad located at 100 km. We can observe that the two power profiles are almost identical before $z = 100$ km. Then, for higher z values, they start to shift from one another. It indicates that there is an element which has had a different impact on the power of each polarization, between the reference configuration and the monitoring configuration. More precisely, we are seeing that the power of “y” polarization is smaller than the one of “x”. This is in line with Eq. (4.1), where when θ is equal to 0 rad, only “y” polarization is experiencing a power loss. To go further in the PDL analysis, let us define other metrics.

Anomaly indicator per polarization

To carefully monitor PDL, we propose to analyze an AI per polarization defined as follows:

$$AI_i(z) = R_{i,\text{ref}}(z) - R_{i,\text{mon}}(z), i = \{x, y\}. \tag{4.7}$$

To highlight the potential of the AI per polarization, we consider the following monitoring scheme. We consider three different incident states of the signal on the PDL element of value $\rho_{dB} = 0.25$ dB: $\theta = \{0, \pi/4, \pi/2\}$ and β set to zero. In the following, we will plot for the three incident states, the AI for “x” polarization and “y” polarization and comment on the link between the observed peaks and the simulated power losses using the formalism described earlier.

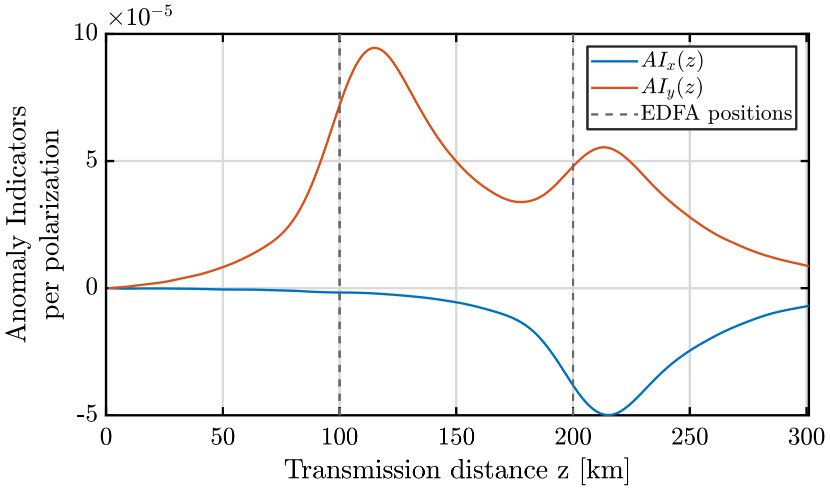

Figure 4.7: $AI_x(z)$ and $AI_y(z)$ for $\theta = 0$ rad.

i) $\theta = 0$. We plot in Fig. 4.7 the AI corresponding to both polarizations $AI_x(z)$ and $AI_y(z)$ for $\theta = 0$. We first focus on the first half of the figure, up to $z = 150$ km. We notice a peak on the $AI_y(z)$ curve and no peak on the $AI_x(z)$ curve. To understand that, we look at Eq. (4.5) in the case of $\theta = 0$. We can calculate the lost power for each polarization between the reference and the monitoring configuration. We obtain $P_{x,\text{out,ref}} - P_{x,\text{out,mon}} = P_0/2 - P_0/2 = 0$ meaning that "x" polarization did not lose any power. This is consistent with the absence of peak on the $AI_x(z)$ curve. However, for "y" polarization, $P_{y,\text{out,ref}} - P_{y,\text{out,mon}} = P_0/2 \cdot (1 - \gamma^2)$. The power for $z > z_{\text{PDL}}$ is different between the reference and monitoring configuration, which explains the existence of a peak in this position.

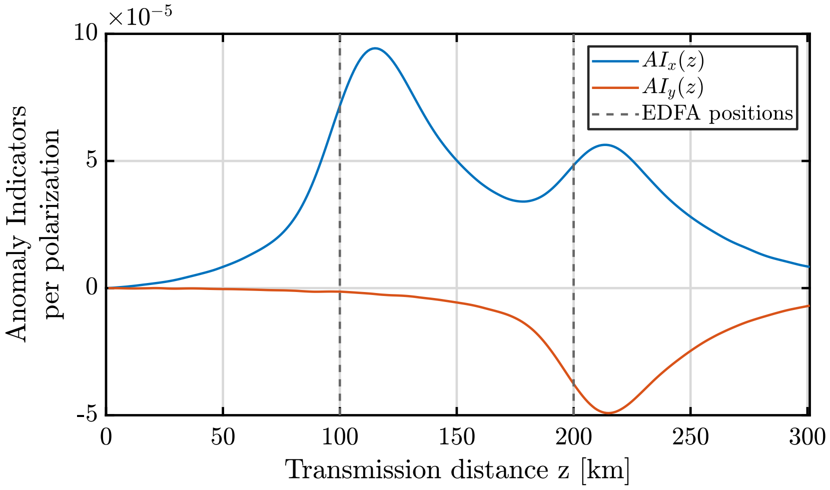

Figure 4.8: $AI_x(z)$ and $AI_y(z)$ for $\theta = \pi/2$ rad.

ii) $\theta = \pi/2$**.** We plot in Fig. 4.8 the AI corresponding to both polarizations $AI_x(z)$ and $AI_y(z)$ for $\theta = \pi/2$. Compared to the case with $\theta = 0$, we observe similar results, but the "x" and "y" polarization inversed. This is consistent with Eq. (4.5). When we have $\theta = \pi/2$ instead of $\theta = 0$, it is the "x" polarization which endures all the power loss and "y" polarization which does not lose any power between the reference and monitoring configurations.

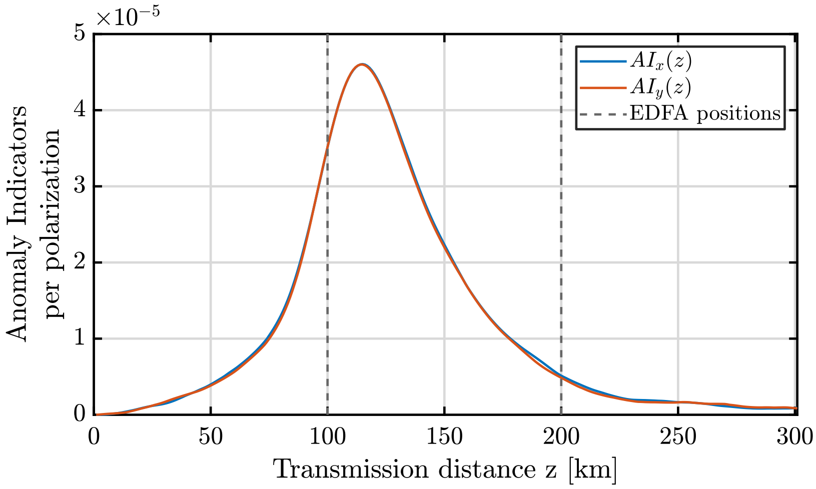

Figure 4.9: $AI_x(z)$ and $AI_y(z)$ for $\theta = \pi/4$ rad.

iii) $\theta = \pi/4$**.** We plot in Fig. 4.9 the AI corresponding to both polarizations $AI_x(z)$ and $AI_y(z)$ for $\theta = \pi/4$. We notice that the two curves are almost superimposed with a peak at $z = 100$ km. We use $\theta = \pi/4$ in Eq. (4.5) to obtain the power loss suffered from both polarizations: $P_{x,\text{out,ref}} - P_{x,\text{out,mon}} = P_{y,\text{out,ref}} - P_{y,\text{out,mon}} = P_0/2 - P_0/2 \cdot ((\sqrt{2}/2)^2 + \gamma^2(\sqrt{2}/2)^2) = P_0/4 \cdot (1 - \gamma^2)$. This confirms that both polarizations undergo the same power loss and justifies the existence of the same peak in both curves.

Finally, we take a look at the secondary peaks observed in Fig. 4.7 and 4.8. To understand their occurence, we show in Fig. 4.10 the sum of the AI per polarization : $AI(z) = AI_x(z) + AI_y(z)$. We can see a peak located at the position of the PDL element but no additional peak. This peak indicates that there is a power loss at that position. Its height - denoted A_{peak} in the previous chapters - is related to the total power loss between the reference configuration without PDL and the monitoring phase with PDL. We can write it by combining Eq. (4.4) and Eq. (4.6).

$$P_{x,\text{out,ref}} + P_{y,\text{out,ref}} - (P_{x,\text{out,mon}} + P_{y,\text{out,mon}}) = P_0/2 \cdot (1 - \gamma^2) \tag{4.8}$$

We can check that this term is equal to twice the power loss endured by each

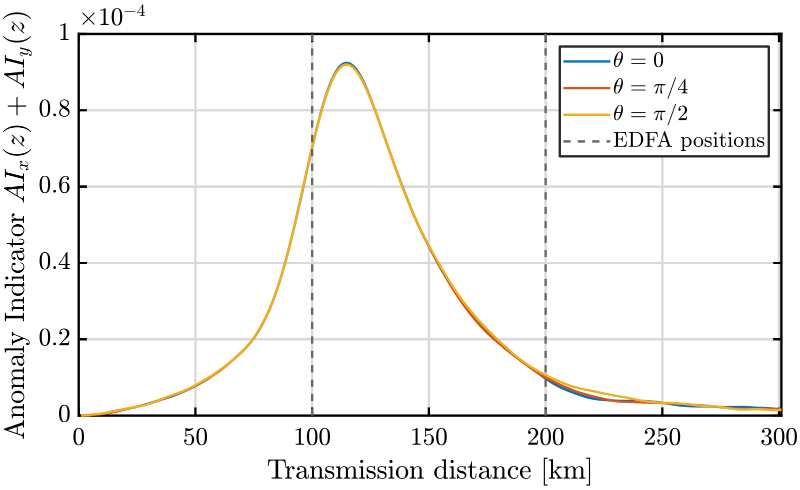

Figure 4.10: Sum of the two anomaly indicators $AI = AI_x + AI_y$.

polarization and that the peak amplitude is twice the one of each polarization for $\theta = \pi/4$.

The absence of secondary peaks around 200 km is due to the operation mode of the amplifiers set to the constant output power mode. The additional loss due to the PDL element is fully compensated by the amplifier so that the power at 200 km is the same as the one in the reference configuration, which explains the absence of a peak. However, since the amplifiers compensate for the total loss regardless of the polarization dependence of endured losses, the mismatch between the polarizations is not compensated. Therefore, the power at 200 km after compensation is different for each polarization compared to the reference case. If we look at Fig. 4.7, we see that the two peaks at 200 km are symmetrical with respect to z-axis: "x" polarization curve has a negative peak whereas "y" polarization has a positive peak. This can be explained by the following: "x" polarization has not been modified by the PDL element but its power is compensated by the following amplifier. Therefore, its power is higher in the monitoring configuration with respect to the monitoring configuration. However, "y" polarization undergoes the highest power loss possible from PDL element, and the amplifier only compensates for half of it since the other half is dedicated to the "x" polarization. Therefore, its power in the monitoring configuration is lower than in the reference configuration, thus creating a positive peak.

Peak amplitudes per polarization

Finally, to characterize the varying PDL element, we propose to measure two metrics, the peak amplitudes of the AI peaks of both polarizations. In Fig. 4.11, we

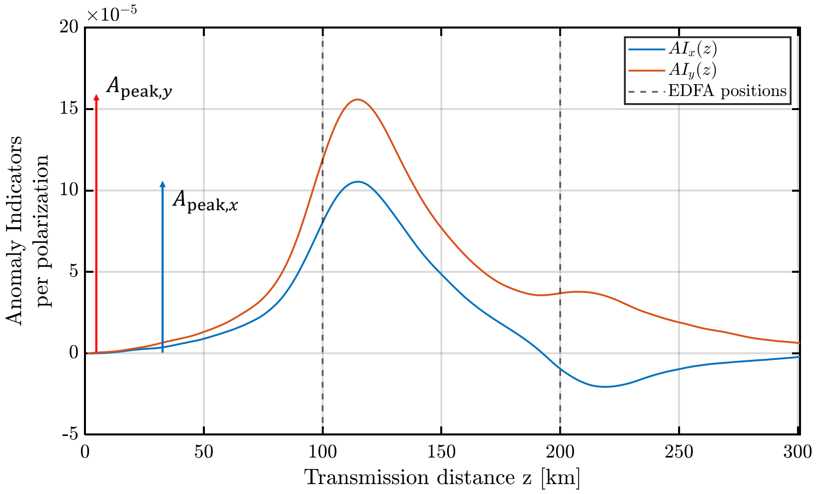

Figure 4.11: Both anomaly indicators per polarization for $\theta = 0.7$ rad.

plot both AI per polarization in the case of a PDL element of $\rho_{\text{dB}} = 0.75$ dB and $\theta = 0.69$ rad. Peak amplitudes are denoted $A_{\text{peak},x}$ and $A_{\text{peak},y}$ and are shown on the graph. We can see that we are close to the case where both peaks have the same amplitude, *i.e.*, $\theta = \pi/4$ rad, however their amplitudes seem to be different enough to indicate a variation of PDL rather than a power loss.

4.4 Proposed method

We have seen that not only the power profile estimation tool is sensitive to PDL, but its behavior can be explained by the equations describing PDL. It confirms that this tool is a good candidate to monitor PDL. In this section, we present the principle of the proposed method which is described in Fig. 4.12.

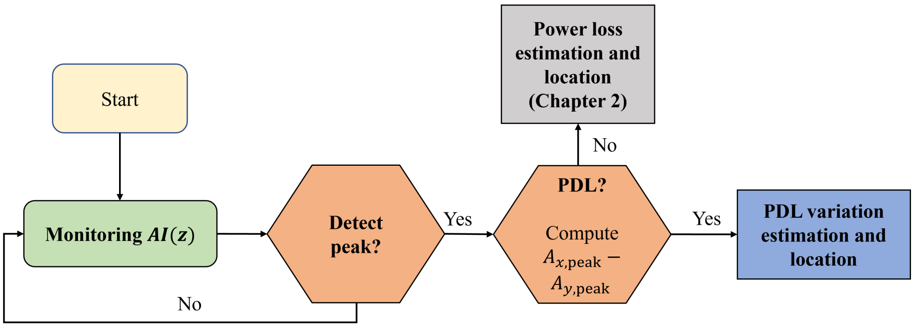

Figure 4.12: Summary diagramm of the proposed method to monitor PDL variations.

As in most of the manuscrit, the receiver-based power profile estimation technique acts an anomaly detection tool. The total anomaly indicator $AI(z)$ is being monitored and when a peak higher than a threshold is detected, an alarm is triggered. It means that there is a power anomaly at the position of the maximum slope of the peak. To fully characterize the event, we propose two steps: distinguishing a power loss from a varying PDL and estimating and locating the event, whether it be a power loss - explained in Chapter 2 - or a varying PDL. We present those two steps in the following.

4.4.1 Differentiating a PDL from a power loss

As seen in Fig. 4.10, when we focus on $AI(z) = AI_x(z) + AI_y(z)$, it is not possible to distinguish a PDL element from a power. That is why analyzing AI per polarization is necessary. We thus simply propose to evaluate $A_{\text{peak},x}$ and $A_{\text{peak},y}$ as defined earlier and compare them by computing the difference between the two. If the difference is very small, it is more likely that the event is a power loss. However, if the difference is higher, then the event is more likely to be PDL variations.

It should be noted that, as seen in Fig. 4.9 in the case of $\theta = \pi/4$ or close to $\pi/4$, it becomes more complicated to distinguish between the two. A few solutions can help in that case. We first can count on the natural rotation of polarizations to approach the PDL element with a different angle. We can also rotate the polarization at the transmitter with a polarization scramble or rotate the polarization at the receiver side as proposed in [60].

4.4.2 Locating and estimating PDL variations

Once it is established that the power anomaly is due to a varying PDL, we can locate and estimate the concerned optical element.

To locate the PDL element, a similar operation as presented in Chapter 2 is proposed. The position of the PDL element is simply given by the maximum slope of the peak in the AI. The measured position is denoted $\widehat{z}_{\text{l}}$.

To explain how to estimate PDL variations, we first recall the model we proposed in Eq. (2.10) in Chapter 2 to estimate a power loss value $l_{\text{dB}} = -10 \cdot \log_{10}(T_0)$ from the AI peak amplitude A_{peak}:

$$A_{\text{peak}}(T_0, d_{\text{l}}) = C_{\text{p}} \cdot (1 - T_0) \cdot 10^{-\frac{\alpha_{\text{dB}}}{10} \cdot d_{\text{l}}}. \tag{4.9}$$

with d_{l} the distance of the power loss from the previous amplifier and C_{p} the calibration factor with the input power included. As a reminder, we proposed to determine it by varying the output power of the amplifier - mimicking a power loss factor $(1-T)$ - and determining the slope of the function $A_{\text{peak}}(T, d_{\text{l}}=0)$. The unknown distance d_{l} is estimated using the position of the maximum slope of the detected AI peak and the position of the amplifier given by the calibration step.

We propose to use this model and method to estimate PDL variations. The peak amplitude A_{peak} considered in this case is the peak of the sum $AI_x(z)+AI_y(z)$ which is seen in Fig. 4.10. In Eq. (4.8), we wrote the power loss induced by the PDL. By identification with the power loss case where the power loss is $P_{\text{ref}} - P_{\text{mon}} = P_{\text{ref}} \cdot (1-T_0)$, the loss factor in the PDL case is $(1-\gamma^2)/2$. Therefore, we can rewrite Eq. (4.9):

$$A_{\text{peak}}(\gamma, d_{\text{l}}) = C_{\text{p}} \cdot (1-\gamma^2)/2 \cdot 10^{-\frac{\alpha_{\text{dB}}}{10} \cdot d}. \tag{4.10}$$

From Eq. (4.10), we see that the same calibration procedure as in Chapter 1 can be used to estimate γ and thus ρ_{dB}. As in Chapter 1, the steps are the following:

- Calibration step: Estimate $\widehat{C}_{\text{p}}$ by varying the output power of an amplifier. Estimate the position of the amplifier $z^{(k)}$ at the beginning of span k. The estimation is denoted - as before - $z_{\text{cal}}^{(k)}$.
- During monitoring: When an anomaly is detected and characterized as a varying PDL element, measure the peak amplitude. It is denoted as $\widehat{A}_{\text{p}}$. Measure the position of the PDL element and compute $\widehat{d} = \widehat{z}_l - z_{\text{cal}}^{(k)}$. Finally, use Eq. (4.11) to estimate γ^2 and then ρ_{dB}.

$$\gamma^2 = 1 - 2 \cdot \widehat{A}_{\text{p}} / \widehat{C}_{\text{p}} \cdot 10^{\frac{\alpha_{\text{dB}}}{10} \cdot \widehat{d}} \tag{4.11}$$

We can note that, since PDL is due to components in nodes or amplifiers and not distributed in the fiber itself, it can be fair to set the distance $\widehat{d}$ to zero if its determined value is small.

4.5 Performance of the proposed method

Finally, in this section, we study the performance of the proposed method. We keep the numerical set-up described in Fig. 4.5. As a reminder, the PDL element is inserted at the beginning of the second span and is equal to zero in the reference

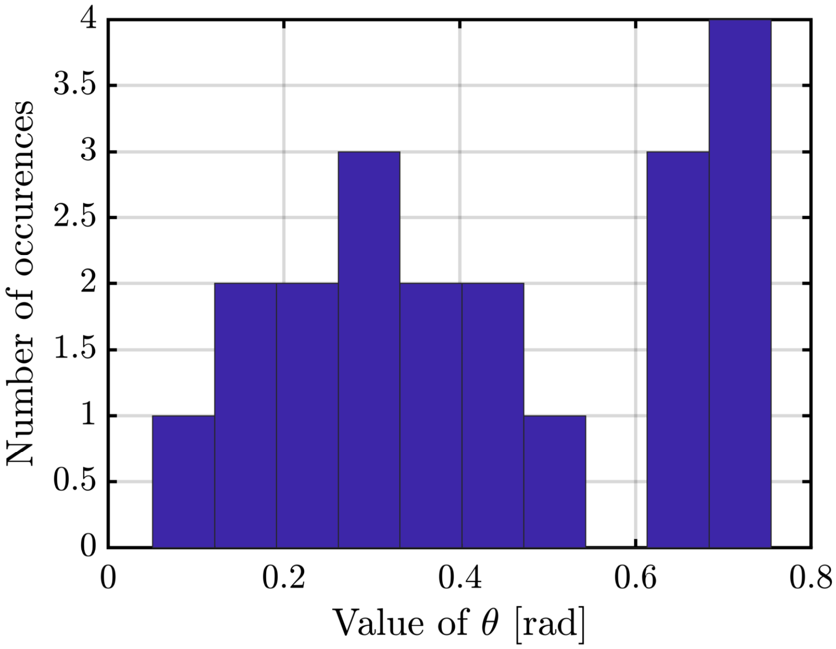

Figure 4.13: Histogram of θ values between 0 rad and $\pi/4$ rad.

configuration, whereas we set its value to $\rho_{\mathrm{dB}} = \{0.25, 0.5, 0.75, 1\}$ dB in the monitoring configuration. To describe statistically the performance, we randomly choose 20 values of θ to describe the variation of the mismatch between incoming field and PDL element eigen values. We choose to vary θ from 0 rad to $\pi/4$ rad. Indeed, for $\theta > \pi/4$, the results are symmetrical between "x" and "y" polarizations. We plot in Fig. 4.13, the histogram of the obtained θ values.

4.5.1 Distinguishing a power loss from a PDL element

To assess the possibility to distinguish power losses with varying PDL, we compare two cases: one with power losses and the other with varying PDL elements and we compute the difference between $A_{\mathrm{peak},x}$ and $A_{\mathrm{peak},y}$. To compare equivalent power losses, the power losses are set so that the loss factors $(1-T)$ are equal to $(1-\gamma^2)/2$. In Fig. 4.14, we show the difference between the peaks in the anomaly indicators for both loss types and for four loss levels. In each case, 20 estimations are performed, with the 20 θ angles. We see that the PDL can be clearly distinguished as the values of the peak differences are almost 100 times higher in the case of a PDL element. event. In practice, by setting an arbitrary threshold to $2 \cdot 10^{-6}$, we can see that we would distinguish the two types of losses perfectly.

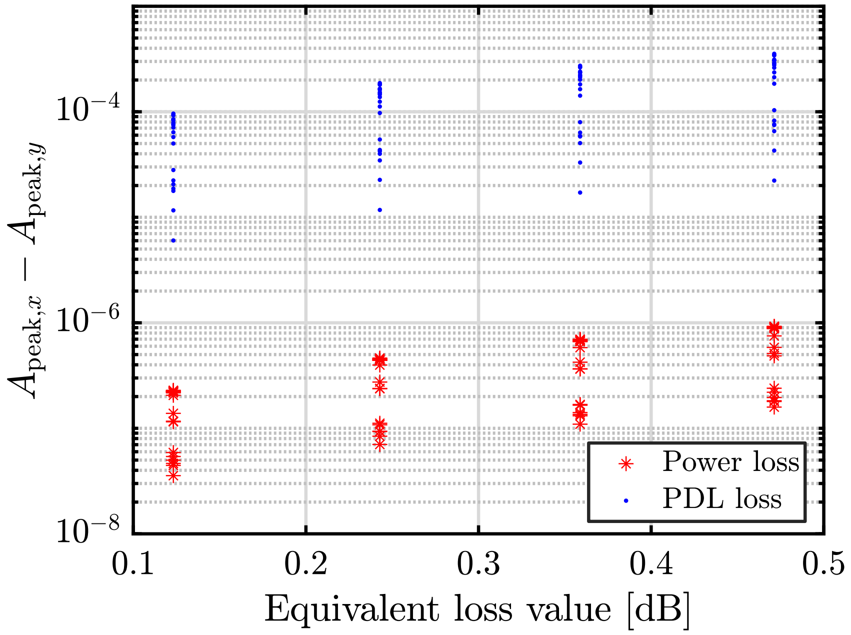

Figure 4.14: Difference $A_{\text{peak},x}$ and $A_{\text{peak},y}$ for four loss values and for two types of power losses: non-polarization dependent and polarization dependent loss. For each case, 20 differences are computed.

4.5.2 Estimating PDL variations

Finally, we assess the accuracy in estimating ρ_{dB} for the link configuration described in Fig. 4.5. We plot in Fig. 4.15, for each value of inserted PDL in the monitoring configuration, 20 markers corresponding to the estimation for 20 randoms θ angles. The estimator offers high accuracy, even for PDL variations as low as 0.25 dB. The highest standard deviation obtained is 0.0066 dB and it is for ρ_{dB}. This value is very small. This is firstly due to the fact that almost all PDL elements were perfectly located, *i.e.,* $\widehat{d} = 0 = \widehat{z}_l - z_{\text{cal}}^{(k)}$. Only three out of $20 \cdot 4 = 80$ estimations were not perfect. We note that it is due to the chosen step of 1 km. If the chosen step had been smaller, though the obtained distances should still be smaller than 1 or 2 km, we would have obtained more non-zero values for $\widehat{d}$, *e.g.,* 500 m. We obtained one $\widehat{d} = 1$ km and two $\widehat{d} = -1$ km. As in Chapter 2, obtaining a negative value for d is not realistic. In our case, this means having a varying PDL at 99 km. As for power losses, the exponential decrease of the peak amplitude makes it impossible to have such a peak far away from previous amplifier. Therefore, we can choose to bring those two values to 0 km. This type of location accuracy obtained here is however realistic since it is quite similar to the one obtained in the experiments presented in Chapter 1. Locating PDL elements here benefits from the high sensibility of the method where the power is the highest.

Secondly, such a small standard deviation is also due to the low noise level of the power profiles computed from simulations. We can remind that, in Chapter 1, we obtained 0.2 dB of standard deviation for losses located at the position of the amplifier.

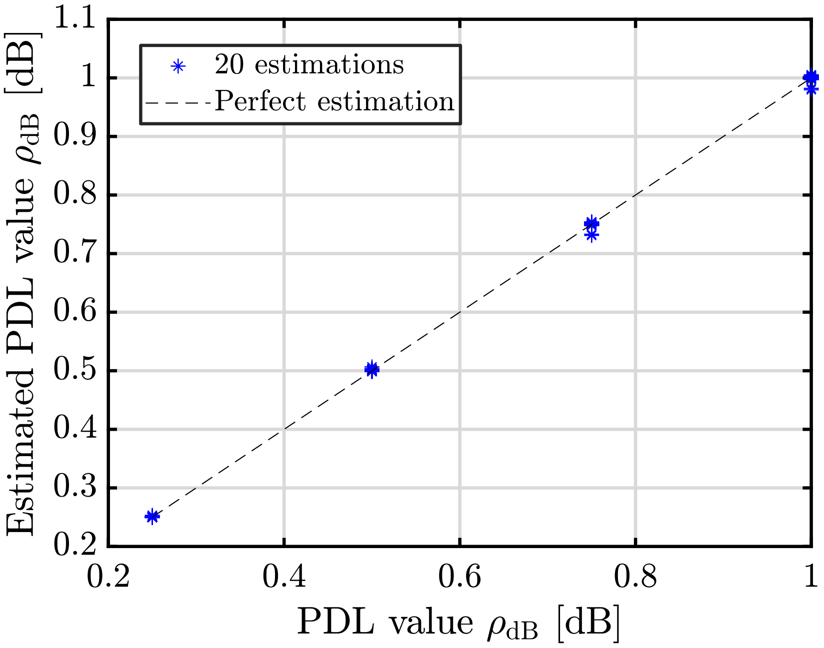

Figure 4.15: Estimated PDL values ρ_{dB} with respect to inserted PDL values.

4.6 Conclusion

In this chapter, we investigated the monitoring of another type of physical effect: polarization dependent loss. The goal is common to the previous chapters: get as much information possible about an optical line in order to take smart decisions.

We proposed the use of a power profile estimation technique with a slightly updated algorithm to monitor longitudinally the PDL. The aim is to get closer to the location of the PDL and not only rely on the total amount of PDL over a whole optical line.

More precisely, the proposed method is the following: the AI is monitored. When a peak is higher than a certain threshold, an alarm is triggered which confirms the occuring of a power anomaly, as in Chapter 2. Then, we focus on the AIs per polarization $AI_x(z)$ and $AI_y(z)$ and we compare both peak amplitudes $A_{\mathrm{peak},x}$ and $A_{\mathrm{peak},y}$. If the difference between the two is higher than a certain threshold, we decide that it is a varying PDL. Otherwise, it is a simple power loss. We can locate both thanks to the position of the maximum slope of the AI peak. In the case of a PDL, we propose an analogous model as in Chapter 2 to estimate PDL variations.

Finally, we assessed the performance of the proposed method. We confirmed that by choosing a certain threshold (10^{-5}), we were able to distinguish all varying PDL elements from pure power losses. We also successfully locate varying PDL elements with a chosen step of 1 km at the exact simulated position. This is coherent with experiments done in Chapter 2 where 90 % of power losses located at the beginning of the span were perfectly located. Here we benefit from the usual location of PDL elements which is where the power is the highest and therefore where the method is most sensitive. Finally, we showed the estimation of the variation of PDL elements, from 0.25 to 0.7 dB with respect to a reference configuration where it was set to zero. The estimation was very accurate, with a standard deviation of 0.0066 dB. To be more realistic, we can expect an accuracy of the same order of what we obtained for power losses, which is around 0.2 dB.

In an optical line where several PDL elements can occur, the proposed method, here validated in a simple case, can gain complexity. Nevertheless several potential solutions can be proposed. In the same regard as what is shown in Chapter 3, we can benefit from the already many parameters already monitored in an optical network. For instance, a high PDL can be detected at the end of a line through the monitoring of the signal-to-noise ratio (SNR) per polarization. This information can be coupled with the power profile estimation tool to refine the characterization. Moreover, coupling our proposed method with the work done in [60] could allow the distinguishment between power losses and PDL even for cases aroung $\theta = \pi/4$. Additionnally, it could also allow for the estimation of existing PDL rather than only variations, using another way to calibrate.

Conclusion

DSP-based monitoring techniques are promising solutions for the further optimization of optical fiber networks. Two pioneer longitudinal power profile estimation techniques were proposed in the literature at the beginning of my PhD, offering low-cost monitoring solutions for a parameter much relevant for the optimization: the optical power in the fiber link. Both techniques showed the possibility to detect power losses in multi-span link through an AI but do not study the estimation of loss values. Moreover, the two experimental demonstrations were performed in a point-to-point link of similar total distance, around 250 km.

In this manuscript, we investigated the use of power profile estimation techniques for the accurate estimation and location of power losses - independent or dependent from polarization - in various network scenarii such as a meshed network and a long-haul optical link. We focused on the correlation-based techniques particularly for their flexibility: when implementing the algorithm, either the "original" or "forward" one, we can target specific zones (values on the z-axis) to monitor without having to simulate the total propagation (from 0 to the total length of the transmission distance), thus saving computation time.

We first proposed a calibration-based method to estimate both the position and the value of power losses relying on the power profile estimation technique. To this end, we proposed a simple model describing the behavior of the power profile, leading to an mathematical expression of the AI and of the peak amplitude induced by a power loss. We finally applied our method on a 300-km link and assessed the accuracy of the loss value estimation. We obtain a standard deviation and a bias smaller than 0.2 dB for loss located at 100 km, at the position of an amplifier, and of values ranging from 1.6 to 10.0 dB, which is quite satisfactory. We obtained the same accuracy for losses located at 125 km of up to 5 dB. For higher loss values, the bias and the standard deviation are increasing.

We then experimentally investigated the calibration-based power losses characterization method in a meshed optical network with a total ring of 475 km. We proposed to use the same calibration factor for three lightpaths characterized by a given wavelength and a given transmission distance (from 202 to 421 km) and we experimentally validated it. We also showed how one calibration factor could be enough for multiple span input powers if the knowledge on the power is available. Finally, we proposed to combine loss estimations from those three lightpaths that share a common span in which the power anomaly has occured. We showed how the accuracy is improved both for the loss position and loss value. For example, for an inserted power loss of 2.5 dB, the single line location error can be up to 4 km, while it is reduced to 1 km when the three estimations are averaged. In this example, we also see that performing the estimation with multiple lightpaths not only increases the accuracy but also the reliability since it avoids having to rely on a single line for monitoring.

Finally, we focused on the detection of another type of power anomalies: PDL. To this end, we proposed the use of a power profile estimation technique with a slightly updated algorithm to longitudinally monitor the PDL. The aim is to get a finer estimation of the position of PDL and not only rely on the estimation of the global PDL over the whole optical link. We proposed the following method: a power profile with the updated algorithm is periodically computed. If a power anomaly is detected, we proposed a criteria based on peak amplitudes to detect whether it is a varying PDL or a pure power loss. Finally, the varying PDL or the power loss can be estimated. We validated this method by performing numerical simulations.

Perspectives

While my work covered several aspects of correlation-based power profile estimation techniques, it paves the way for future investigations.

We have seen in Chapter 1 the different techniques which have been proposed to estimate the longitudinal power profile. Some techniques are based on a correlation [17, 57]. Another one is based on a gradient descent algorithm which performs iteratively the SSFM [18]. A novel technique is based on a Volterra equalization [20]. Finally, a promising solution is a least squares technique [58]. Those several works call for a proper comparison between them. An important aspect to be investigated concerns the accuracy which they can offer. This accuracy will have to be characterized with respect to the used number of data samples. Another important point of comparison is the complexity of the algorithm implementation. To conclude, outcomes of this comparison might not be limited to the choice of “the best" power profile estimation technique, but rather guidelines on which ones to use depending on the monitoring needs (accuracy, speed of monitoring).

The accuracy of the power profile estimation technique as well as the proposed method in Chapter 2 depends on several physical parameters. The accumulated CD [ps/nm] and the total length of the fiber L [km], or the accumulated CD and the CD parameter D [ps/nm/km] are needed for the location of anomalies since they allow for the mapping in distance. The fiber attenuation α_{dB} [dB/km] is needed to estimate the loss values if the proposed method is used. Those parameters, if available, are known with a given uncertainty. One important investigation would be to study the robustness of the power profile estimation technique and the calibration-based method with respect to the system parameters. This could motivate the improvement of the methods to be more robust, even if this translates into an increase of complexity.

Finally, a first analytical derivation has been performed [59, 63] to compare the correlation-based and the linear squares techniques. Analytical derivations are necessary to deepen our understanding on the subject. It can also give guidelines to improve the technique. Finally, it brings knowledge on the potential limits of the technique, *e.g.,* which physical effects are to be exploited (SPM, cross-phase modulation (XPM)). Investigations in this topic could include going further in the derivation and find closed-form expressions for other techniques.

Bibliography

[1] D. Brake, "Submarine cables: Critical infrastructure for global communications," *Information technology*, p. 11, 2019.

[2] G. P. Agrawal, *Nonlinear Fiber Optics*, Third Edition (Optics and Photonics). Academic Press, 2001.

[3] S. J. Savory, "Digital coherent optical receivers: Algorithms and subsystems," *IEEE Journal of Selected Topics in Quantum Electronics*, vol. 16, no. 5, pp. 1164–1179, Sep. 2010, ISSN: 1077-260X, 1558-4542. DOI: `10.1109/JSTQE.2010.2044751`.

[4] "Cisco annual internet report - cisco annual internet report (2018–2023) white paper - cisco." (), [Online]. Available: `https://www.cisco.com/c/en/us/solutions/collateral/executive-perspectives/annual-internet-report/white-paper-c11-741490.html`.

[5] "Measuring digital development: Facts and figures." (2022), [Online]. Available: `https://www.itu.int/hub/publication/d-ind-ict_mdd-2022/`.

[6] F. Bordage. "The environmental footprint of the digital world." (2019), [Online]. Available: `https://www.greenit.fr/wp-content/uploads/2019/11/GREENIT_EENM_etude_EN_accessible.pdf`.

[7] O. Gerstel, M. Jinno, A. Lord, and S. B. Yoo, "Elastic optical networking: A new dawn for the optical layer?" *IEEE Communications Magazine*, vol. 50, no. 2, s12–s20, Feb. 2012, ISSN: 0163-6804, 1558-1896. DOI: `10.1109/MCOM.2012.6146481`.

[8] K. Christodoulopoulos *et al.*, "ORCHESTRA - optical performance monitoring enabling flexible networking," in *2015 17th International Conference on Transparent Optical Networks (ICTON)*, Budapest: IEEE, Jul. 2015, pp. 1–4, ISBN: 978-1-4673-7880-2. DOI: `10.1109/ICTON.2015.7193584`.

[9] C. Delezoide, P. Ramantanis, and P. Layec, "Leveraging field data for the joint optimization of capacity and availability in low-margin optical networks," *Journal of Lightwave Technology*, vol. 38, no. 24, pp. 6709–6718, 2020. DOI: `10.1109/JLT.2020.3022107`.

[10] Y. Pointurier, "Design of low-margin optical networks," *Journal of Optical Communications and Networking*, vol. 9, no. 1, A9, Jan. 1, 2017, ISSN: 1943-0620, 1943-0639. DOI: `10.1364/JOCN.9.0000A9`.

[11] P. Ramantanis, C. Delezoide, P. Layec, and S. Bigo, "Revisiting the calculation of performance margins in monitoring-enabled optical networks," *Journal of Optical Communications and Networking*, vol. 11, no. 10, p. C67, Oct. 1, 2019, ISSN: 1943-0620, 1943-0639. DOI: `10.1364/JOCN.11.000C67`.

[12] F. Boitier *et al.*, "Proactive fiber damage detection in real-time coherent receiver," in *2017 European Conference on Optical Communication (ECOC)*, Gothenburg, Sep. 2017, pp. 1–3, ISBN: 978-1-5386-5624-2. DOI: `10.1109/ECOC.2017.8346077`.

[13] A. Dupas, P. Layec, D. Verchere, Q. P. Van, and S. Bigo, "Ultra-fast hitless 100gbit/s real-time bandwidth variable transmitter with SDN optical control,"

in *Optical Fiber Communication Conference*, San Diego, California: OSA, 2018, Th2A.46, ISBN: 978-1-943580-38-5. DOI: `10.1364/OFC.2018.Th2A.46`.

[14] D. C. Kilper *et al.*, “Optical performance monitoring,” *Journal of Lightwave Technology*, vol. 22, no. 1, p. 294, Jan. 2004.

[15] F. Hauske, M. Kuschnerov, B. Spinnler, and B. Lankl, “Optical performance monitoring in digital coherent receivers,” *Journal of Lightwave Technology*, vol. 27, no. 16, pp. 3623–3631, Aug. 2009, ISSN: 0733-8724, 1558-2213. DOI: `10.1109/JLT.2009.2024960`.

[16] D. C. Kilper, W. Weingartner, S. Hunsche, and A. Azarov, “Q-factor monitoring using FEC for fault-management applications,” *J. Opt. Netw.*, vol. 3, no. 8, pp. 651–663, Aug. 2004, Publisher: Optica Publishing Group. DOI: `10.1364/JON.3.000651`.

[17] T. Tanimura, K. Tajima, S. Yoshida, S. Oda, and T. Hoshida, “Experimental demonstration of a coherent receiver that visualizes longitudinal signal power profile over multiple spans out of its incoming signal,” in *45th European Conference on Optical Communication (ECOC 2019)*, Dublin, Ireland, 2019, 297 (4 pp.)–297 (4 pp.) ISBN: 978-1-83953-185-9. DOI: `10.1049/cp.2019.1031`.

[18] T. Sasai *et al.*, “Simultaneous detection of anomaly points and fiber types in multi-span transmission links only by receiver-side digital signal processing,” in *Optical Fiber Communication Conference (OFC) 2020*, San Diego, California, 2020, Th1F.1, ISBN: 978-1-943580-71-2. DOI: `10.1364/OFC.2020.Th1F.1`.

[19] T. Sasai, M. Nakamura, E. Yamazaki, and Y. Kisaka, “Precise longitudinal power monitoring over 2,080 km enabled by step size selection of split step fourier method,” in *Optical Fiber Communication Conference (OFC) 2022*,

San Diego, California, 2022, Th1C.4, ISBN: 978-1-55752-466-9. DOI: `10.1364/OFC.2022.Th1C.4`.

[20] S. Gleb, P. Konstantin, J. Luo, and B. Zheng, “Fiber link anomaly detection and estimation based on signal nonlinearity,” in *2021 European Conference on Optical Communication (ECOC)*, Bordeaux, France, Sep. 13, 2021, pp. 1–4, ISBN: 978-1-66543-868-1. DOI: `10.1109/ECOC52684.2021.9606094`.

[21] M. Sena, R. Emmerich, B. Shariati, J. K. Fischer, and R. Freund, “Link tomography for amplifier gain profile estimation and failure detection in c+l-band open line systems,” in *Optical Fiber Communication Conference (OFC) 2022*, San Diego, California, 2022, Th1H.1, ISBN: 978-1-55752-466-9. DOI: `10.1364/OFC.2022.Th1H.1`.

[22] T. Tanimura, S. Yoshida, K. Tajima, S. Oda, and T. Hoshida, “Fiber-longitudinal anomaly position identification over multi-span transmission link out of receiver-end signals,” *Journal of Lightwave Technology*, vol. 38, no. 9, pp. 2726–2733, May 1, 2020, ISSN: 0733-8724, 1558-2213. DOI: `10.1109/JLT.2020.2984270`.

[23] J. Renaudier *et al.*, “Recent advances in 100+nm ultra-wideband fiber-optic transmission systems using semiconductor optical amplifiers,” *Journal of Lightwave Technology*, vol. 38, no. 5, pp. 1071–1079, 2020. DOI: `10.1109/JLT.2020.2966491`.

[24] B. J. Puttnam, G. Rademacher, and R. S. Luís, “Space-division multiplexing for optical fiber communications,” *Optica*, vol. 8, no. 9, pp. 1186–1203, Sep. 2021, Publisher: Optica Publishing Group. DOI: `10.1364/OPTICA.427631`.

[25] “Corning LEAF optical fiber, product information.” (Jun. 2014), [Online]. Available: `https://www.corning.com/media/worldwide/coc/documents/Fiber/LEAF%20optical%20fiber.pdf`.

[26] P. Poggiolini, G. Bosco, A. Carena, V. Curri, Y. Jiang, and F. Forghieri, "The GN-model of fiber non-linear propagation and its applications," *Journal of Lightwave Technology*, vol. 32, no. 4, pp. 694–721, 2014. DOI: `10.1109/JLT.2013.2295208`.

[27] A. Carena, G. Bosco, V. Curri, Y. Jiang, P. Poggiolini, and F. Forghieri, "EGN model of non-linear fiber propagation," *Opt. Express*, vol. 22, no. 13, pp. 16 335–16 362, Jun. 2014, Publisher: Optica Publishing Group. DOI: `10.1364/OE.22.016335`.

[28] E. Ip and J. M. Kahn, "Compensation of dispersion and nonlinear impairments using digital backpropagation," *Journal of Lightwave Technology*, vol. 26, no. 20, pp. 3416–3425, 2008. DOI: `10.1109/JLT.2008.927791`.

[29] Z. Tao *et al.*, "Complexity-reduced digital nonlinear compensation for coherent optical system," in *Next-Generation Optical Communication: Components, Sub-Systems, and Systems II*, G. Li, Ed., Backup Publisher: International Society for Optics and Photonics, vol. 8647, SPIE, 2013, 86470K. DOI: `10.1117/12.2002284`.

[30] D. Xie *et al.*, "LCoS-based wavelength-selective switch for future finer-grid elastic optical networks capable of all-optical wavelength conversion," *IEEE Photonics Journal*, vol. 9, no. 2, pp. 1–12, Apr. 2017, ISSN: 1943-0655. DOI: `10.1109/JPHOT.2017.2671436`.

[31] G. P. Agrawal, *Nonlinear Fiber Optics*, Fifth Edition (Optics and Photonics). Academic Press, 2012.

[32] K. Kikuchi, "Fundamentals of coherent optical fiber communications," *Journal of Lightwave Technology*, vol. 34, no. 1, pp. 157–179, Jan. 1, 2016, ISSN: 0733-8724, 1558-2213. DOI: `10.1109/JLT.2015.2463719`.

[33] M. Kuschnerov *et al.*, “DSP for coherent single-carrier receivers,” *Journal of Lightwave Technology*, vol. 27, no. 16, pp. 3614–3622, Aug. 2009, ISSN: 0733-8724, 1558-2213. DOI: `10.1109/JLT.2009.2024963`.

[34] F. Pittalà, I. Slim, A. Mezghani, and J. A. Nossek, “Training-aided frequency-domain channel estimation and equalization for single-carrier coherent optical transmission systems,” *Journal of Lightwave Technology*, vol. 32, no. 24, pp. 4849–4863, 2014. DOI: `10.1109/JLT.2014.2358933`.

[35] A. Leven, N. Kaneda, U.-V. Koc, and Y.-K. Chen, “Frequency estimation in intradyne reception,” *IEEE Photonics Technology Letters*, vol. 19, no. 6, pp. 366–368, 2007. DOI: `10.1109/LPT.2007.891893`.

[36] T. Pfau, S. Hoffmann, and R. Noe, “Hardware-efficient coherent digital receiver concept with feedforward carrier recovery for m-QAM constellations,” *Journal of Lightwave Technology*, vol. 27, no. 8, pp. 989–999, Apr. 2009, ISSN: 0733-8724. DOI: `10.1109/JLT.2008.2010511`.

[37] A. J. Viterbi and A. M. Viterbi, “Nonlinear estimation of PSK-modulated carrier phase with application to burst digital transmission,” *IEEE Transactions on Information Theory*, vol. 29, no. 4, pp. 543–551, Jul. 1983, ISSN: 0018-9448, 1557-9654. DOI: `10.1109/TIT.1983.1056713`.

[38] A. Gouin, “Real-time flexible and virtualized transponders for optical communications,” Ph.D. dissertation, INSA, Rennes, 2022.

[39] E. Seve, J. Pesic, C. Delezoide, S. Bigo, and Y. Pointurier, “Learning process for reducing uncertainties on network parameters and design margins,” *Journal of Optical Communications and Networking*, vol. 10, no. 2, A298, Feb. 1, 2018, ISSN: 1943-0620, 1943-0639. DOI: `10.1364/JOCN.10.00A298`.

[40] Z. Jiang and S. Wang, “Diagnosing transient behavior during channel add/drop by real-time performance monitoring,” in *OSA Advanced Photonics Congress 2021*, Journal Abbreviation: OSA Advanced Photonics Congress 2021, Optica Publishing Group, 2021, NeF2B.5. DOI: `10.1364/NETWORKS.2021.NeF2B.5`.

[41] F. Boitier *et al.*, “Seamless optical path restoration with just-in-time resource allocation leveraging machine learning,” in *2018 European Conference on Optical Communication ECOC*, Rome, Sep. 2018, pp. 1–3. DOI: `10.1109/ECOC.2018.8535279`.

[42] *Optical monitoring for dense wavelength division multiplexing systems.* 2016.

[43] P. Serena *et al.*, “Locating fiber loss anomalies with a receiver-side monitoring algorithm exploiting cross-phase modulation,” in *Optical Fiber Communication Conference (OFC) 2023*, San Diego, California: Optica Publishing Group, 2023, W1H.3.

[44] A. Carena, V. Curri, R. Guadino, P. Poggiolini, and S. Benedetto, “New analytical results on fiber parametric gain and its effects on ASE noise,” *IEEE Photonics Technology Letters*, vol. 9, no. 4, pp. 535–537, Apr. 1997, ISSN: 1041-1135, 1941-0174. DOI: `10.1109/68.559413`.

[45] C. Lorattanasane and K. Kikuchi, “Parametric instability of optical amplifier noise in long-distance optical transmission systems,” *IEEE Journal of Quantum Electronics*, vol. 33, no. 7, pp. 1068–1074, Jul. 1997, ISSN: 00189197. DOI: `10.1109/3.594867`.

[46] G. Bellotti, M. Varani, C. Francia, and A. Bononi, “Intensity distortion induced by cross-phase modulation and chromatic dispersion in optical-fiber transmissions with dispersion compensation,” *IEEE Photonics Technology Let-*

ters, vol. 10, no. 12, pp. 1745–1747, Dec. 1998, ISSN: 1041-1135, 1941-0174. DOI: `10.1109/68.730489`.

[47] K. Peddanarappagari and M. Brandt-Pearce, "Volterra series transfer function of single-mode fibers," *Journal of Lightwave Technology*, vol. 15, no. 12, pp. 2232–2241, Dec. 1997, ISSN: 07338724. DOI: `10.1109/50.643545`.

[48] K. Peddanarappagari and M. Brandt-Pearce, "Volterra series approach for optimizing fiber-optic communications system designs," *Journal of Lightwave Technology*, vol. 16, no. 11, pp. 2046–2055, Nov. 1998, ISSN: 07338724. DOI: `10.1109/50.730369`.

[49] A. Vannucci, P. Serena, and A. Bononi, "The RP method: A new tool for the iterative solution of the nonlinear schrodinger equation," *Journal of Lightwave Technology*, vol. 20, no. 7, pp. 1102–1112, Jul. 2002, ISSN: 0733-8724. DOI: `10.1109/JLT.2002.800376`.

[50] P. Serena and A. Bononi, "An alternative approach to the gaussian noise model and its system implications," *Journal of Lightwave Technology*, vol. 31, no. 22, pp. 3489–3499, Nov. 2013, ISSN: 0733-8724, 1558-2213. DOI: `10.1109/JLT.2013.2284499`.

[51] T. Hoshida *et al.*, "Advanced DSP for monitoring and mitigation in optical transport networks," in *Optical Fiber Communication Conference (OFC) 2020*, San Diego, California: OSA, 2020, Th1I.1, ISBN: 978-1-943580-71-2. DOI: `10.1364/OFC.2020.Th1I.1`.

[52] T. Tanimura, S. Yoshida, S. Oda, K. Tajima, and T. Hoshida, "Advanced data-analytics-based fiber-longitudinal monitoring for optical transport networks," in *2020 European Conference on Optical Communications (ECOC)*,

Brussels, Belgium, Dec. 2020, pp. 1–4, ISBN: 978-1-72817-361-0. DOI: `10.1109/ECOC48923.2020.9333137`.

[53] M. Sena *et al.*, "DSP-based link tomography for amplifier gain estimation and anomaly detection in c+l-band systems," *Journal of Lightwave Technology*, vol. 40, no. 11, pp. 3395–3405, Jun. 1, 2022, ISSN: 0733-8724, 1558-2213. DOI: `10.1109/JLT.2022.3160101`.

[54] M. Sena *et al.*, "Advanced DSP-based monitoring for spatially resolved and wavelength-dependent amplifier gain estimation and fault location in c+l-band systems," *Journal of Lightwave Technology*, pp. 1–10, 2022, ISSN: 0733-8724, 1558-2213. DOI: `10.1109/JLT.2022.3208209`.

[55] T. Sasai, M. Nakamura, E. Yamazaki, S. Yamamoto, H. Nishizawa, and Y. Kisaka, "Digital backpropagation for optical path monitoring: Loss profile and passband narrowing estimation," in *2020 European Conference on Optical Communications (ECOC)*, Brussels, Belgium, Dec. 2020, pp. 1–4, ISBN: 978-1-72817-361-0. DOI: `10.1109/ECOC48923.2020.9333191`.

[56] T. Sasai, M. Nakamura, T. Kobayashi, H. Kawakami, E. Yamazaki, and Y. Kisaka, "Revealing raman-amplified power profile and raman gain spectra with digital backpropagation," in *Optical Fiber Communication Conference (OFC) 2021*, Washington, DC, 2021, p. M3I.5, ISBN: 978-1-943580-86-6. DOI: `10.1364/OFC.2021.M3I.5`.

[57] C. Hahn, J. Chang, and Z. Jiang, "Localization of reflection induced multi-path-interference over multi-span transmission link by receiver-side digital signal processing," in *Optical Fiber Communication Conference (OFC) 2022*, San Diego, California, 2022, Th1C.3, ISBN: 978-1-55752-466-9. DOI: `10.1364/OFC.2022.Th1C.3`.

[58] T. Sasai, E. Yamazaki, M. Nakamura, and Y. Kisaka, "Proposal of linear least squares for fiber-nonlinearity-based longitudinal power monitoring in multi-span link," in *2022 27th OptoElectronics and Communications Conference (OECC) and 2022 International Conference on Photonics in Switching and Computing (PSC)*, Toyama, Japan: IEEE, Jul. 3, 2022, pp. 1–4, ISBN: 978-4-88552-336-6. DOI: `10.23919/OECC/PSC53152.2022.9850175`.

[59] T. Sasai, E. Yamazaki, M. Nakamura, and Y. Kisaka, "Closed-form expressions for fiber-nonlinearity-based longitudinal power profile estimation methods," 2022.

[60] M. Eto, K. Tajima, S. Yoshida, S. Oda, and T. Hoshida, "Location-resolved PDL monitoring with rx-side digital signal processing in multi-span optical transmission system," in *Optical Fiber Communication Conference (OFC) 2022*, San Diego, California, 2022, Th1C.2, ISBN: 978-1-55752-466-9. DOI: `10.1364/OFC.2022.Th1C.2`.

[61] L. Gifre *et al.*, "Demonstration of monitoring and data analytics-triggered reconfiguration in partially disaggregated optical networks," in *Optical Fiber Communication Conf.*, San Diego, California: OSA, 2020, M3Z.19, ISBN: 978-1-943580-71-2. DOI: `10.1364/OFC.2020.M3Z.19`.

[62] B. Jander *et al.*, "Enhanced undersea line monitoring technology for coherent open cable systems," presented at the Suboptic, 2019, p. 5.

[63] T. Sasai, E. Yamazaki, and Y. Kisaka, "Performance limit of fiber-longitudinal power profile estimation methods," *Journal of Lightwave Technology*, pp. 1–13, 2023, ISSN: 0733-8724, 1558-2213. DOI: `10.1109/JLT.2023.3234534`.

[64] C. Xie and S. Chandrasekhar, "Two-stage constant modulus algorithm equalizer for singularity free operation and optical performance monitoring in opti-

cal coherent receiver," in *Optical Fiber Communication Conference*, San Diego, California: OSA, 2010, OMK3, ISBN: 978-1-55752-885-8. DOI: `10.1364/OFC.2010.OMK3`.

[65] G. Huang *et al.*, "Polarization dependent loss monitor with visualization on poincaré sphere in digital coherent system," in *2017 European Conference on Optical Communication (ECOC)*, Gothenburg, Sep. 2017, pp. 1–3, ISBN: 978-1-5386-5624-2. DOI: `10.1109/ECOC.2017.8345947`.

[66] J. Girard-Jollet *et al.*, "Estimating network components PDL using performance statistical measurements," *Journal of Lightwave Technology*, pp. 1–9, 2022, ISSN: 0733-8724, 1558-2213. DOI: `10.1109/JLT.2022.3181786`.

[67] A. Dumenil, E. Awwad, and C. Measson, "PDL in optical links: A model analysis and a demonstration of a PDL-resilient modulation," *Journal of Lightwave Technology*, vol. 38, no. 18, pp. 5017–5025, Sep. 15, 2020, ISSN: 0733-8724, 1558-2213. DOI: `10.1109/JLT.2020.2998841`.

[68] L. E. Nelson *et al.*, "Statistics of polarization dependent loss in an installed long-haul WDM system," *Optics Express*, vol. 19, no. 7, p. 6790, Mar. 28, 2011, ISSN: 1094-4087. DOI: `10.1364/OE.19.006790`.

[69] M. Shtaif, "Performance degradation in coherent polarization multiplexed systems as a result of polarization dependent loss," *Optics Express*, vol. 16, no. 18, p. 13 918, Sep. 1, 2008, ISSN: 1094-4087. DOI: `10.1364/OE.16.013918`.

[70] M. Zamani, Z. Zhang, C. Chen, and C. Li, "PDL compensation using whitening matrix in polarization division multiplexed coherent optical transmission," in *Optical Fiber Communication Conference/National Fiber Optic Engineers Conference 2013*, Anaheim, California: OSA, 2013, JW2A.49, ISBN: 978-1-55752-962-6. DOI: `10.1364/NFOEC.2013.JW2A.49`.

[71] N. J. Muga and A. N. Pinto, “Digital PDL compensation in 3d stokes space,” *Journal of Lightwave Technology*, vol. 31, no. 13, pp. 2122–2130, Jul. 2013, ISSN: 0733-8724, 1558-2213. DOI: `10.1109/JLT.2013.2263849`.

[72] E. Awwad, Y. Jaouën, and G. R.-B. Othman, “Polarization-time coding for PDL mitigation in long-haul PolMux OFDM systems,” *Optics Express*, vol. 21, no. 19, p. 22 773, Sep. 23, 2013, ISSN: 1094-4087. DOI: `10.1364/OE.21.022773`.

ECOLE DOCTORALE

Titre : Nouvelles technologies de réception cohérente pour la mesure et le contrôle des paramètres physiques de transmission sur fibres optiques

Mots clés : Monitoring, effets non-linéaires, détection cohérente, réseaux optiques fibrés

Résumé : Dans les réseaux à fibre optique, le monitoring massif a suscité un intérêt important pour leur permettre d'être plus autonomes et élastiques. Au fil des années, diverses techniques de monitoring basées sur le traitement numérique du signal côté récepteur ont été proposées. Ces techniques sont particulièrement intéressantes car elles ne nécessitent pas de matériel supplémentaire et sont moins coûteuses. Dans ma thèse, je me suis concentrée sur les techniques de monitoring de la puissance longitudinale d'un lien optique, basées sur l'analyse des effets de propagation non linéaires. Dans un premier temps, j'ai proposé d'utiliser une technique existante pour estimer la valeur d'une perte de puissance dans une liaison optique point à point et je l'ai validée expérimentalement. Ensuite, j'ai généralisé la méthode d'estimation des pertes de puissance et l'ai appliquée à un réseau maillé. L'utilisation de différents trajets lumineux sur ce réseau m'a permis de montrer une augmentation de la précision de l'estimation des valeurs de perte. Afin d'élargir les possibilités de mise en œuvre de cette méthode, j'ai étudié ensuite expérimentalement l'application de la technique d'estimation du profil de puissance sur une longue liaison optique pour valider son utilisation pour les systèmes sous-marins. Enfin, je propose d'utiliser cette technique pour surveiller un autre type de pertes de puissance, la perte dépendante de la polarisation (PDL). La PDL est présente dans les composants optiques tels que les commutateurs et les amplificateurs. Habituellement, seul le montant cumulé est surveillé. J'ai proposé d'utiliser une méthode similaire à celle des pertes de puissance, permettant de localiser un élément PDL variable et d'estimer sa variation. Ce dernier travail nous permet de connaître plus précisément le type d'événement, ce qui est important pour prendre des décisions plus intelligentes et efficaces.

Title : Novel receiver-based techniques for the monitoring of physical parameters in optical fiber networks

Keywords : Monitoring, non-linear effects, coherent detection, optical fibered networks

Abstract : In optical fibered networks, massive monitoring generated significant interest to allow them to be more autonomous and elastic. Over the years, various monitoring techniques based on the digital signal processing at the receiver side have been proposed. Those techniques are particularly interesting since they do not require additional hardware and are less costly. In my PhD, I focused on techniques to monitor the longitudinal power of an optical link, based on the analysis of non-linear propagation effects. First, I proposed to use an existing technique to estimate the value of a power loss in a point-to-point optical link and validated it experimentally. Then, I generalized the power losses estimation method and applied it to a meshed network. Using various lightpaths on this network allowed me to show experimentally an increase of the accuracy of the estimation of loss values. To broaden the possibilities of implementation of this method, I then investigate experimentally the application of the power profile estimation technique on a long optical link to validate its use for submarine systems. Finally, I propose to use this technique to monitor another type of power losses, polarization-dependent loss (PDL). PDL is present in optical components such as switches and amplifiers. Usually, only the accumulated amount is monitored. I proposed to use a similar method as with the power losses, allowing the location of a varying PDL element and the estimation of its variation. This latest work allows us to get closer to the type of event, which is important to take smart and effective solutions.

Institut Polytechnique de Paris
91120 Palaiseau, France